Florida Department of Transportation
Final Report
July 2017

Impedance-Based Detection of Corrosion in Post-Tensioned Cables: Phase 2 from Concept to Application

FDOT Contract No. BDV31-977-35

FDOT Project Manager:	Ron Simmons
UF Principal Investigator:	Mark Orazem, PhD
Consultant:	David Bloomquist, PhD, PE
Graduate Students:	Christopher Alexander, PhD Yu-Min Chen, PhD

Disclaimer

Cover photograph: Ringling Causeway Bridge, Florida. Taken by Mark Orazem

Approximate Conversions to SI Units

SYMBOL	WHEN YOU KNOW	MULTIPLY BY	TO FIND	SYMBOL
LENGTH				
in	inches	25.4	millimeters	mm
ft	feet	0.305	meters	m
yd	yards	0.914	meters	m
mi	miles	1.61	kilometers	km

SYMBOL	WHEN YOU KNOW	MULTIPLY BY	TO FIND	SYMBOL
AREA				
in^2	squareinches	645.2	square millimeters	mm^2
ft^2	squarefeet	0.093	square meters	m^2
yd^2	square yard	0.836	square meters	m^2
ac	acres	0.405	hectares	ha
mi^2	square miles	2.59	square kilometers	km^2

SYMBOL	WHEN YOU KNOW	MULTIPLY BY	TO FIND	SYMBOL
VOLUME				
fl oz	fluid ounces	29.57	milliliters	mL
gal	gallons	3.785	liters	L
ft^3	cubic feet	0.028	cubic meters	m^3
yd^3	cubic yards	0.765	cubic meters	m^3
NOTE: volumes greater than 1000 L shall be shown in m^3				

SYMBOL	WHEN YOU KNOW	MULTIPLY BY	TO FIND	SYMBOL
MASS				
oz	ounces	28.35	grams	g
lb	pounds	0.454	kilograms	kg
T	short tons (2000 lb)	0.907	megagrams (or "metric ton")	Mg (or "t")

SYMBOL	WHEN YOU KNOW	MULTIPLY BY	TO FIND	SYMBOL
TEMPERATURE (exact degrees)				
ºF	Fahrenheit	5 (F-32)/9 or (F-32)/1.8	Celsius	ºC

SYMBOL	WHEN YOU KNOW	MULTIPLY BY	TO FIND	SYMBOL
ILLUMINATION				
fc	foot-candles	10.76	lux	lx
fl	foot-Lamberts	3.426	candela/m^2	cd/m^2

SYMBOL	WHEN YOU KNOW	MULTIPLY BY	TO FIND	SYMBOL
FORCE and PRESSURE or STRESS				
lbf	poundforce	4.45	newtons	N
lbf/in^2	poundforce per square inch	6.89	kilopascals	kPa

SYMBOL	WHEN YOU KNOW	MULTIPLY BY	TO FIND	SYMBOL
LENGTH				
mm	millimeters	0.039	inches	in
m	meters	3.28	feet	ft
m	meters	1.09	yards	yd
km	kilometers	0.621	miles	mi

SYMBOL	WHEN YOU KNOW	MULTIPLY BY	TO FIND	SYMBOL
AREA				
mm^2	square millimeters	0.0016	square inches	in^2
m^2	square meters	10.764	square feet	ft^2
m^2	square meters	1.195	square yards	yd^2
ha	hectares	2.47	acres	ac
km^2	square kilometers	0.386	square miles	mi^2

SYMBOL	WHEN YOU KNOW	MULTIPLY BY	TO FIND	SYMBOL
VOLUME				
mL	milliliters	0.034	fluid ounces	fl oz
L	liters	0.264	gallons	gal
m^3	cubic meters	35.314	cubic feet	ft^3
m^3	cubic meters	1.307	cubic yards	yd^3

SYMBOL	WHEN YOU KNOW	MULTIPLY BY	TO FIND	SYMBOL
MASS				
g	grams	0.035	ounces	oz
kg	kilograms	2.202	pounds	lb
Mg (or "t")	megagrams (or "metric ton")	1.103	short tons (2000 lb)	T

SYMBOL	WHEN YOU KNOW	MULTIPLY BY	TO FIND	SYMBOL
TEMPERATURE (exact degrees)				
°C	Celsius	1.8C+32	Fahrenheit	°F

SYMBOL	WHEN YOU KNOW	MULTIPLY BY	TO FIND	SYMBOL
ILLUMINATION				
lx	lux	0.0929	foot-candles	fc
cd/m^2	candela/m^2	0.2919	foot-Lamberts	fl

SYMBOL	WHEN YOU KNOW	MULTIPLY BY	TO FIND	SYMBOL
FORCE and PRESSURE or STRESS				
N	newtons	0.225	poundforce	lbf
kPa	kilopascals	0.145	poundforce per square inch	lbf/in^2

*SI is the symbol for the International System of Units. Appropriate rounding should be made to comply with Section 4 of ASTM E380.
(Revised March 2003)

Technical Report Documentation Page

1. Report No.	2. Government Accession No.	3. Recipient's Catalog No.
4. Title and Subtitle Impedance-Based Detection of Corrosion in Post-Tensioned Cables: Phase 2 from Concept to Application		5. Report Date July, 2017
		6. Performing Organization Code
7. Author(s) Christopher L. Alexander, Yu-Min Chen, and Mark E. Orazem		8. Performing Organization Report No.
9. Performing Organization Name and Address University of Florida Department of Chemical Engineering		10. Work Unit No. (TRAIS)
		11. Contract or Grant No. BDV31-977-35
12. Sponsoring Agency Name and Address Florida Department of Transportation 605 Suwannee Street, MS 30 Tallahassee, FL 32399		13. Type of Report and Period Covered Final Report – 12/29/2014-7/31/2017
		14. Sponsoring Agency Code
15. Supplementary Notes		

16. Abstract

Indirect impedance was explored as a non-destructive means of detecting active corrosion in post-tensioned tendons used in segmentally constructed bridges. The research program included both fundamental studies to quantify corrosion rates and oxide film thicknesses for ASTM A416 steel in simulated pore solutions and in grout and practical studies to determine how indirect impedance may be employed in field applications. Indirect impedance was found to provide a means of detecting corrosion in tendons if the corroding strands are located near the grout-duct interface and are directly under one of the two current injection electrodes. The indirect impedance approach is only qualitative because the grout impedance obscures quantification of the corrosion rate. Corrosion of strands in the center of a duct containing many strands cannot be detected by indirect impedance. These conclusions are supported by experimental observations and numerical simulations.

Thus, indirect impedance may be useful if corrosion can be anticipated to occur in response to grout segregation, for which corroding strands will be located near the top of tendons. The procedure for the indirect impedance measurement is relatively simple, and the instrumentation required can weigh less than 20 pounds. Measurements are performed in approximately 20 minutes, and the holes that are drilled can be sealed if desired.

17. Key Word Indirect impedance, Post-tensioned tendons, Corrosion		18. Distribution Statement No Restrictions	
19. Security Classif. (of this report) Unclassified	20. Security Classif. (of this page) Unclassified	21. No. of Pages 104	22. Price

Form DOT F 1700.7 (8-72) Reproduction of completed page authorized

Acknowledgements

The authors gratefully acknowledge financial support from the Florida Department of Transportation (Contract BDV31-977-35, Ronald Simmons, project manager) Technical assistance from Nicholas G. Rudawski and Eric Lambers of the Major Analytical Instrumentation Center at the University of Florida is also gratefully acknowledged.

Publications Based on Present Work

A portion of the work presented in this report was published as:

- Y.-M. Chen, N. G. Rudawski, E. Lambers, and M. E. Orazem, “Application of Impedance Spectroscopy and Surface Analysis to Obtain Oxide Film Thickness,” *Journal of the Electrochemical Society,* (2017), in press.
- Y.-M. Chen and M. E. Orazem, “Impedance Analysis of ASTM A416 Tendon Steel Corrosion in Alkaline Simulated Pore Solutions,” *Corrosion Science,* **104** (2016), 26-35.
- Christopher L. Alexander, *Impedance Spectroscopy: The Influence of Surface Heterogeneity and Application to Corrosion Monitoring od Bridge Tendons,* Ph.D. dissertation, University of Florida, May 2017.
- Yu-Min Chen, *Analysis of ASTM A416 Tendon Steel Corrosion in Alkaline Simulated Pore Solutions,* Ph.D. dissertation, University of Florida, August 2016.

Executive Summary

The objective of the present work was to explore the feasibility of using indirect impedance as a means of detecting corrosion in post-tensioned tendons used in segmentally constructed bridges. Indirect impedance was first proposed to detect corrosion of concrete reinforcement, but the technique has not been employed due to difficulties associated with interpretation of the measured spectra. The idea explored here is that the confined geometry of the tendon may facilitate interpretation, making indirect impedance more useful than it has been in assessing the condition of concrete structures.

The research plan followed several intersecting paths. Fundamental studies were performed to explore the behavior of ASTM A416 steel in electrolytes chosen to mimic the properties of solutions found in the pores of cured grout. To facilitate interpretation of the results, only the circular cross-section of the steel strand was exposed to the grout. Electrochemical techniques, including cyclic voltammetry, measurement of steady-state polarization curves, and direct impedance spectroscopy, were paired with surface analysis techniques. Of these, the most useful were x-ray photoelectron spectroscopy (XPS), used to identify differences between steel samples, and high-angle annular dark-field scanning transmission electron microscopy (HAADF-STEM), used to measure the thickness of oxide layers following exposure. This work showed: (1) differences in the performance of two separate batches of steel with the same nominal composition; (2) the recently developed power-law model[1,2] provided a means to interpret the impedance response in terms of oxide film thickness, an important property of metals that rely on passivation to prevent corrosion; and (3) impedance spectra could be reliably interpreted in terms of corrosion rate and oxide film thickness.

Direct impedance measurements were also performed in a three-electrode configuration for steel coupons embedded in grout. Again, to facilitate interpretation of the results, only the circular cross-section of the steel strand was exposed to the grout. The impedance was found to be sensitive to steel condition. Interpretation of impedance spectra in terms of corrosion detection was verified by observation of corrosion in optical images taken after the cell was dismantled.

Indirect impedance measurements were performed on synthetic tendons in which a single steel strand was stretched within a grout-filled concentric HDPE conduit. Corrosion was induced by passing direct current between iridium-oxide-coated titanium plugs, which served as the cathode, and the steel strand, which served as the anode. After the experiment, the tendon was destroyed to allow optical imaging of the steel tendon. The indirect impedance was found to be locally sensitive to locations in which corrosion could be visually identified. Surprisingly, the corrosion was not centered under the plugs serving as the cathodes, as would be expected if the current distribution was caused by the ohmic resistance of the grout. Instead, corrosion was distributed randomly, suggesting that corrosion was controlled by local variations of steel properties. This interpretation is consistent with the observations for steel in simulated pore solutions. The four-electrode indirect impedance technique was found to be sensitive to corrosion if it occurred directly under one of the current injection electrodes.

Numerical finite-element simulations confirmed that indirect impedance is sensitive to corrosion under the current-injection electrodes and insensitive to corrosion in other locations. Thus, indirect impedance for steel strands in grout-filled plastic conduits represents a

highly localized measurement.

To explore its potential for use in bridges, the indirect impedance technique was applied to sections of tendons taken from the Ringling Bridge Causeway. Practical tendons encompass many steel strands, as compared to the single strand employed in the synthetic tendons described in the previous experiments. One of the sections showed clear evidence of grout segregation and associated corrosion. Indirect impedance measured directly above the corroded section gave results that could be differentiated from measurements made above steel strands with normal appearance. However, these differences could be seen only if the corroded strand was located near the measurement location. Impedance measurements made at the opposite location, e.g., 180° from the corrosion, were not influenced by corrosion. These observations were confirmed by finite-element modeling.

The indirect impedance technique was applied as well to tendons of a mock bridge constructed at the Texas A&M University under the direction of Prof. Stefan Hurlebaus. While the impedance response showed some correlation to pre-fabricated faults, the methods used to simulate corrosion of steel strands were unlikely to generate the active corrosion needed to trigger changes in the impedance response.

The general conclusion of the present study is that indirect impedance provides a means of detecting corrosion in tendons if the corroding strands are located near the grout–duct interface and are directly under one of the two current injection electrodes. Greatest sensitivity was seen at frequencies at or below 1 Hz. The indirect impedance approach is only qualitative because the grout impedance obscures quantification of the corrosion rate. Corrosion of strands in the center of a duct containing many strands cannot be detected by indirect impedance. These conclusions are supported by experimental observations and numerical simulations. Thus, indirect impedance may be useful if corrosion can be anticipated to occur in response to grout segregation, for which corroding strands will be located near the top of tendons.

While there are many difficulties with the application of indirect impedance to corrosion detection in tendons, there are still clear advantages over existing technologies. The procedure for the indirect impedance measurement is relatively simple and does not require heavy equipment. The instrumentation required can weigh less than 20 pounds. Measurements are performed in approximately 20 minutes, and the holes that are drilled can be sealed if desired.

The present study also made contributions to the general understanding of this system. Models were developed to interpret the impedance response for steel disk electrodes in simulated pore solutions and in grout. These models could be used to extract corrosion rate and oxide film thickness. The oxide resistivity at the oxide–electrolyte interface, an important parameter in the power-law model, was shown to be a property of the steel. Despite different silicon content in nominally identical steels, different film thicknesses as observed by HAADF-STEM, and different impedance responses, three samples yielded a common value for oxide resistivity at the oxide–electrolyte interface. Numerical simulations provided an explanation for the frequency dispersion associated with the grout. The nonuniform current and potential distributions yielded a frequency-dependent complex ohmic impedance associated with current pathways through the grout. This work showed why the indirect impedance was most sensitive to corrosion taking place directly underneath the current injection electrodes.

Table of Contents

List of Figures

List of Tables

Chapter 1

Introduction

The exploration of the feasibility of using indirect impedance to detect corrosion involved both investigation of its application to post-tensioned tendons used in segmentally constructed bridges and fundamental studies of the nature of corrosion in the tendon environment. A discussion of corrosion problems associated with segmental-precast box-girder bridge construction is presented in this chapter. In addition, a review is presented of prior research on corrosion (taken from Chen and Orazem[5]) and associated passive films formed on steel in alkaline media (taken from Chen et al.[7]).

1.1 Tendons in Segmentally Constructed Bridges

External post-tensioned tendons are used in segmental-precast box-girder bridge construction to hold segments together and to prevent stress cracking. An alkaline grout is intended to provide protection against corrosion, but, due to possible voids in the grout and areas of improper mixing, cases of severe corrosion have occurred. Precast segmental bridges are constructed by connecting precast concrete members to form the span of the bridge between piers or columns which support the span. The term precast means that the concrete segments are built prior to being set in place. The segments are fastened together with the use of longitudinal post-tensioned tendons.

Concrete is a brittle material that cracks under tension but can withstand large compressive forces without any structural damage. Therefore, steel reinforcement is used to withstand any tensile forces the structure may experience. However, for the tensile load to be transferred to the steel under normal or unstressed reinforcement, the concrete has to crack. By stressing the steel within the tendons and forcing the concrete into compression, the tensile forces are transferred to the steel prior to the concrete cracking which greatly improves the durability of the bridge and allows for longer bridge spans. The ends of the tendons are anchored at bulkheads and stressed, after which the duct is filled with cementitious grout.[8]

Two classifications of tendons may be used, including external and internal tendons. Internal tendons are placed within the concrete segments through holes which are pre-formed into the concrete segments. External tendons are usually placed within the inner openings of the segments but are external to the concrete. The tendons consist of multiple 7-wire pre-stressing strands contained within a high-density polyethylene (HDPE) duct. They run continuously through deviator blocks which help form the profile of the tendon. The tendons may either be bonded or unbonded, meaning grout is used to fill the space between the duct and the steel (bonded) or is left empty (unbonded). The tendons are called post-tensioned because, after they are in place, the steel within the tendon is pulled into tension using a high strength jack. Stretching the steel strands forces the concrete segments into compression.

Despite the use of grout to prevent corrosion, there have been many cases in which corrosion has still occurred. Some of the causes of corrosion within post-tensioned tendons include voids in the grout, grout bleed water, cracks in the duct, and grout segregation. Voids in the grout can be caused by the adsorption of bleed water, and grout segregation is usually caused by improper grout mixing procedures.[9]

Since post-tensioning technology is still relatively new, corrosion problems were not evident until the 1980s. The first instance occurred in 1980 when the southern outer roof of the Berlin Congress Hall collapsed 23 years after it was constructed.[10] Soon thereafter, two bridges were found with similar serious corrosion issues: the Taf Fawr Bridge on A470 in Wales, England, and the Angel Road Bridge on the A406 North Circular in London, England.[11] Ultimately, the Taf Fawr Bridge was demolished in 1986 while the Angel Road Bridge was significantly retrofitted in 1982. In 1985, the single-span segmental post-tensioned Ynys-y-Gwas Bridge in Wales collapsed as a result of corrosion of longitudinal tendons at its segmented joints. This structure was only 32 years old, and there had been no previous indication of distress prior to collapse.[12] In 1992, the British Department of Transportation conducted a study on these corrosion issues and concluded that there was no method that could guarantee complete corrosion prevention. Later that year, post-tensioned bridges were effectively banned in the United Kingdom.[13]

The United Kingdom was not the only country with post-tensioned bridge issues. The post-tensioned Melle Bridge, which was built in Belgium in 1956, collapsed in 1992. In this instance, the bridge had been inspected, load tested, re-waterproofed, declared adequate, and just restored to service two years prior to its collapse.[10] More recently, the Saint Stefano Bridge in Italy[11] and the Lowes Motor Speedway footbridge in North Carolina[14] collapsed due to similar corrosion-related failures.

Corrosion in post-tensioned bridges is a major concern in Florida as well. The first reported post-tensioned corrosion issue was at the 18-year-old Niles Channel Bridge in the Keys.[15,16] Similar issues were reported at the 7-year-old Mid-Bay Bridge in the Western Panhandle[17,8] and the 15-year-old Sunshine Skyway Bridge in Tampa.[16] A number of studies were commissioned by the Florida Department of Transportation (FDOT) to address corrosion issues. An important conclusion from the study related to the Mid-Bay Bridge was that a non-destructive technique for testing corrosion and corrosion-risk in these post-tensioned members was required.

In 2006, FDOT and researchers at the University of Florida tried to develop a nondestructive technique for corrosion detection in post-tensioned members.[18] The study hinged on finding air-voids and/or entrained water in the grout matrix because these variables have been shown to lead to corrosion. A number of methods were used in this study including ground penetrating radar, impact echo, ultrasonic sound waves, and gamma-ray spectroscopy.

Results from this study indicate that, of these methods, only gamma-ray spectroscopy showed any real promise as a possible solution. However, spectroscopy results were preliminary (at best), and were based only on a limited number of laboratory-prepared samples. Furthermore, field-implementation of such a system appeared to be unlikely since it hinged upon using an HPGe detector which required liquid nitrogen (at 77K; -196°C; -321°F). While investigators from the previous study recommended designing a better gamma-ray detector, specifics about exactly how this was to be done were never addressed.

The Federal Highway Administration identified main magnetic flux as a possible nondestructive method for external tendons that is still in need of development.[19] High-powered magnets are used to induce a static magnetic field in the tendon and the magnetic flux, which is a function of steel cross-sectional area, is monitored to detect fractures.[20] Ultrasonic tomography has been used to detect voids within the internal tendons by sending ultrasound waves and measuring the time for them to be transmitted. Differences in the density of media lead to longer transmission times.[21] While these methods are useful in identifying problem areas, only electrochemical techniques such as impedance spectroscopy can yield actual corrosion rates.

In application to reinforced concrete, many methods have been developed to estimate the corrosion rate of the embedded steel. The most notable of these techniques is the Linear Polarization Resistance (LPR) method in which a small over-potential is applied to the reinforcing steel and the current response is monitored. The polarization resistance of the steel is estimated by dividing the potential by the current response. With the relationship,

$$i_{\mathrm{corr}} = B/A * R_{\mathrm{p}} \tag{1.1}$$

developed by Stern and Geary, the steel polarization resistance, R_{p}, is used to estimate the corrosion rate based on the Tafel slope, B. However, the inherent assumption is that the corrosion reaction follows Tafel kinetics. Also, the LPR method requires a connection to the steel to polarize it, but, in reinforced structures, access to the steel can only be provided by cutting through the concrete.

To avoid cutting through the concrete, research has been done to develop a way to indirectly polarize the steel without an electrical connection. An indirect method has been explored in which an electric field is applied to the surface of the concrete and the induced current pulse indirectly polarizes the steel.[22] An alternative to the pulse method is electrochemical impedance spectroscopy, which uses a sinusoidal current or potential perturbation applied to the concrete surface at a range of frequencies to indirectly polarize the steel.[23,24] Monteiro et al.[23] reported using indirect impedance spectroscopy to determine the location and the condition of steel rebar within concrete slabs. They were able to qualitatively determine that the measured surface impedance was a function of the corrosion state of the steel as well as the resistance of the concrete.[23] The object of this work is to apply the indirect impedance measurement to post-tensioned tendons in order to monitor the integrity of the steel and to develop a means of interpreting the response.

1.2 Applications of Impedance to Steel in Alkaline Media

Corrosion of steel strands within the tendons has been attributed to defective grout, including formation of voids by bleed water accumulation and reabsorption as well as areas of un-hydrated grout which has been termed deficient.[25] Recent examinations of failed tendons suggested that the deficient grout has high moisture content, a high pore solution pH, a low chloride concentration, and a high sulfate concentration.[9] Bertolini and Carsana suggested that corrosion of post-tensioned steel in deficient grout is initiated in highly alkaline environments by the large cathodic polarization that may exist in oxygen-deficient environments.[26] Hope et al.[27] suggested that penetration of moisture and chlorides to a localized area may form an aggressive environment resulting in corrosion.

The corrosion of post-tensioned steel may be related to corrosion of steel reinforcement in concrete, which has been more extensively studied. Due to the natural chemistry of concrete, the pore solution has a high degree of alkalinity. In this environment, steel reinforcement is chemically protected by a passive film and exhibits high corrosion resistance.

Electrochemical impedance spectroscopy is widely used to model and estimate corrosion rates from the anodic reaction resistance, $R_{\mathrm{t,a}}$, extracted from a fitting procedure. Sánchez et al.[28] suggested that an equivalent circuit with two RC loops connected in parallel could be used to model the spontaneous growth of a passive layer. However, a Warburg element must be added in series with charge transfer resistance in the circuit when the passive layer was formed under anodic polarization. Flis et al.[29] reported that, in Nyquist format, the low-frequency impedance presented an angle between 25 and 70 degrees with respect to the real axis, depending on immersion time and the charge transfer resistance. They suggested that the higher slope corresponded to better protective properties of the surface film. Dhouibi et al.[30] conducted impedance measurements to determine the long-term effectiveness of two corrosion inhibitors, calcium nitrate and alkanolamine, for carbon steel in concrete. Their impedance results showed that the steel–concrete interface response contained two or three loops. The resistance corresponding to the polarisation resistance of the steel decreased with time in chloride solution, suggesting that inhibitors did not prevent the corrosion process when chloride is present. Pech-Canul and Castro[31] conducted impedance measurements for carbon steel in concrete with different water/cement ratio exposed to a tropical marine atmosphere. Their work suggested that a Randles circuit modified with a constant-phase element could be used to fit impedance data.

1.3 Use of Impedance to Assess Oxide Film Thickness

Electrochemical impedance measurements provide a means to interrogate electrochemical systems, yielding spectra that are influenced by properties of the system under study.[32–35] For passivated metals subject to corrosive environments, the impedance spectra can provide information concerning the properties of the passive film. These spectra, however, typically reveal the influence of a distribution of time constants that can often be represented by a constant-phase element (CPE). The impedance for a film-covered electrode showing CPE behavior may be expressed in terms of ohmic resistance R_{e}, a parallel resistance $R_{||}$, and CPE parameters α and Q as

$$Z = R_{\mathrm{e}} + \frac{R_{||}}{1 + (\mathrm{j}\omega)^{\alpha} R_{||} Q} \tag{1.2}$$

where ω is the frequency in units of s^{-1}.[36] When $\alpha = 1$, the system is described by a single time-constant, and the parameter Q has units of capacitance; otherwise, Q has units of

$\mathrm{s}^{\alpha}/\Omega\mathrm{cm}^2$ or $\mathrm{F}/\mathrm{s}^{(1-\alpha)}\mathrm{cm}^2$.[34,35] Under conditions that $(\omega)^{\alpha}R_{||}Q \gg 1$,

$$Z = R_{\mathrm{e}} + \frac{1}{(\mathrm{j}\omega)^{\alpha}Q} \tag{1.3}$$

which has the appearance of a blocking electrode. The term $R_{||}$ in equation (1.2) accounts for a resistance that may be attributed to current pathways that exist in parallel to the dielectric response of a film.

The problem of interpretation of CPE parameters in terms has attracted substantial attention. For example, Brug et al.[37] developed a relationship for capacitance in terms of CPE model parameters under the assumption that time constants were distributed along the surface of the electrode. Hsu and Mansfeld[38] developed a relationship under the assumption that time constants were distributed within a film in the direction perpendicular to the surface of the electrode. Jorcin et al.[39] used local electrochemical impedance spectroscopy (LEIS) to distinguish between CPE behavior associated with time-constant distributions along the electrode surface or in the direction perpendicular to the electrode surface.

Hirschorn et al.[1,2] suggested that the time-constant distribution in a film can be expressed in terms of a modified power-law distribution of resistivity, given as

$$\frac{\rho}{\rho_\delta} = \left(\frac{\rho_\delta}{\rho_0} + \left(1 - \frac{\rho_\delta}{\rho_0}\right)\xi^{\gamma}\right)^{-1} \tag{1.4}$$

where ρ_0 and ρ_δ are the boundary values of resistivity at the interfaces, such that $\rho_0 > \rho_\delta$. Under the assumption that

$$R_{||} \ll g\delta\rho_\delta^{(1-\alpha)}\rho_0^{\alpha} \tag{1.5}$$

a relationship among the CPE parameters Q and α and the dielectric constant ϵ, resistivity ρ_δ, and film thickness δ was found to be

$$Q = \frac{(\epsilon\epsilon_0)^{\alpha}}{g\delta\rho_\delta^{1-\alpha}} \tag{1.6}$$

where

$$g = 1 + 2.88(1-\alpha)^{2.375} \tag{1.7}$$

The corresponding expression for effective capacitance was given as

$$C_{\mathrm{eff,PL}} = gQ\left(\rho_\delta\epsilon\epsilon_0\right)^{1-\alpha} \tag{1.8}$$

The development of equation (1.6) does not require values for the characteristic frequency; thus, the results depend only on the high-frequency data. In addition to the CPE parameters Q and α, $C_{\mathrm{eff,PL}}$ depends on the dielectric constant ϵ and the smaller value of the resistivity ρ_δ.

While the dielectric constant may be known for some films, the value of ρ_δ is not generally known. Thus, equation (1.6) may be described as a single equation with two unknown parameters, δ and ρ_δ. In spite of this difficulty, the power-law model for interpretation of CPE parameters has found application for oxide films on steel,[36] human skin,[36,40,41] and coatings,[42–44] and has even found commercial application.[45] Orazem et al.[46] addressed the difficulties in applying equation (1.6) associated with uncertain values for the resistivity ρ_δ. The usual approach is to estimate a value of ρ_δ by performing a calibration experiment in which XPS is used to estimate film thickness for a coupon for which impedance measurements were made,[36,47] apply equation (1.6) to estimate ρ_δ for a specified dielectric constant, and then to assume that this value of ρ_δ applies for all other impedance measurements.

The system under study in the present work was an ASTM A416 steel in an alkaline electrolyte chosen to simulate the pore solution for a cementitious grout. The corrosion behavior of carbon steel in highly alkaline environment ($pH > 12$) is controlled by a passive iron oxide film. Montemor et al.[48] used Auger electron spectroscopy (AES) and X-ray photoelectron spectroscopy to study the effect of chloride (Cl^-) and fly ash on behavior of the passive film formed on steel in solutions simulating the concrete interstitial electrolyte. Their work suggested that the outermost layers of the passive films formed on the steel in cement paste solutions were essentially composed of FeOOH. Ghods et al.[49] investigated passivity and chloride-induced depassivation of carbon steel in simulated concrete pore solution ($pH=13.3$). Their work suggested that the oxide films close to the steel substrate were mainly composed of protective Fe^{2+} oxides; whereas, the film near the free surface consisted mostly of Fe^{3+} oxides. This duplex structure was also reported by Haupt and Strehblow[50] for the passive film on 99.99% iron in 1M NaOH. They reported that the ratio Fe^{3+}/Fe^{2+} and the oxide film thickness increased with applied potential and that Fe^{2+} oxide is negligible for an applied potential greater than +0.2 V(SHE). Schmuki et al.[51] investigated passivity of iron in 0.1 M NaOH by in-situ X-ray absorption near edge spectroscopy and a laser reflection technique. Their work suggested that a 10 nm iron film can convert completely to an oxide film from the metallic state and a porous Fe^{2+}-oxide/hydroxide film was formed at potentials smaller than −1.4 V(MSE).

The oxide film thickness may be estimated from Fe 2p spectra as measured by X-ray photoelectron spectroscopy (XPS). The accuracy of the thickness values obtained from the Fe 2p spectrum reconstruction decreases with increasing film thickness, with best accuracy for film thickness between 1 and 4 nm.[52] Ghods et al.[49] used the Fe 2p spectra of XPS to suggest that the oxide film thickness of carbon steel in simulated concrete pore solution ($pH = 13.3$) is about 5 nm. Montemor et al.[48] suggested that the passive film formed on a carbon steel in solutions simulating the concrete interstitial electrolyte is about 80 to 110 nm.

As the oxide film thickness on carbon steel is usually smaller than 5 nm, direct imaging of the film requires use of electron microscopy. Gunay et al.[53] used annular dark field scanning transmission electron microscopy (ADF-STEM) and electron energy loss spectroscopy (EELS) to investigate the atomic structure of oxide films formed on carbon steel exposed to highly alkaline simulated concrete pore solutions. The images of the oxide film showed three different layers with total thickness close to 10 nm. In the presence of saturated $Ca(OH)_2$ solution, the outer layer of the oxide film consisted of Fe_3O_4, and the outer layer consisted of α-Fe_2O_3/Fe_3O_4 in simulated concrete pore solution. The composition of the intermediate layer was Fe_3O_4, and inner layer was FeO. Khaselev and Sykes[54] used in-situ electrochemical scanning tunneling microscopy to take images of the iron surface after conducting cyclic voltammetry. Their work suggested that formation of facets can be observed on surface of iron after cycling to -0.95 V(Ag/AgCl), but the surface of iron became smooth again after sweeping to -0.80 V(Ag/AgCl).

The properties of oxide films on iron and carbon steel have also been studied by different electrochemical approaches. Sánchez et al.[28] used EIS to analyze two different cases of passive films: a passive layer spontaneously grown in a high alkaline media and a passive layer assisted by the application of an anodic potential in the same media. Freire et al.[55] conducted impedance measurements for AISI 1040 mild steel at -0.2 V(SCE) and +0.2 V(SCE) in 0.1M NaOH + 0.1M KOH after 3 days of immersion. They reported that the impedance results suggested a partial coverage of oxide film on the surface, which corresponded to atomic force microscopy results. Chen and Orazem[5] conducted impedance measurements for ASTM A416 steel in simulated pore solution. Their work suggested that the impedance responses of ASTM A416 steel showed porous electrode behavior that diminished with time, and, from their impedance results, corrosion rate and oxide film thickness of ASTM A416 steel were estimated.

Chapter 2

Bench-Top Experimentation

The electrochemistry of ASTM A416 steel was studied in simulated pore solutions intended to mimic the electrolyte within cementitious pores. This work showed the presence of subtle differences between different batches of steel with nominally the same composition. This work was also used to explore the use of the power-law model as a means to extract the thickness of oxide films. ASTM A416 steel disk electrodes were also exposed to grout to determine the sensitivity of impedance measurements to corrosion.

2.1 Disk Electrodes in Simulated Pore Solutions

The objective of this work is to explore the use of high-angle annular dark field scanning transmission electron microscopy (HAADF-STEM)[56] to image the oxide film on ASTM A416 steel and to use repeated measurements to explore the extent to which ρ_δ may be considered a property of the oxide film. The value of ρ_δ was then used to explore the influence of system properties on the oxide film grown in alkaline simulated pore solution. This work was published by Chen et al.[7] and represents an extension to the work performed in the previous FDOT contract (see Orazem et al.[57]) and published by Chen and Orazem.[5]

2.1.1 Experimental

The calibration experiments performed included impedance measurements on a specimen subsequently subjected to surface analysis to identify composition and film thickness. The coupon size was constrained by the need to conform to the sample requirements of the analytical instrumentation. The other experiments were performed on cylindrical specimens encased in epoxy to expose the face of the cylinder to the electrolyte. The chemical composition of the simulated pore solution and the nominal composition of the ASTM A416 steel are presented in this section. The exposure time for the calibration experiments was limited to 24 hours; whereas, much larger exposure times could be achieved with the insulated cylindrical specimens.

Table 2.1: Chemical composition of simulated pore solution and the resulting pH value.

KOH	NaOH	$Ca(OH)_2$	pH
23.3(g/L)	8.33 (g/L)	2 (g/L)	13.8

Table 2.2: Nominal chemical composition of ASTM A416 steel. The remainder was Fe.[4]

Element	C	Si	Mn	P	Cu	S
weight %	0.75-0.81	0.26-0.28	0.62-0.84	0.012-0.021	0.01-0.02	0.018-0.028

Materials

The procedure for preparation of simulated pore solutions, following the recipe presented by Li and Sagüès,[58] was that reported by Chen and Orazem.[5,7] The electrolyte composition is presented in Table 2.1. This solution was intended to simulate the environmental conditions for steel strands within cement grout. A 5 mm × 50 mm platinum sheet was used as the counterelectrode. The reference electrodes employed were mercury/mercuric oxide (1 M KOH) and saturated calomel (SCE). The working electrode was a 5 mm diameter, ASTM A416 steel rod (Sumiden Wire Products) embedded in epoxy resin to expose the circular face of the rod. The nominal composition of the ASTM A416 steel is presented in Table 2.2. While nominally the same, the properties of the steel specimens showed some variability. The XPS analysis, presented in subsequent sections, suggests that Si can be detected from one steel but cannot be detected from the other. For the present work, the ASTM A416 steel for which Si could be detected is termed Steel No. 1; whereas, the ASTM A416 steel, whereas, for which Si could not be detected is termed Steel No. 2.

Instrumentation

A Gamry reference 600 potentiostat was used to conduct all electrochemical measurements. A VWR Scientific Model 1160 temperature controller was used to control the electrolyte temperature at 298±1 K.

Electrochemical Protocol

The working electrode was polished sequentially with #120, #320, #600, #800 and #1200 grit silicon carbide papers to yield a smooth working electrode surface. After the previous procedure, the steel surface was further polished by 1 μm alumina powder to a achieve mirror finish. The working electrode was subsequently degreased with ethanol and washed with water before each experiment. Experiments were performed with a stationary electrode.

Cathodic pre-treatment was applied to the working electrode at -1.1 V(Hg/HgO) for one hour to remove any oxide film that may have formed on the specimen surface. Impedance measurements were taken with frequencies ranging from 500 Hz to 0.05 Hz and with a perturbation amplitude of 5 mV after an elapsed time at least 2 hours.

The frequency range used for regression analysis was constrained by the characteristic frequency associated with geometry-induced frequency dispersion. The frequency at which the current and potential distributions begin to influence the impedance response can be expressed as[35, 59]

$$f_{\mathrm{c,disk}} = \frac{1}{2\pi}\frac{\kappa}{C_0 r_0} \tag{2.1}$$

where κ is the electrolyte conductivity, C_0 is the electrode capacitance, and r_0 is the radius of the disk electrode. The influence of high-frequency geometry-induced time-constant dispersion can be avoided for reactions that do not involve adsorbed intermediates by conducting experiments below the characteristic frequency given in equation (2.1). For example, from the values of the regressed parameters of impedance data after 300ks in Table 2.4, the characteristic frequency is 2.2 kHz. While the maximum frequency reported for most measurements was 500 Hz, some measurements for No. 2 steel had a maximum frequency of 10 kHz. To eliminate the confounding effect of geometry-induced frequency dispersion, such impedance data were truncated by removing data measured at frequencies higher than 2.2 kHz.

Calibration Experiments. To obtain values for ρ_δ, the steel was cut to a 5 mm diameter cylinder with the height smaller than 5 mm, and the polished disk side was placed in contact with the simulated pore solution such that surface tension forces kept the face of the electrode exposed to the electrolyte and the sides of the cylinder were not immersed. The coupon was immersed in electrolyte for an elapsed time of 24 h, sufficient to establish a stable oxide film. After 24 h, impedance measurements were performed, and the electrode was removed from electrolyte, rinsed successively with deionized water, ethanol, and deionized water, and allowed to air dry before surface analysis was performed.

Corrosion Studies. The electrochemical techniques employed included measurement of polarization curves, linear sweep voltammetry, cyclic voltammetry, and electrochemical impedance spectroscopy.

Surface Analysis

The oxide film was analyzed ex-situ by several different techniques. The chemical composition of the oxide film was investigated by X-ray photoelectron spectroscopy (XPS). The oxide film thickness was analyzed by high-angle annular dark-field scanning transmission electron microscopy (HAADF-STEM). A focused-ion beam was used for specimen preparation.

X-Ray Photoelectron Spectroscopy. A ULVAC-PHI 5000 VersaProbe II was used to perform the XPS analysis using monochromatic Al X-rays and a spot size of 200 μm in diameter. The X-ray gun was operated at 43.9 W. The chamber pressure during analysis was kept below 1×10^{-6} Pa with a pass energy of 93.90 eV. The survey scans were performed at the emission angles of 45°.

Focused-Ion Beam Specimen Preparation. An FEI DB235 dual-beam scanning electron microscope / Ga^+ FIB was used to prepare cross-sectional specimens for TEM and HAADF-STEM imaging using an in-situ lift-out method described elsewhere.[60] Prior to performing FIB milling, the surface of the specimens was protected via in-situ electron-beam-assisted deposition of Pt or via ex-situ sputter deposition of AuPd. The final stages of FIB milling were performed using a 5 keV Ga^+ beam to reduce the final damage layer of the specimen.[60]

HAADF-STEM. A JEOL 2010F transmission electron microscope operating at 200 kV was used to perform HAADF-STEM imaging. HAADF-STEM images were collected using an Oxford Instruments digital image-capturing device.

2.1.2 Results

Results are presented for the calibration experiments, in which coupons were examined by electrochemical methods before being subjected to surface analysis, and corrosion experiments in which electrochemical methods are used to explore the properties of ASTM A416 steel in alkaline electrolyte.

Calibration Experiments

The purpose of the calibration experiment was to obtain a value for the parameter ρ_δ which can be used to extract oxide film thickness from CPE parameters. EIS measurements were performed on the coupon to obtain CPE parameters α and Q. HAADF-STEM was employed to obtain film thickness, and XPS was employed to identify composition differences between No. 1 and No. 2 steel.

Impedance Spectroscopy. Nyquist plots are presented in Figure 2.1 for the impedance data collected in the calibration experiments after an elapsed time of 24 h. The solid lines represent the fit of the process model discussed in a subsequent section. The corresponding ohmic-resistance-corrected phase angle and magnitude are shown in Figure 2.2. The solid lines represent the fit of the process model discussed in a subsequent section and provide excellent fits to the data throughout the measured frequency range. The labels 2(a) and 2(b) in Figure 2.1 represent two samples of #2 steel, with measurements performed using the same protocol. Measurements performed on the same coupon were very reproducible; thus, these differences represent differences between two coupons with the same nominal composition.

The oxide film thickness δ was estimated from CPE parameters by use of the model developed by Hirschorn et al.[1,2] in which the oxide resistivity was assumed to have a modified power-law dependence on position. The oxide film thickness can be estimated from

$$\delta = \frac{(\varepsilon\varepsilon_0)^\alpha}{gQ\rho_\delta^{1-\alpha}} \tag{2.2}$$

Equation (2.2) requires values for the dielectric constant, assumed to be uniform, and the resistivity at position $y = \delta$. Based on the cyclic voltammetry results presented in a subsequent section, the dielectric constant of the oxide was assumed to be that of magnetite, i.e., $\epsilon = 20$).[61]

Surface Analysis. The properties of the oxide film on ASTM A416 steel exposed to simulated pore solution were analyzed by several different approaches. The chemical composition of

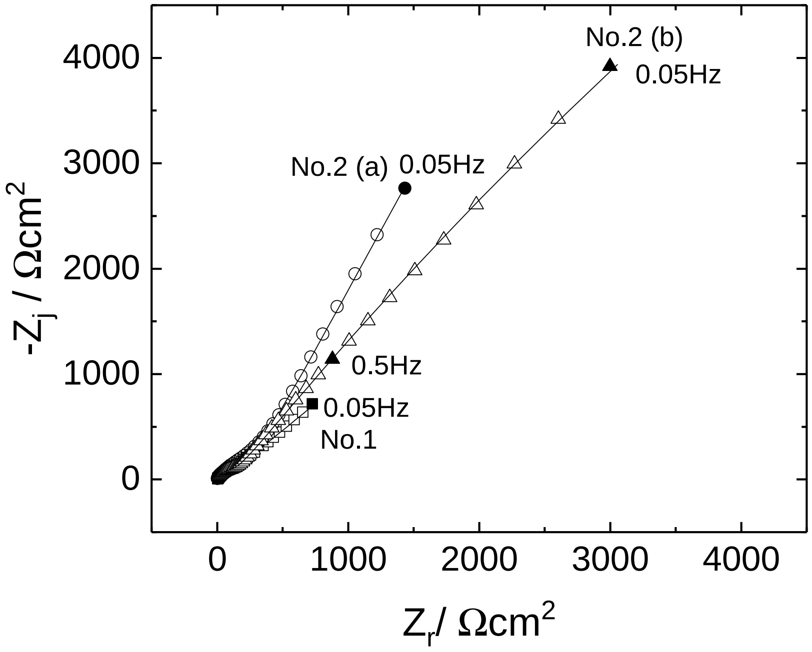

Figure 2.1: Nyquist representation of the impedance data from No. 1 and No. 2 steel after 24 hours of elapsed time for oxide film thickness calibration. The solid lines represent the process model fits.

the oxide film was investigated by XPS. The oxide film thickness was analyzed by HAADF-STEM.

High-Angle Annular Dark-Field Scanning Transmission Electron Microscopy. The film thickness for the calibration experiments was obtained by HAADF-STEM. The images for No. 1 and No. 2 ASTM A416 steel immersed in simulated pore solution after 24 hours of elapsed time are shown in Figure 2.3. Images shown in Figures 2.3(a) and (b) are from different locations for a single coupon of No. 1 ASTM A416 steel. Images shown in Figures 2.3(c) and (d) are from two different coupons of No. 2 ASTM A416 steel.

Figure 2.3(a) suggests that the oxide film thickness on No. 1 ASTM A416 steel is not uniform. Film thickness values of 3–7 nm may be observed. No visible oxide film can be observed in Figure 2.3(b), taken for the same coupon in a different location. Figures 2.3(c) and (d) suggest that the oxide film thickness for No. 2 ASTM A416 steel at open-circuit potential in simulated pore solution after 24 hours of elapsed time is more uniform and has values of 4 and 3 nm, respectively. The oxide film in Figures 2.3(c) and (d) was more uniform than the oxide film in Figures 2.3(a) and (b), suggesting that the oxide film formed on No. 2 ASTM A416 steel can provide a better protection against corrosion.

The value of δ obtained from HAADF-STEM was used to calibrate equation (2.2) by providing values for ρ_δ. A Monte Carlo simulation was used to explore the propagation of error through equation (2.2) to estimate the uncertainty in the resulting value of ρ_δ. The values of Q and α obtained by regression of the process model to the impedance data shown

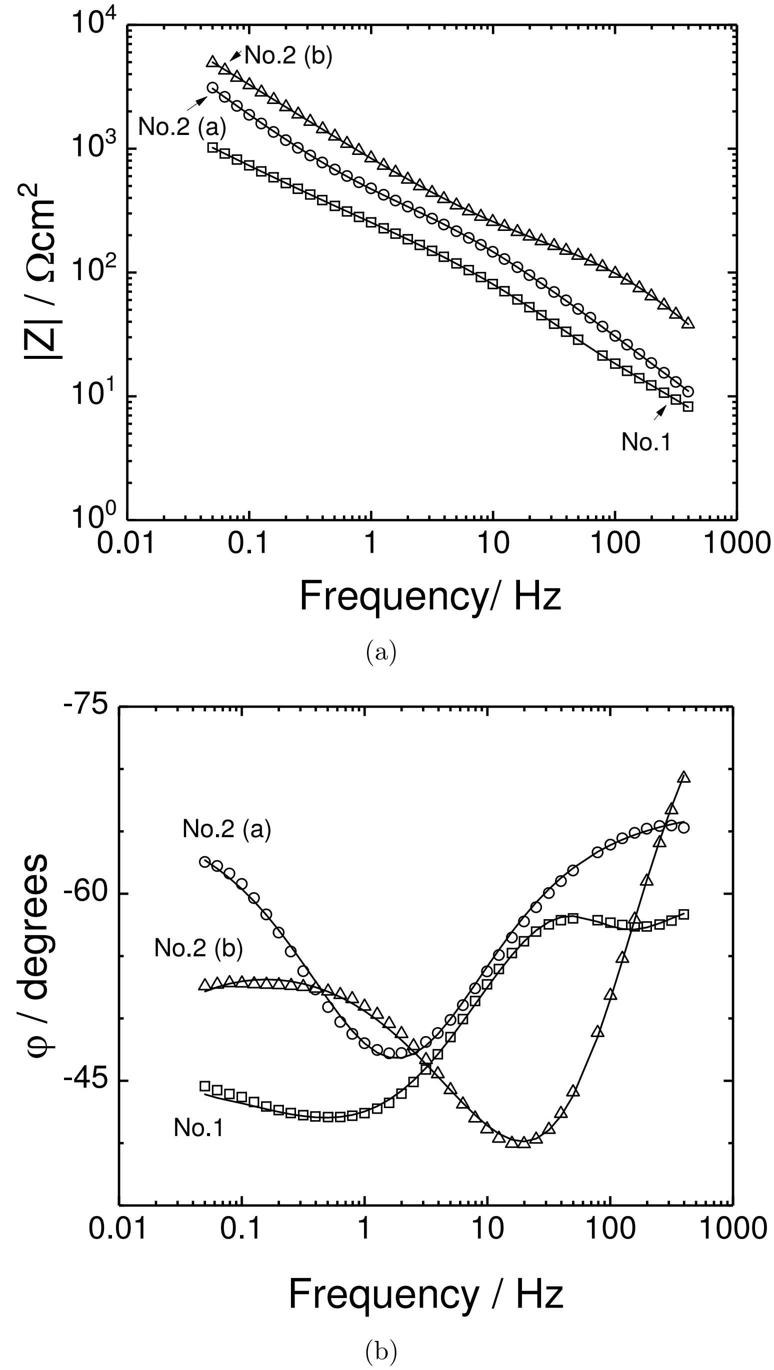

(a)

(b)

Figure 2.2: The phase angle and the magnitude of the impedance data shown in Figure 2.1. The solid lines represent the process model fits.

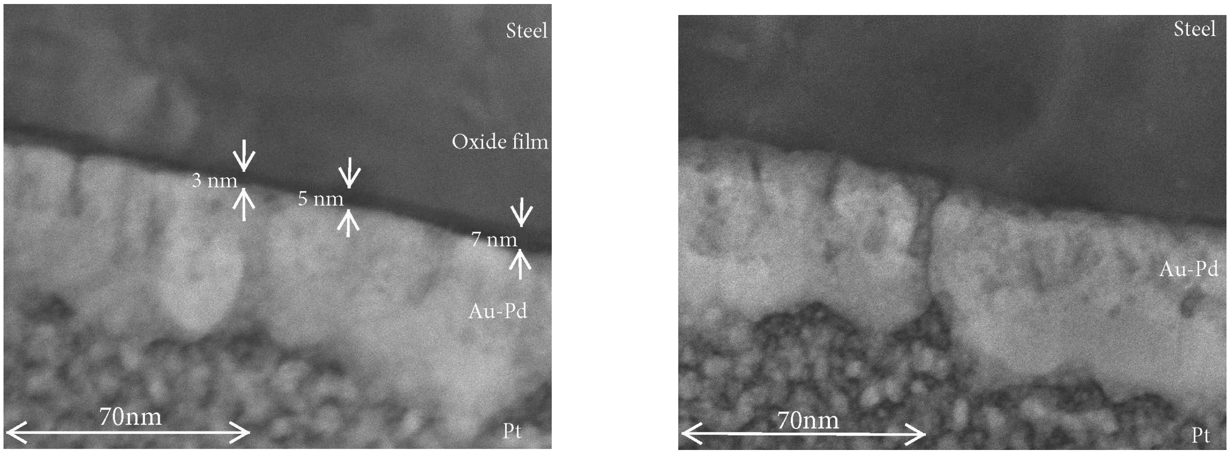

(a) Steel 1 (b) Steel 1

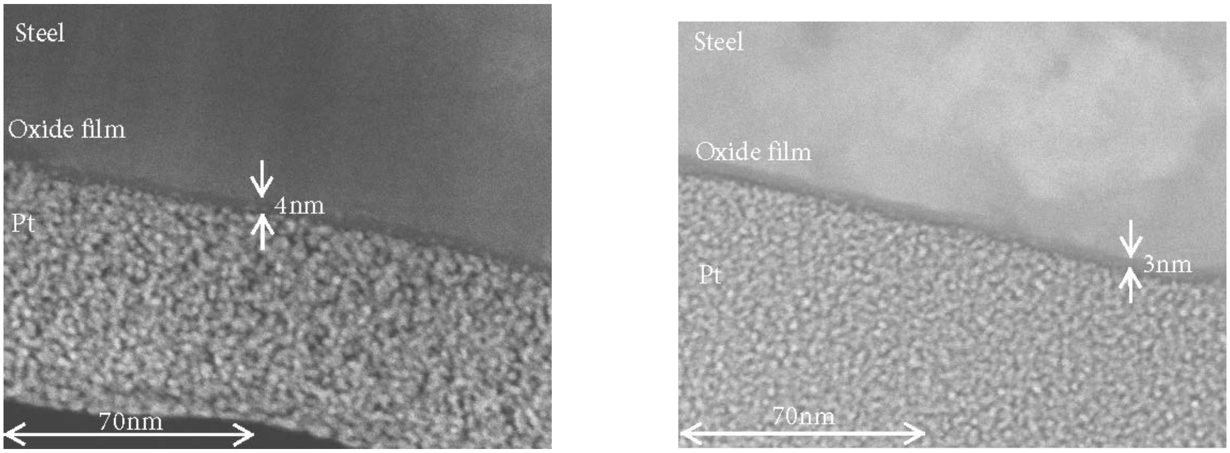

(c) Steel 2a (d) Steel 2b

Figure 2.3: HAADF-STEM images at 100,000X magnification of steel coupons following 24 hours immersion in simulated pore solution. Images (a) and (b) are from different locations for a single coupon of No. 1 ASTM A416 steel. Images (c) and (d) are from two different coupons of No. 2 ASTM A416 steel.

Table 2.3: Regressed CPE parameters, film thickness obtained by HAADF-STEM, and resulting resistivity of oxide film at the film–electrolyte interface as obtained from equation (2.2).

		No. 1 steel	No. 2 steel (2a)	No. 2 steel (2b)
α	–	0.71±0.006	0.75±0.01	0.92±0.007
Q	$\mathrm{mF/s^{(1-\alpha)}cm^2}$	0.42±0.017	0.26±0.05	0.018±0.0012
δ	nm	5±1	4±0.5	3±0.5
$\ln(\rho_\delta/\Omega\mathrm{cm})$		10.2±0.8	10.4±1.1	13.1±2.6
ρ_δ	kΩcm	27	34	49

in Figures 2.1 and 2.2 and the values of δ obtained from Figures 2.3 are presented in Table 2.3. The standard deviations for the CPE parameters were obtained from the Levenberg–Marquardt regression, and the standard deviations for film thickness were estimated to be 1 nm for No. 1 steel and 0.5 nm for No. 2 steel.

As shown in Figure 2.4, the resulting values for ρ_δ followed a log normal distribution. Application of the paired Student's t-test showed that the null hypothesis, that the means for $\ln(\rho_\delta)$ are equal, could not be rejected. Thus, the distribution of ρ_δ was assumed to be described by

$$\ln(\rho_\delta/\Omega\mathrm{cm}) = 11.2 \pm 1.53 \tag{2.3}$$

or $\overline{\rho}_\delta = 7.64\times10^4$ Ωcm. This value is substantially larger than the value of 450 Ωcm reported for an oxide on Fe17Cr steel.^{2}

Thus, despite different silicon content in nominally identical No. 1 and No. 2 steel, different film thicknesses as observed by HAADF-STEM, and different impedance responses, the three calibration experiments yielded a common value for ρ_δ, needed for estimations of film thickness by use of equation (2.2). The corresponding characteristic frequency for which CPE behavior reverts to RC behavior is

$$f_\delta = \frac{1}{\rho_\delta \varepsilon \varepsilon_0} = 1.2 \text{ MHz} \tag{2.4}$$

which is well above the measured frequency range. Equation (2.4) serves as a check for internal consistency. The value of $\overline{\rho}_\delta = 7.64 \times 10^4$ Ωcm is consistent with the observation of CPE behavior at the highest measured frequency. The distribution of ρ_δ characterized by equation (2.3) was used in the evaluation of the confidence interval for film thickness in subsequent analyses.

X-Ray Photoelectron Spectroscopy. The XPS diagrams for polished steel are presented in Figure 2.5. The major species detected from Figures 2.5(a) and (b) were carbon and oxygen, with iron as minor species, suggesting the presence of an air-formed oxide. The XPS spectrum for No. 1 ASTM A416 steel showed peaks corresponding to Si, but the spectrum for No. 2 steel did not.

The XPS spectra for two different sections of the No. 2 ASTM A416 steel immersed in simulated pore solution after 8 cycles of cyclic voltammetry are presented in Figure 2.6.

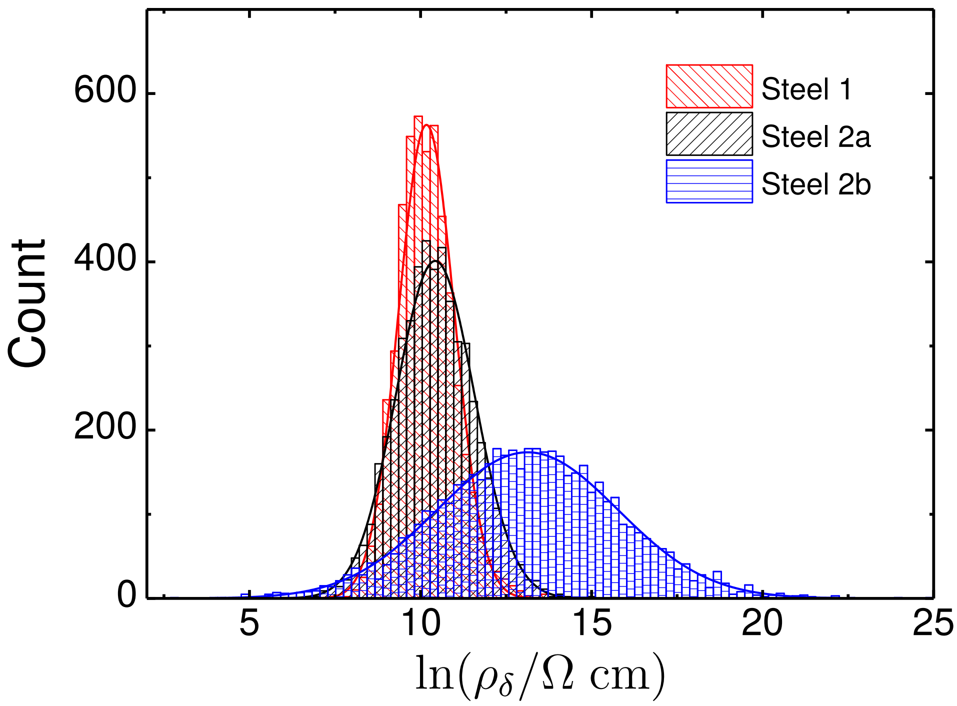

Figure 2.4: The distribution of $\ln(\rho_\delta)$ obtained by Monte Carlo simulations based on parameters extracted from the calibration experiments reported in Table 2.3.

Calcium peaks in Figure 2.6 suggest that calcium is a component of the oxide film. It may be attributed to the deposition of $Ca(OH)_2$ from reaction with hydroxide ions produced by the cathodic oxygen reduction reaction

$$\mathrm{O_2 + 2H_2O + 4e^- \rightarrow 4OH^-} \tag{2.5}$$

As the solubility product K_{sp} for $Ca(OH)_2$ is 6.5×10^{-6},[62] a slight increase of the concentration of OH^- would cause deposition of $Ca(OH)_2$. The presence of $Ca(OH)_2$ in the oxide film suggests that oxide film thickness estimation based on iron peaks of XPS, used by several different studies,[49,63] may be inaccurate.

The precipitation of calcium has been addressed previously. Page[64] postulated that a dense continuous cement-rich layer containing precipitated calcium hydroxide was formed at the steel-concrete interface when concrete was cast against a steel bar. Suryavanshi et al.[65] also found that steel taken from a mortar specimen was covered with a thin dense white deposit, approximately 10 to 15 μm in thickness, which showed a strong calcium peak in the EDX spectrum. However, Glass et al.[66] examined the steel–concrete interface by backscattered electron microscopy and observed no continuous $Ca(OH)_2$ layer.

Application of Electrochemical Methods to ASTM A416 Steel

The electrochemical approaches used in this paper to investigate the corrosion behavior of ASTM A416 steel include polarization curves, linear sweep voltammetry, cyclic voltammetry, and electrochemical impedance spectroscopy.

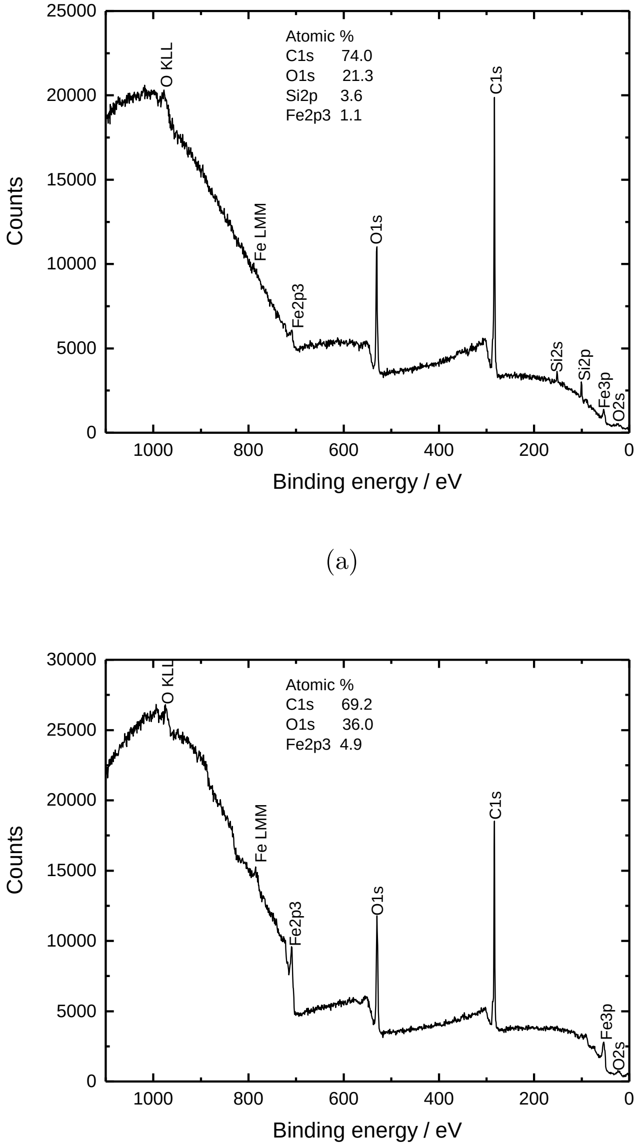

(a)

(b)

Figure 2.5: XPS spectra of polished ASTM A416 steel: (a) No. 1 and (b) No. 2 steel.

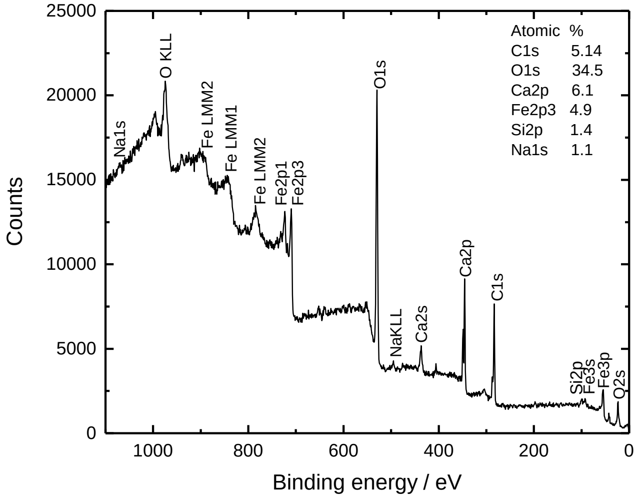

Figure 2.6: XPS spectra of No. 2 ASTM A416 steel received in 2012 immersed in simulated pore solution after 8 cycles of cyclic voltammetry.

Polarization Curve and Linear Sweep Voltammetry. As shown by Chen and Orazem,[5] the polarization curves for steel in alkaline media are strong functions of sweep rate. Thus, the steady-state polarization curve was found by first allowing the system to reach a steady corrosion potential at open circuit and then setting the desired potential and measuring the resulting current until a steady value was achieved. Each measurement began with a freshly polished sample, and the time required for each measurement was on the order of 24–85 hours. The results are presented in Figure 2.7, for No. 2 steel, taken from the present work. The results for No. 1 steel, taken from Chen and Orazem,[5] are added for comparison. The steady-state current for No. 1 steel was found to be about 100 times larger than the steady-state current observed for No. 2 steel, suggesting that the corrosion rate of No. 1 steel was larger than that of No. 2 steel. These results are consistent with the impedance data.

Cyclic Voltammetry. Different peaks were observed for No. 1 and No. 2 ASTM A416 steel. The results of the 8th cycle for No. 1 and No. 2 ASTM A416 steels in simulated pore solution are presented in Figure 2.8. The results obtained in the present work may be compared to the results presented by Joiret et al.[3] Based on a comparison to their work, the possible oxide film compositions for No. 1 steel (labeled (1) in Figure 2.8) are Fe_3O_4, γ-Fe_2O_3, α-FeOOH, FeO, and $Fe(OH)_2$. In contrast, the possible oxide film compositions for No. 2 steel (labeled (2) in Figure 2.8) are FeO, $Fe(OH)_2$ and Fe_3O_4. Analysis of cyclic voltammetry results suggests that the dielectric constant used to assess film thickness from equation (2.2) may be assigned a value of 20, corresponding to magnetite, Fe_3O_4.

Electrochemical Impedance Spectroscopy. The impedance response for both No.1 and No.2 steel disk electrode at the open-circuit potential after an elapsed time of 7.2 ks (2 h) is presented in Figure 2.9, and the corresponding results at the open-circuit potential after a

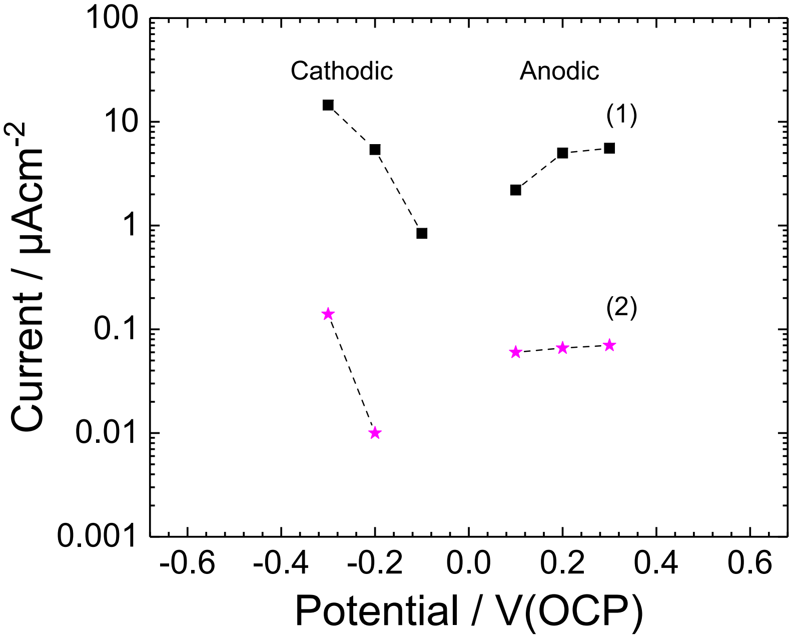

Figure 2.7: Steady-state polarization curves for ASTM A416 steel. The label (1) refers to No. 1 steel, and label (2) refers to No. 2 steel.

steady state was reached are presented in Figure 2.10. After two hours exposure, seen in Figure 2.9, a porous electrode behavior was observed for both No. 1 and No. 2 steels. The porous electrode behavior is represented by an angle with respect to the real axis of 33° (steel No. 1) and 43° (steel No. 2) for data in the frequency range from 10 to 1 Hz (see, e.g., de Levie[67]). The impedance data of No. 1 steel below 1 Hz shown has a slight curvature, suggesting that a finite value for corrosion rate may be estimated.

After steady-state was reached, the low-frequency impedance data collected reveals an angle with respect to the real axis of 44° for steel No. 1 (label (1) in Figure 2.10) or 65° for steel No. 2 (label (2) in Figure 2.10). These results suggest that a porous electrode behavior is evident to a lesser degree for No. 1 steel; whereas, blocking behavior, generally associated with an oxide film, is evident for Steel No. 2. For both cases, the low-frequency data show a straight-line, suggesting that, after 300 ks, the corrosion rates were too small to be measured by impedance within the measured frequency range. Thus, the results presented in Figure 2.10 indicate that the level of passivity of ASTM A416 steel at the open-circuit potential in alkaline simulated pore solution increased with time.

Differences among results presented in Figures 2.1, 2.9, and 2.10 can be attributed in part to differences in elapsed time, i.e., 24 h, 2 h, and 83 h, respectively. While impedance measurements for the same coupon were highly reproducible, some variability was seen for measurements with different steels of the same nominal composition. As shown in the present work, the model used to extract physical parameters could account for these variations.

The imaginary-impedance-derived phase angle and ohmic-resistance-corrected magnitude of impedance are presented in Figures 2.11 and 2.12. The imaginary-impedance-derived

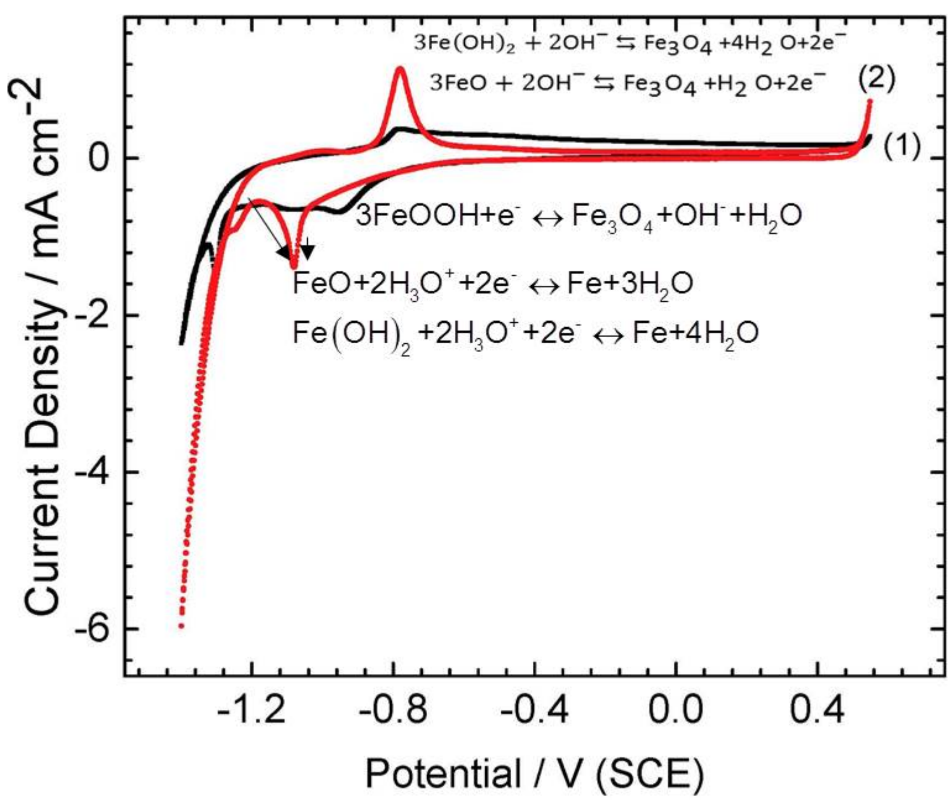

Figure 2.8: The 8^{th} cyclic voltammogram for ASTM A416 steel in simulated pore solution with a scan rate of 10 mV/s. The label (1) refers to No. 1 steel, and label (2) refers to No. 2 steel. The reactions associated with different peaks are taken from Joiret et al.[3]

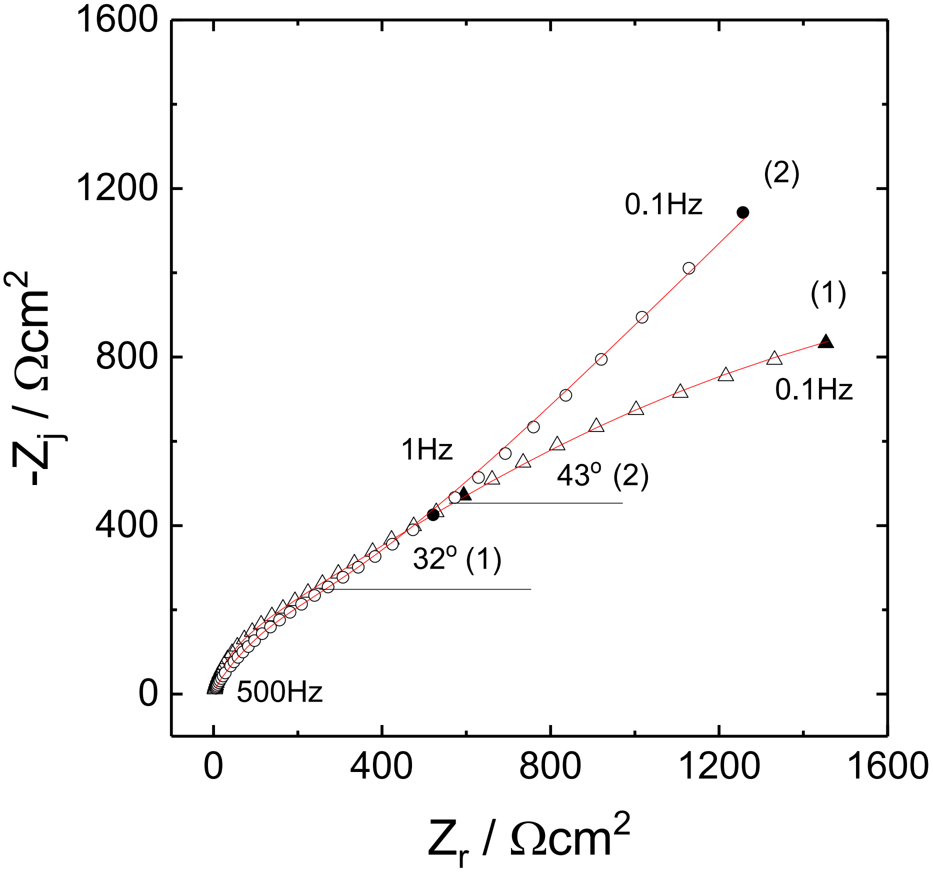

Figure 2.9: Impedance response of the stationary No. 1 and No. 2 ASTM A416 steel disk electrode at the open-circuit potential after an elapsed time of 7.2 ks (2 h). Labels (1) and (2) refer to steels No. 1 and 2, respectively. The lines represent the regression of equation (2.8) to data for steels No. 1 and 2.

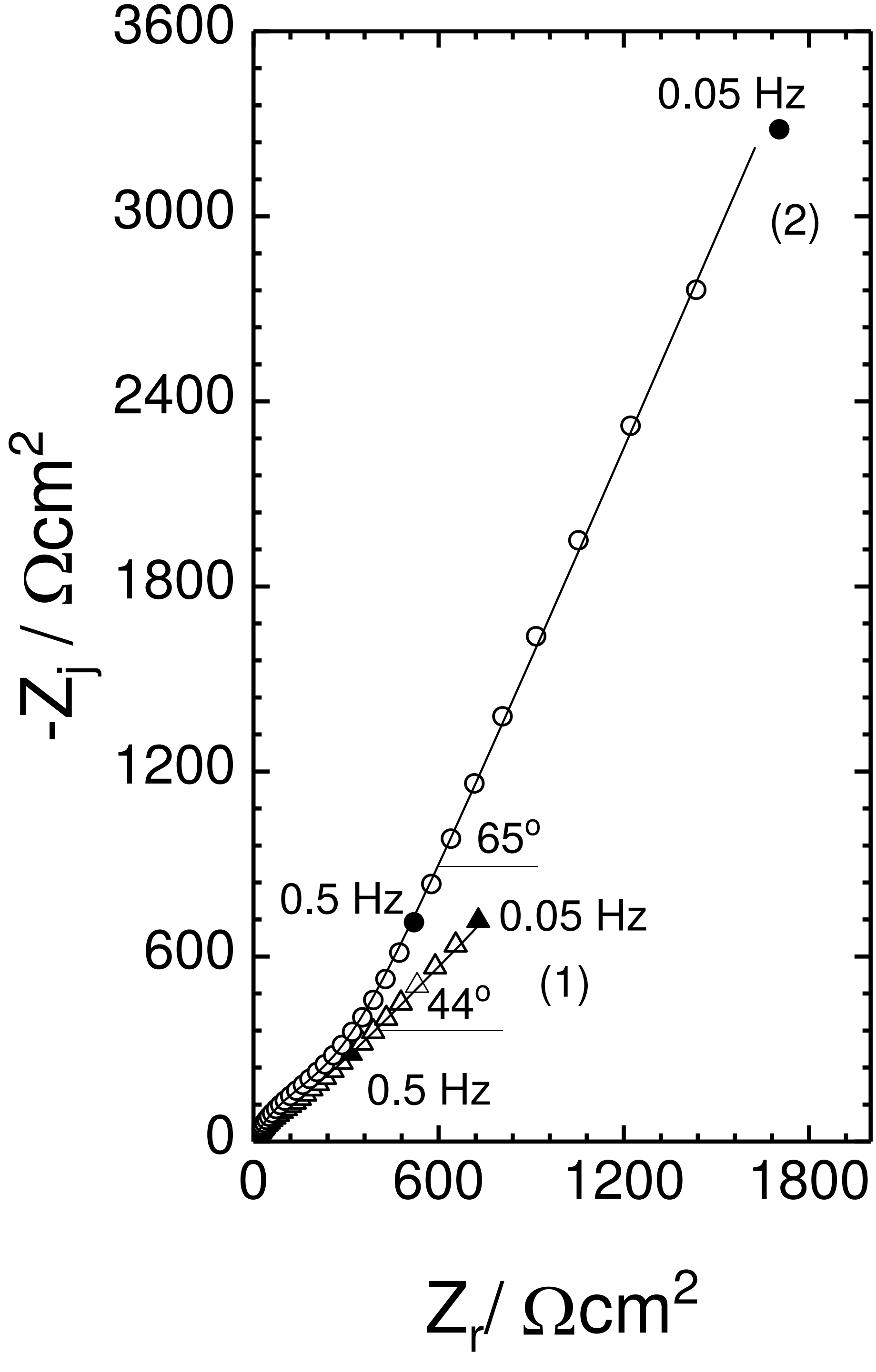

Figure 2.10: Impedance response of the stationary ASTM A416 steel disk electrode at the open-circuit potential after steady-state was reached. Labels (1) and (2) refer to steels No. 1 and 2, respectively. The lines represent the regression of equation (2.8) to data for steel No. 1 and equation (2.16) for steel No. 2.

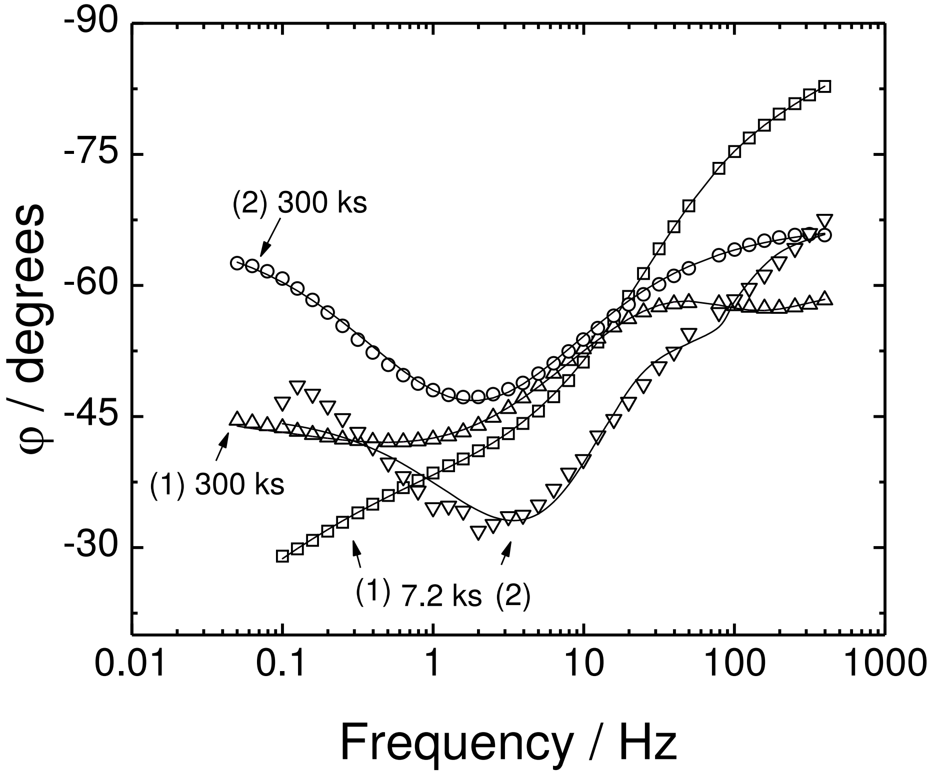

Figure 2.11: Imaginary-impedance-derived phase angle, obtained from equation (2.6), for the stationary ASTM A416 steel disk electrode at the corrosion potential after an elapsed time of 7.2 ks (2 h) and after steady-state was reached. Labels (1) and (2) refer to steels No. 1 and 2, respectively. The lines represent the regression of equation (2.8) to data for steel No. 1 (at 7.2 ks and 300 ks) and steel No. 2 (at 7.2 ks) and equation (2.16) for steel No. 2 at 300 ks.

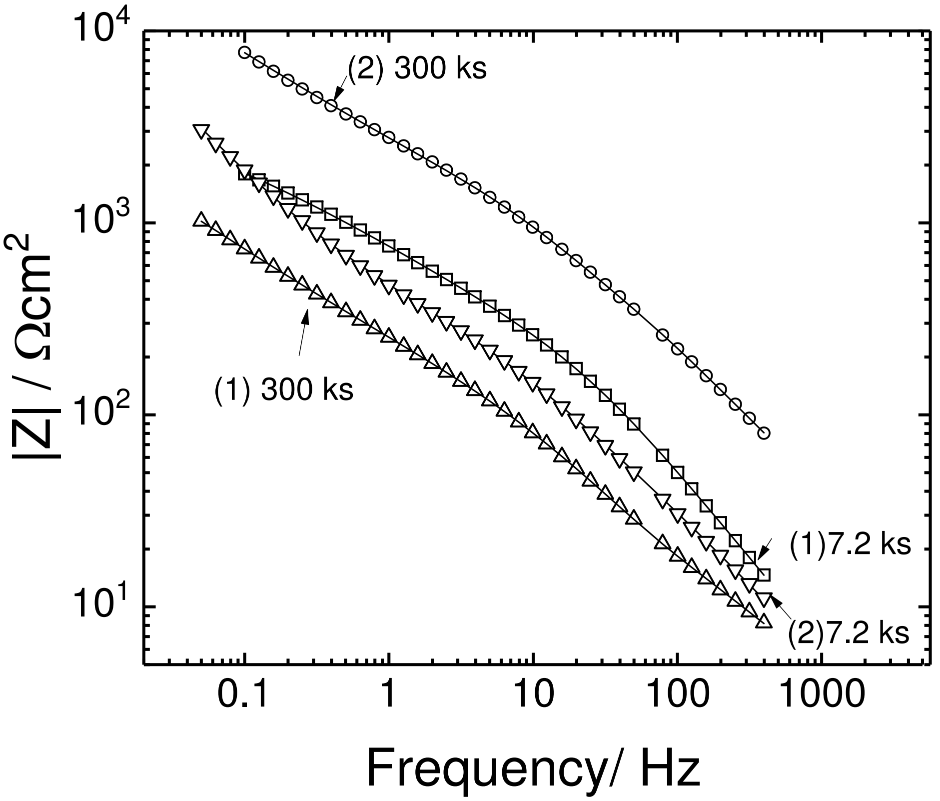

Figure 2.12: Ohmic-resistance-corrected magnitude of the impedance, obtained from equation (2.7), for the data presented in Figure 2.11. Labels (1) and (2) refer to steels No. 1 and 2, respectively. The lines represent the regression of equation (2.8) to data for steel No. 1 (at 7.2 ks and 300 ks) and steel No. 2 (at 7.2 ks) and equation (2.16) for steel No. 2 at 300 ks.

phase angle was defined following Alexander et al.[68] as

$$\varphi_{\mathrm{dZj}} = 90\frac{\mathrm{d}\log|Z_{\mathrm{j}}|}{\mathrm{d}\log f} \tag{2.6}$$

The low-frequency phase-angle information for steel No. 1 is consistent with the information obtained from the Nyquist plots in Figure 2.9 and 2.10. After a short exposure, the phase angle defined by equation (2.6) reached a plateau value of 33°. After a steady-state condition was obtained, the phase angle had a value of 44°.

The imaginary-impedance-derived phase angle obtained at 7.2 ks for steel No. 2 was less conclusive, but a low-frequency phase angle of 65° is evident after 300 ks, when a steady state was achieved. To emphasize the comparison between model and data at high frequency, the magnitude presented in Figure 2.12 was adjusted by subtracting the ohmic resistance, following Orazem et al.,[69] i.e.,

$$|Z| = \sqrt{(Z_{\mathrm{r}} - R_{\mathrm{e}})^2 + Z_{\mathrm{j}}^2} \tag{2.7}$$

The match between the model values and data shown in Figures 2.11 and 2.12 suggest that the process models discussed in the subsequent section provided an excellent fit to the data.

Process Model Development

Before steady-state was reached, both No. 1 and No. 2 ASTM A416 steels showed porous electrode behavior that could be fit by the process model proposed by Chen and Orazem,[5] i.e.,

$$Z = R_{\mathrm{e}} + \left(\frac{R_{\mathrm{t,a}} + Z_{\mathrm{c}}}{R_{\mathrm{t,a}}Z_{\mathrm{c}}} + (\mathrm{j}\omega)^{\alpha}Q\right)^{-1} \tag{2.8}$$

where Z_{c}, associated with oxygen reduction, has the general form expressed in terms of lumped parameters as

$$Z_{\mathrm{c}} = A_1\sqrt{Z_1}\coth\left(\frac{A_2}{\sqrt{Z_1}}\right) \tag{2.9}$$

where

$$Z_1 = \frac{(1 + A_3\left(\frac{\tanh\sqrt{\mathrm{j}\omega A_4}}{\sqrt{\mathrm{j}\omega A_4}}\right)}{1 + \mathrm{j}\omega A_5\left(1 + A_3\left(\frac{\tanh\sqrt{\mathrm{j}\omega A_4}}{\sqrt{\mathrm{j}\omega A_4}}\right)\right)} \tag{2.10}$$

represents the interfacial impedance on the wall of porous electrode,

$$A_1 = \left(\frac{R_0 R_{\mathrm{t,c}}}{2\pi n^2 r}\right)^{0.5} \tag{2.11}$$

$$A_2 = L\sqrt{\frac{2\pi r R_0}{R_{\mathrm{t,c}}}} \tag{2.12}$$

$$A_3 = \frac{R_0}{R_{\mathrm{t,c}}} \tag{2.13}$$

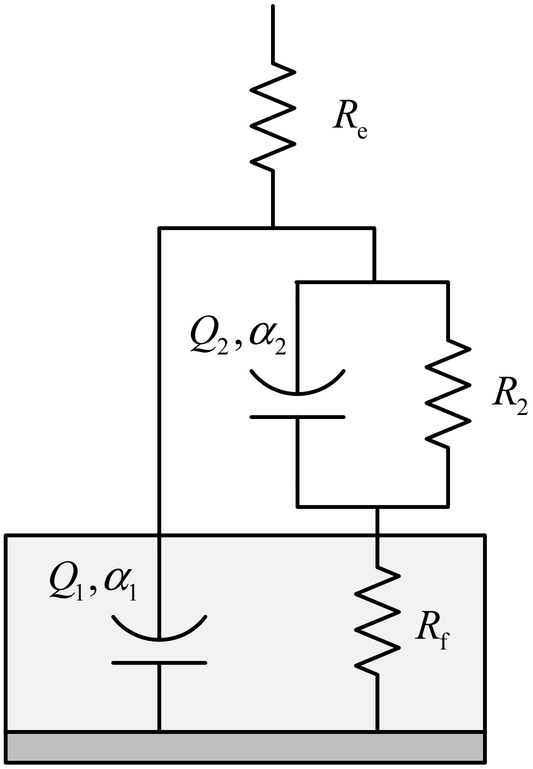

Figure 2.13: Electrical circuit representation of the model used for the No. 2 ASTM A416 steel under steady-state conditions. The CPE parameters Q_1 and α_1 represent the dielectric response of the oxide film, treated in the present work by the power-law model, and Q_2 and α_2 can be attributed to a surface distribution of time constants.

$$A_4 = \frac{\delta_r^2}{D_r} \tag{2.14}$$

and

$$A_5 = C_{\mathrm{c,dl}} R_{\mathrm{t,c}} \tag{2.15}$$

The parameters of interest for the present study are α and Q, from which oxide film thickness may be inferred, and $R_{\mathrm{t,a}}$, which gives information concerning the corrosion rate.

After steady state was reached, the No. 1 ASTM A416 steel still showed porous electrode behavior. Observation of porous electrode behavior may be attributed to the presence of FeOOH in the oxide film, in agreement with the cyclic voltammetry results shown in Figure 2.8. Schmuki et al.[51] suggested that reduction of the Fe(III) oxide takes place at potentials $V < -1$ V(SCE) and the entire film is converted to an Fe(II) oxide/hydroxide. The Fe(II) film must be porous to allow, in the following anodic cycle at $V > -0.9$ V(SCE), a new passive film to grow below the porous layer. As the potential reaches $V > 0.7$ V(SCE), the Fe(II) in the outer porous layer is oxidized to Fe(III).

As porous electrode behavior could not be observed after a steady state was reached for No. 2 ASTM A416 steel, the model shown in Figure 2.13 was used. The mathematical model for the total impedance in this case can be expressed as

$$Z = R_{\mathrm{e}} + \left(\left(R_{\mathrm{f}} + \frac{R_2}{1 + (\mathrm{j}\omega)^{\alpha_2} Q_2 R_2} \right)^{-1} + \left(\frac{1}{(\mathrm{j}\omega)^{\alpha_1} Q_1} \right)^{-1} \right)^{-1} \tag{2.16}$$

The circuit shown in Figure 2.13 was used by Joiret et al.[3] for a stationary iron electrode in 1M NaOH. As the corresponding HAADF-STEM images shown in Figure 2.3(c) and 2.3(d) suggest that the oxide film covers the entire ASTM A416 steel uniformly, the faradaic reaction is envisioned to take place on the surface of the oxide layer. Experiments reported in the literature indicated that water still exists in passive oxide films.[70,71] The physical interpretation of the equivalent circuit shown in Figure 2.13 can be expressed as an electrode coated with an inert dielectric layer. Within the dielectric layer, the resistance R_{f} is associated with a redox process in the passive layer between magnetite and iron(III) oxides.[55] The insulating part of the coating can be considered to be a constant-phase element, with parameters Q_1 and α_1, under the assumption that the film has a distribution of resistivity normal to the electrode surface. The term R_2 accounts for the faradaic reaction taking place on the surface of the dielectric layer. The parameters Q_2 and α_2 can be attributed to a surface distribution on the oxide film.

This type of impedance response can be observed when FeOOH is not present in the oxide film. The corresponding cyclic voltammetry results are labeled (2) in Figure 2.8. The corresponding oxide film composition includes FeO, $Fe(OH)_2$, and Fe_3O_4. However, FeO is thermodynamically unstable below 575 °C, tending to disproportionate to metal and Fe_3O_4.[72]

Discussion

The curve fitting results shown as lines in Figures 2.1, 2.2, and 2.9–2.12 suggest that the models provide accurate fits to the experimental data. The anodic charge-transfer resistance, $R_{\mathrm{t,a}}$, may be used to provide an estimate for the corrosion rate. The values for Q and α associated with the constant-phase element may be used to estimate oxide film thickness by use of the power-law model developed by Hirschorn et al.[1,2] The value of ρ_δ, required for application of the power-law model, was obtained by calibration.

Measurements at the Corrosion Potential

Parameters extracted from the fitting procedure for the data presented in Figures 2.9 and 2.10 for No. 1 and No. 2 steel are presented in Table 2.4. The anodic charge-transfer resistance, $R_{\mathrm{t,a}}$, could only be extracted from impedance data after an elapsed time of 7.2 ks (2 h) for No. 1 steel. The observation that a statistically-significant value for the anodic charge-transfer resistance could not be extracted from fitting procedure after steady state was reached (300ks) suggests that the steady-state corrosion rate was too small to be measured at the open-circuit potential. For No. 2 steel, porous electrode behavior was observed for an elapsed time of 7.2 ks, but a statistically significant value for the anodic charge-transfer resistance could not be obtained. The model represented by Figure 2.13 was used for data collected after an elapsed time of 300 ks. As a statistically significant value for R_2 could not be obtained, corrosion rates could also not be estimated for No. 2 steel at the corrosion potential.

Table 2.4: Values of the regressed parameters for No. 1 and No. 2 steel obtained from impedance data collected at the corrosion potential after elapsed times of 7.2 ks (2 h) and 300 ks (85 h). The regressed values for No. 1 steel were taken from Chen and Orazem,[5] but new values are reported for the calculated film thickness.

	Material	Steel #1		Steel #2	
Elapsed Time	ks	7.2	300	7.2	300
Equation (2.8)					
R_e	$\Omega\mathrm{cm}^2$	1.9±0.11	1.3±0.24	2.2±0.2	
$A_1 = (R_0 R_{\mathrm{t,c}}/2\pi n^2 r)^{0.5}$	$\mathrm{k}\Omega/\mathrm{cm}^{1/2}$	0.77±0.02	0.58±0.02	1.3±0.09	
$A_2 = L(2rR_0/R_{\mathrm{t,c}})^{0.5}$	–	1.4±0.03	0.83±0.05	1.4±0.1	
$A_3 = R_\mathrm{D}/R_{\mathrm{t,c}}$	–	16.2±1.1	31.3±2.03	6.7±0.2	
$A_4 = \delta_r^2/D_r$	s	–	60.4±3.3	–	
$A_5 = C_{\mathrm{dl,c}} R_{\mathrm{t,c}}$	ms	1.2±0.05	7.7±0.44	7.3±0.7	
Q	$\mu\mathrm{F/s}^{(1-\alpha)}\mathrm{cm}^2$	16.9±0.04	410±3	65±12	
$R_{\mathrm{t,a}}$	$\mathrm{k}\Omega\mathrm{cm}^2$	4.7±0.02	–	–	
α	–	0.96±0.01	0.70±0.01	0.87±0.02	
Equation (2.16)					
R_e	$\Omega\mathrm{cm}^2$				2.1±0.1
Q_1	$\mu\mathrm{F/s}^{(1-\alpha)}\mathrm{cm}^2$				46±1.9
α_1	–				0.91±0.01
R_1	$\mathrm{k}\Omega\mathrm{cm}^2$				0.12±0.01
Q_2	$\mu\mathrm{F/s}^{(1-\alpha)}\mathrm{cm}^2$				420±2.9
α_2	–				0.63±0.03
R_2	$\mathrm{k}\Omega\mathrm{cm}^2$				–
$\ln(\delta/\mathrm{nm})$		0.69±0.17	1.46±0.48	0.75±0.41	0.47±0.22
$\overline{\delta}$	nm	2	4.3	2.1	1.6

The film thicknesses reported in Table 2.4 for No. 1 and No. 2 steel followed a log normal distribution. Thus, the confidence intervals are reported for $\ln(\delta)$ with δ in units of nm. When the standard deviation for $\ln(\delta)$ was smaller than 0.2, the distribution approximated a normal distribution, as was reported by Orazem et al.[46] Thus, a linear propagation of error analysis could provide a valid confidence interval for δ for the measurement at an elapsed time of 7.2 ks, but the Monte Carlo analysis was required for the measurement at an elapsed time of 300 ks. The film thickness values reported as $\overline{\delta}$ correspond to values calculated directly from equation (2.2). These values were in good agreement with the value calculated from the mean of $\ln(\delta)$. The film thickness for No. 1 steel differs from that reported in an earlier publication[5] due to the change in the assumed values for dielectric constant and ρ_δ. Nevertheless, the film thickness was still larger after steady state was reached.

Influence of Applied Potential

Parameters extracted from the fitting procedure for steady-state impedance scans measured at different applied potentials for No. 1 steel are presented in Table 2.5. An anodic charge-transfer resistance could be extracted only for No. 1 steel polarized at +0.22 V(Hg/HgO). The film thickness was found to be larger for potentials anodic to the open-circuit potential and smaller for cathodic potentials. The decrease of oxide film thickness at more negative potentials is in agreement with use of cathodic pre-treatment to remove air-formed oxide films.

Parameters extracted from the fitting procedure at different applied potentials for No. 2 steel are presented in Table 2.6. The oxide film thickness was found to increase with potential, but was smaller than for the No. 1 steel. A value for R_2 could not be extracted for any of the tested potentials. This behavior suggests that No. 2 steel has better corrosion resistance at positive applied potentials.

The nature of the film-thickness distributions obtained by Monte Carlo simulations is demonstrated in Figure 2.14 for No. 2 steel at a potential of -0.38 V(Hg/HgO), shown in Table 2.6. The log normal distribution for δ is shown in Figure 2.14(a), where the solid line represents a log normal distribution. The corresponding distribution for $\ln(\delta)$ is given in Figure 2.14(b), where the solid line represents a normal distribution. As shown in Table 2.6, $\overline{\delta} = 1$ nm and the distribution is given as $(\ln \delta/\mathrm{nm}) = 0.005 \pm 0.5$.

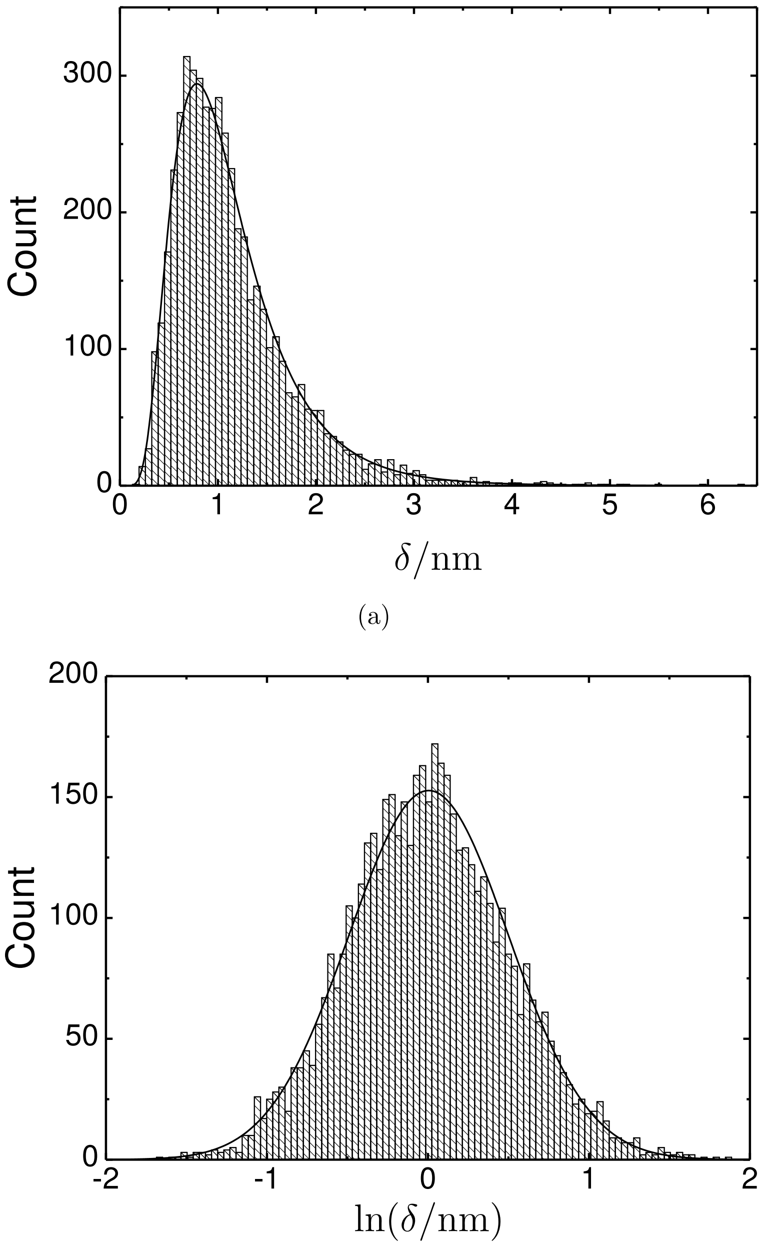

(a)

(b)

Figure 2.14: Distributions for film thickness estimated by Monte Carlo simulations for No. 2 steel at a potential of -0.38 V(Hg/HgO), shown in Table 2.6: (a) δ, where the solid line represents a log normal distribution, and (b) $\ln(\delta)$, where the solid line represents a normal distribution.

Table 2.5: Values of the regressed parameters obtained for impedance data measured for No. 1 ASTM A416 at different applied potentials after a steady-state current was reached.

	Potential V(OCP)	-0.3	- 0.2	-0.1	+0.1	+0.2	+0.3
R_e	$\Omega\mathrm{cm}^2$	1.1±0.05	0.90±0.13	1.3±0.24	0.69±0.23	1.20±0.21	0.51±0.22
$A_1 = \sqrt{\frac{R_0 R_\mathrm{t,c}}{2\pi n^2 r}}$	$\mathrm{k}\Omega/\mathrm{cm}^{0.5}$	0.59±0.11	0.67±0.01	0.58±0.02	0.34±0.06	0.29±0.03	0.26±0.07
$A_2 = L\sqrt{\frac{2rR_0}{R_\mathrm{t,c}}}$	dimensionless	0.73±0.03	0.77±0.04	0.83±0.05	0.95±0.12	1.07±0.05	0.99±0.12
$A_3 = R_\mathrm{D}/R_\mathrm{t,c}$	dimensionless	19±6.3	17±0.44	31±2.0	36±11	83±11	15±3.7
$A_4 = \delta_r^2/D_r$	s	203±13	82± 3.4	60±3.3	24±2.4	63± 16	–
$A_5 = C_\mathrm{dl,c} R_\mathrm{t,c}$	ms	5.8±0.25	7.3±0.46	7.7±0.44	3.4±0.42	2.6±0.15	1.7±0.36
Q	$\mathrm{mF/s^{(1-\alpha)}cm^2}$	0.77±0.01	0.66± 0.01	0.41±0.03	0.44±0.16	0.28± 0.05	0.32±0.10
$R_\mathrm{t,a}$	$\mathrm{k}\Omega\mathrm{cm}^2$	–	–	–	–	–	5.90±0.52
α	dimensionless	0.67±0.03	0.66±0.01	0.70±0.01	0.70±0.05	0.72±0.03	0.69±0.05
$\ln(\delta/\mathrm{nm})$		1.26±0.67	1.58±0.53	1.46±0.49	1.47±1.00	1.58±0.63	1.93±0.97
$\overline{\delta}$	nm	3.5	4.8	4.3	4.0	4.6	6.3

Table 2.6: Values of the regressed parameters obtained for impedance data measured for No. 2 ASTM A416 measured at different applied potentials after a steady-state current was reached.

	Potential V(Hg/HgO)	-0.38	-0.28	0.02	0.12	0.22
R_e	$\Omega\mathrm{cm}^2$	1.6±0.01	1.5±0.01	2.1±0.02	2.2±0.01	2.4±0.01
Q_1	$\mu\mathrm{F/s}^{(1-\alpha)}\mathrm{cm}^2$	99±2.7	100±3.1	39±0.7	36±1.5	30±1.0
α_1	dimensionless	0.89±0.003	0.88±0.005	0.92±0.01	0.92±0.003	0.92±0.003
R_1	$\Omega\mathrm{cm}^2$	30±1.3	60±3.3	96±1.6	83±1.3	52±1.6
Q_2	$\mathrm{mF/s}^{(1-\alpha)}\mathrm{cm}^2$	0.9±0.01	0.6±0.02	0.39±0.02	0.36±0.05	0.29±0.07
α_2	dimensionless	0.52±0.001	0.57±0.003	0.61±0.002	0.62±0.001	0.62±0.004
R_2	$\mathrm{k}\Omega\mathrm{cm}^2$	–	–	–	–	–
$\ln(\delta/\mathrm{nm})$		0.005±0.5	0.16±0.20	0.47±0.20	0.55±0.14	0.74±0.14
$\overline{\delta}$	nm	1.0	1.2	1.6	1.7	2.1

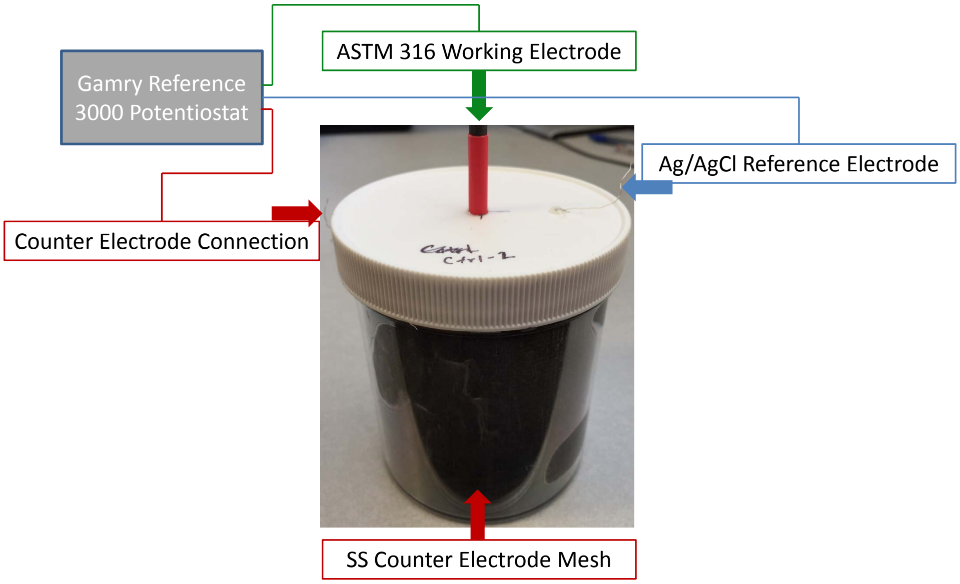

Figure 2.15: Schematic showing the conventional three-electrode impedance measurement on a cylindrical electrochemical cell in which the electrolyte is grout and the working electrode is a coupon of the steel strand.

2.2 Disk Electrodes in Grout

Conventional impedance experiments were conducted with a disk electrode embedded in grout to determine the impedance behavior of the steel within the environment of the grout. The impedance was analyzed with mathematical models which include physical parameters to describe the behavior of the steel and grout interface.

2.2.1 Experimental

One of the necessary parameters needed to develop a reliable interpretation technique of the indirect impedance is the impedance of the steel and grout interface in locations of passive and actively corroding steel. Cells configured with 3 electrodes were made of small plastic cylinders containing grout as the electrolyte and the impedance was measured across the steel and grout interface. A 3-in rod of steel was cut from the king wire of the steel strand and was inserted into the grout as shown in Figure 2.15. Heat shrink tubing and duct-tape was used to insulate the sides of the steel rod such that only the cross section of the rod was exposed to the grout in the form of a disk electrode within an insulating plane. A stainless-steel wire mesh was used as the counter electrode and a solid Ag/AgCl electrode was used as the reference.

Four cells were made and two of them were forced to corrode. A schematic of the impressed current technique is presented in Figure 2.16. A constant 20-V potential was applied between the steel rod and the stainless steel mesh for 1 week. The impedance was measured before and after the application of the impressed current.

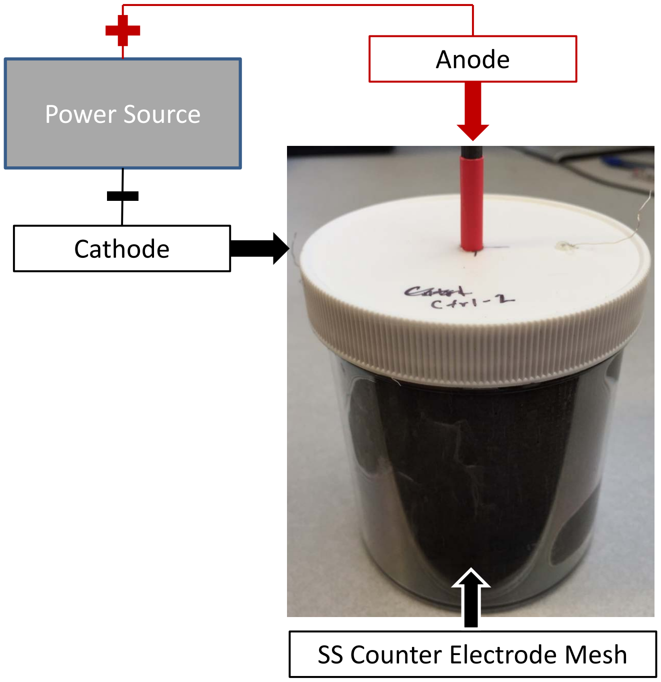

Figure 2.16: Schematic showing the impressed current technique for a cylindrical electrochemical cell in which the electrolyte is grout and the working electrode is a coupon of the steel strand.

2.2.2 Results

The impedance results of two of the specimens are presented in Figure 2.17, in which one is labeled as the control and the other is the to-be-corroded specimen. The results should be representative of the impedance of the steel and grout interface. The impedance was measured at frequencies between 500 Hz and 10 mHz. At high frequencies there is a depressed capacitive arc followed by a straight line at an angle at lower frequencies. The-high frequency behavior in both cases is almost identical while the slope of the impedance is slightly larger for the control specimen.

The impedance of a corroding specimen is compared to the control case in Figure 2.18. After forcing one of the specimens to corrode, the impedance decreased drastically. The ohmic resistance of the corroded specimen increased which can be explained by the reduction of water that occurs due to the cathodic reaction which increases the resistivity. The impedance of the control specimen did not change significantly. The figure inset shows a magnified view of the corroded specimen impedance which contains a high frequency tail and a small capacitive arc at lower frequencies. The magnitude of the impedance decreased by a factor of 50 after forcing corrosion.

The steel rods from the control and corroded specimens were removed to view the steel surface. Images of the steel surface are presented in Figure 2.19. The control case, Figure 2.19(a), has a shiny surface and areas of residual grout which have adhered to the surface. The corroded case shown in Figure 2.19(b) has reddish-brown corrosion product similar to what was observed on the steel removed from the tendons after the induced corrosion. In this case the corrosion is much more uniform and advanced.

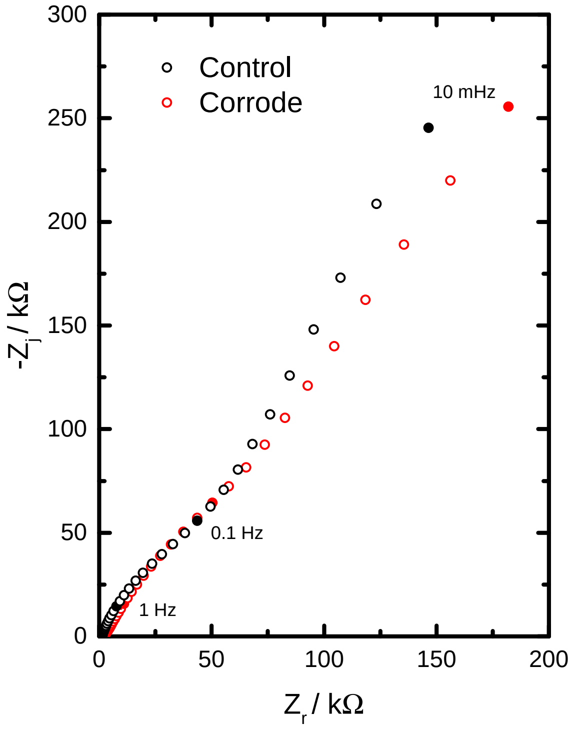

Figure 2.17: Conventional three-electrode impedance of a steel disk electrode in grout before one of the specimens (corroded) was forced to corrode.

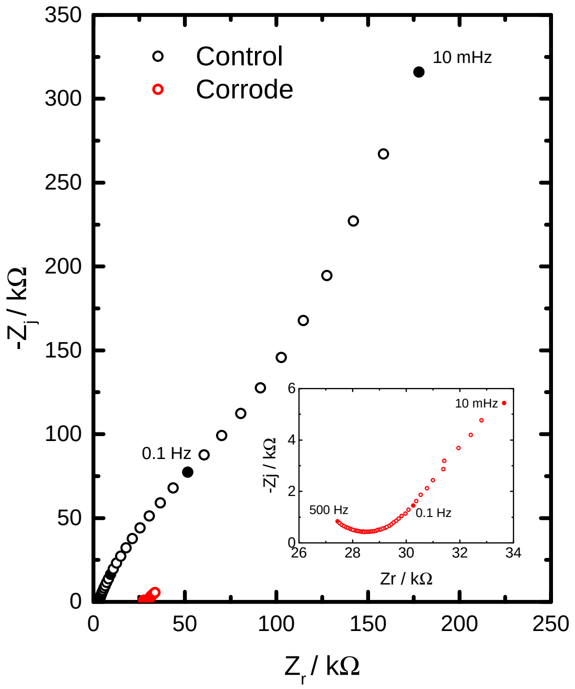

Figure 2.18: Conventional three-electrode impedance of a steel disk electrode in grout after one of the specimens (corroded) was forced to corrode.

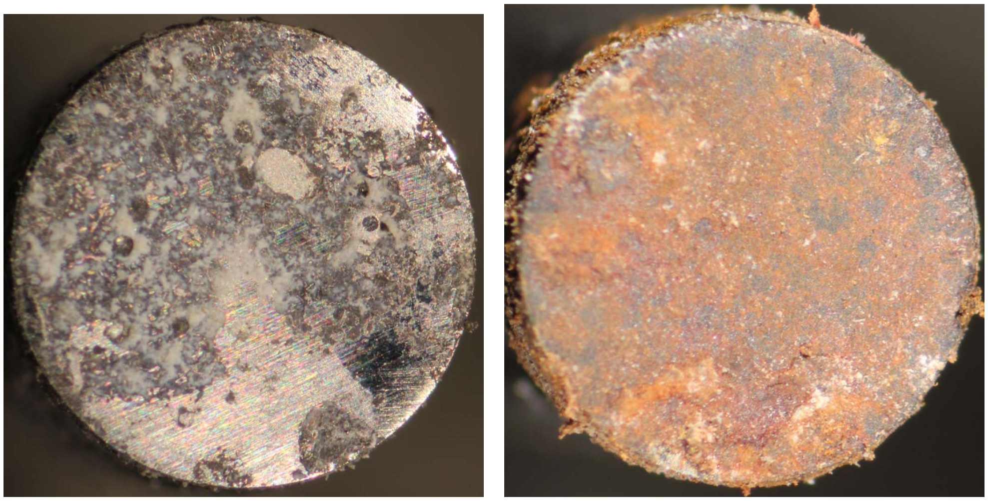

(a) (b)

Figure 2.19: Images of the steel disk electrode extracted from the grout: (a) passive case and (b) corroded case.

2.2.3 Regression Analysis

An equivalent circuit model was developed to fit the impedance results of the 3-electrode measurements to build an understanding of the impedance of the steel and grout interface. The equivalent circuit is based upon a physical model of the interface which is presented in Figure 2.20. We have assumed the interface comprises a porous film due to an uneven oxide layer. The resistance to current flow through the pore is described by R_{sp}, and the impedance of the interface between the solution and the bare metal is described as a resistor and constant-phase element in parallel with parameters R_{t}, Q_2, and α_2. The impedance of the film was modeled as a constant-phase element with parameters Q_1 and α_1 under the assumption that the film has a distribution of resistivity normal to the electrode surface.

The fitting results are presented in Figure 2.21 in Nyquist format for the control case. OriginLab nonlinear complex regression analysis with modulus weighting was used to fit the parameters to the data. The fitting results are presented in Table 2.7 along with the standard error for each parameter. Theoretically, R_{t} should be very large for the passive case and should decrease as the corrosion rate increases. The same circuit model was applied to the corroded case but the results were not realistic. Therefore, a measurement model[73] was used to determine the extrapolated value of the zero frequency limit of the real impedance which signifies the lowest possible value of the polarization resistance. A series of Voigt elements are fit to the impedance sequentially until the fit cannot be improved with the addition of another element. The extrapolated value of the low-frequency limit of the impedance is then based on the element which has the largest time constant. The value obtained was approximately 15 kΩ which is roughly 30 times less than the charge-transfer resistance obtained for the passive case.

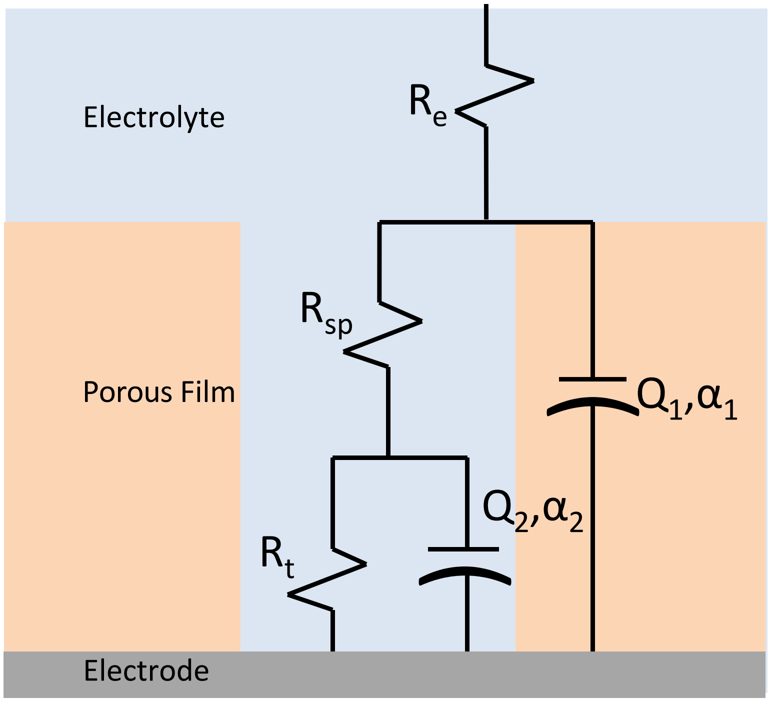

Figure 2.20: Circuit diagram for the passive steel and grout interface.

Table 2.7: Regression parameters and standard error for equivalent circuit fit to conventional three-electrode impedance for the passive case.

Variable	Regression Estimate	Units
R_e	206 ± 9.0	Ω cm^2
R_sp	31.57 ± 0.86	kΩ cm^2
R_t	532 ± 26	kΩ cm^2
Q_1	334 ± 4	μF/s$^{(1-\alpha)}$cm^2
α_1	0.86 ± 0.01	
Q_2	213 ± 1	μF/s$^{(1-\alpha)}$cm^2
α_2	0.79 ± 0.01	

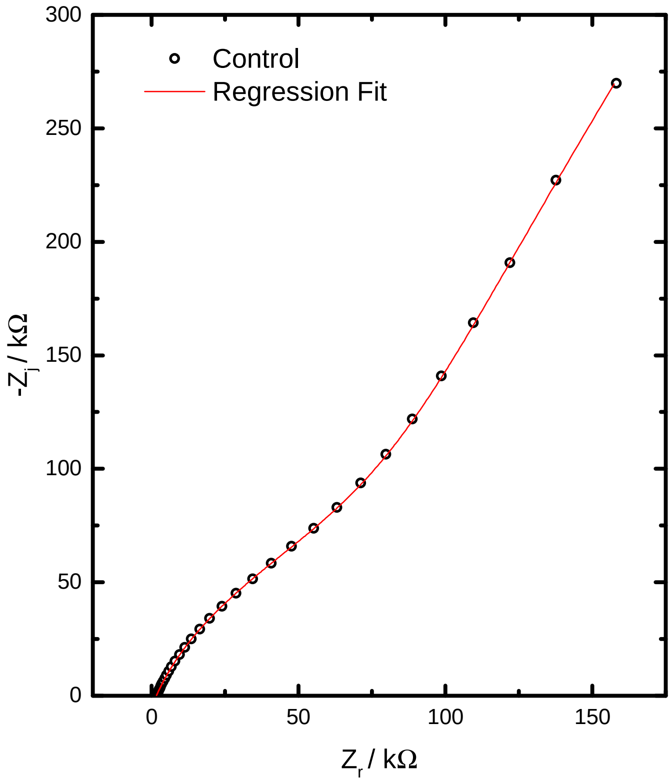

Figure 2.21: Impedance of the passive steel disk electrode in grout fitted with the circuit in Figure 2.20.

Chapter 3

Application to Bridge Tendons

The indirect impedance technique was tested on sections of tendons taken from the Ringling Causeway Bridge and on external tendons on a mock bridge constructed at the Texas A&M University under a contract from the National Cooperative Highway Research Program.[6]

3.1 Ringling Causeway Bridge

Samples of a failed external post-tensioned tendon from the Ringling Causeway Bridge were obtained from the FDOT State Materials Office. These tendons differed from the synthetic tendons fabricated and described in a previous report[57] in that the synthetic tendons had a single steel strand; whereas the Ringling Causeway had many more tendons.

3.1.1 Methods

The external post-tensioned tendons on the Ringling Causeway Bridge showed signs of corrosion fewer than 7 years after construction. The tendons that were replaced were cut into 3 or 4 ft. sections and stored at the FDOT State Materials Office. Indirect impedance measurements were performed on one of the sections that showed corrosion. An image of the cross-section is shown in Figure 3.1. The tendon contained 22 strands of steel which are randomly dispersed. There were visible signs of grout segregation and corrosion of one of the steel strands. Measurements were performed at 6 different locations around the tendon to determine if corrosion could be detected.

3.1.2 Results

The indirect impedance results from the Ringling Bridge tendon are shown in Figure 3.2. The numbers correspond to the location of the measurement shown in Figure 3.1. Measurements could not be made at location 2 because the steel strand was exposed from the grout when the holes were drilled. The smallest impedance was found for the location of the corroded strand, shown as number 4 in Figure 2. A smaller impedance is expected for corroding steel as the impedance associated with corrosion of steel is smaller than the impedance associated with passivated steel.

The impedance at location 4 is shown separately in Figure 3.3. There are two capacitive

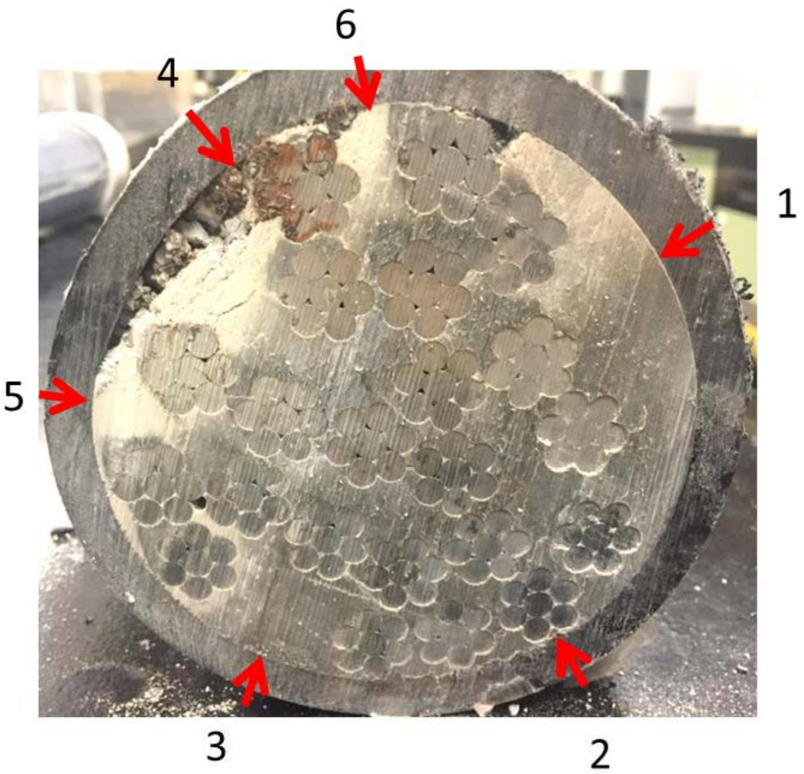

Figure 3.1: The cross-section of the Ringling Bridge tendon. The numbers indicate the locations of the electrodes.

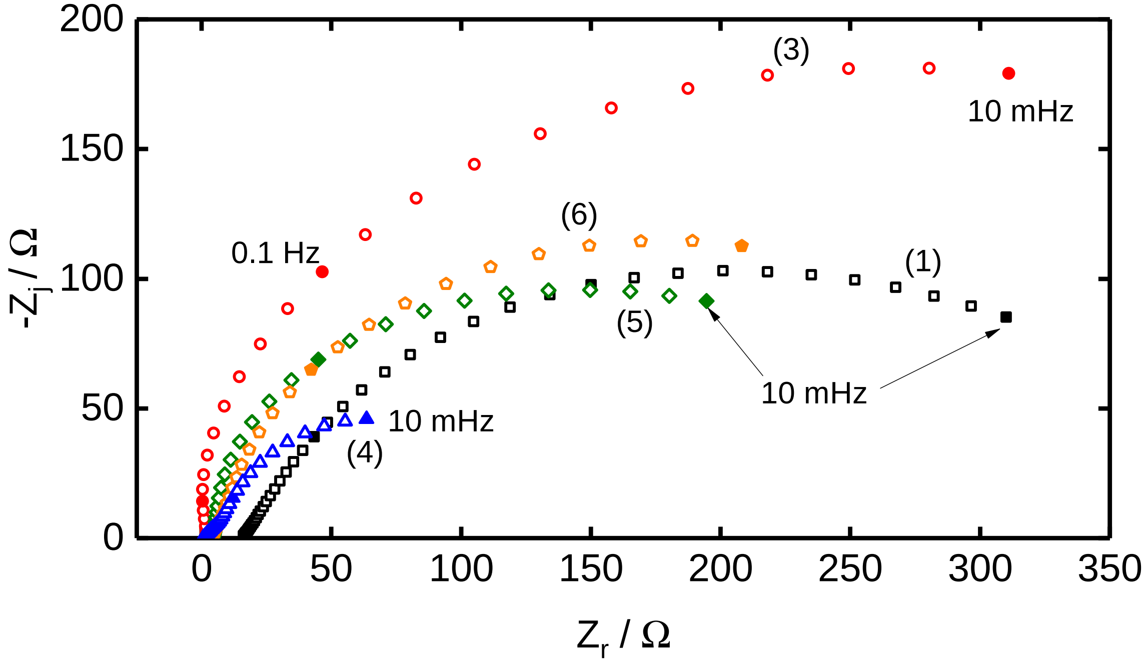

Figure 3.2: Experimental impedance in Nyquist format measured on an extracted tendon from the Ringling Causeway Bridge with the location of the electrodes as a parameter. The numbers in parentheses correspond to the location of the tendon shown in Figure 3.1.

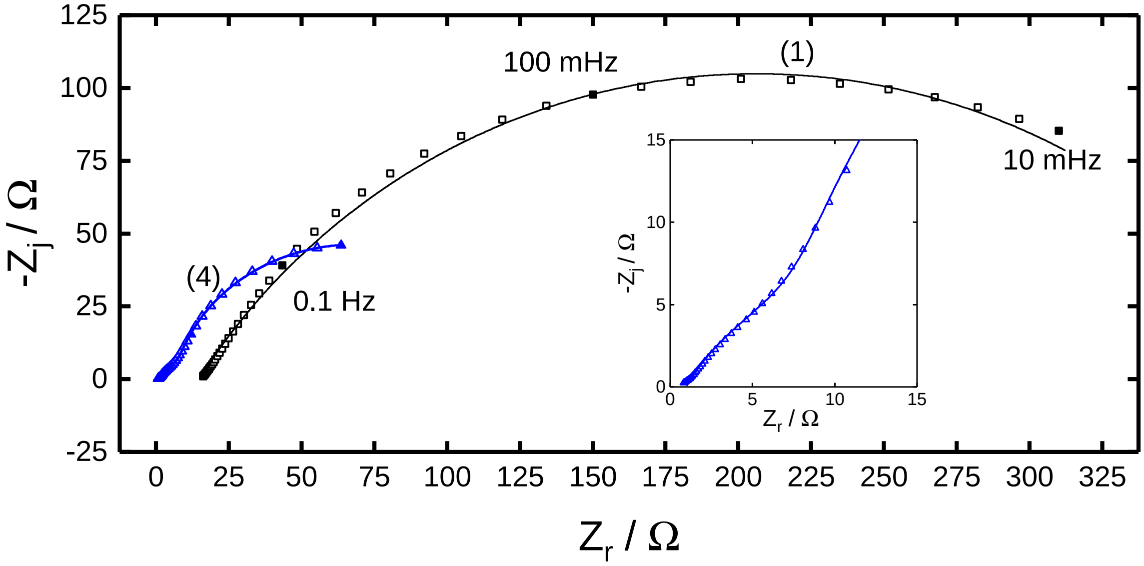

Figure 3.3: Experimental impedance in Nyquist format measured on an extracted tendon from the Ringling Causeway Bridge. The numbers in parentheses correspond to the location of the tendon shown in Figure 3.1. The inset shows the high-frequency behavior measured at location (4).

loops which overlap, indicating the presence of two time constants. The higher-frequency time constant is associated with the corrosion reaction. The results indicate that corrosion can be detected if it is located directly beneath the array of electrodes. However, if the corrosion is located on a steel strand not near the measurement electrodes, it may be undetected.

An experiment was set up to try to overcome this obstacle. Instead of the electrodes being placed along the axis of the tendon, the electrodes were placed circumferentially in hopes that this electrode configuration was more sensitive to corrosion. The impedance results are shown in Figure 3.4 with the number designation indicating the location of the 4 electrodes corresponding to the diagram in Figure 3.1. The results are similar to the results in Figure 3.2 in that there is only one particular measurement, when the electrodes were at locations 5-4-6-1, that was able to detect the corrosion shown by the significantly smaller impedance. Therefore, the corrosion detection capabilities of the indirect impedance measurement are confined to cases where the corrosion is present directly beneath the measurement electrodes.

3.2 Texas A&M Mock Bridge

A full-scale post-tensioned girder specimen and four large-scale stay cable specimens were constructed at the Texas A&M University Riverside Campus to provide a platform for evaluation of NDE technologies. The final report for this project is given as reference [6]. On two separate occasions in 2016 (January 27–29 and March 9–11) members of our team visited the Texas A&M facility to apply the indirect impedance technique.

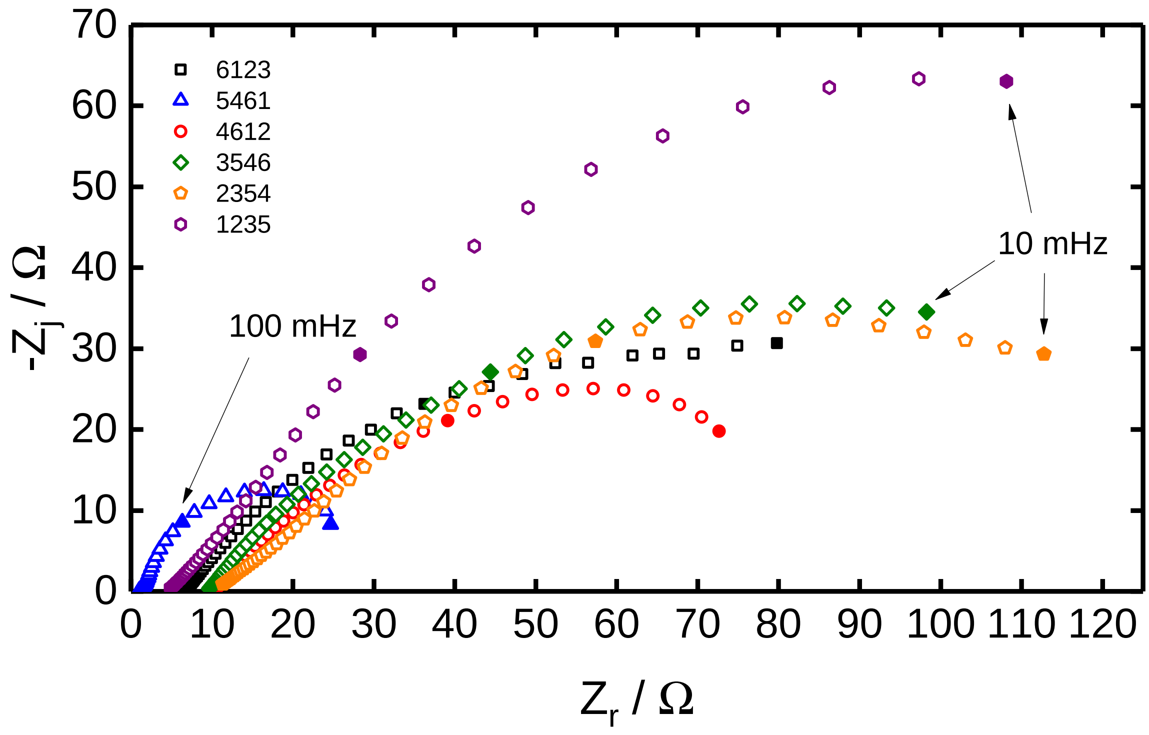

Figure 3.4: Experimental impedance in Nyquist format measured on an extracted tendon from the Ringling Causeway Bridge with the location of the electrodes as a parameter. The numbers in designation corresponds to the electrode locations described in Figure 3.1.

Figure 3.5: An image of the interior of the mock bridge built at Texas A&M University. Photograph by Mark Orazem.

3.2.1 Methods

The external tendons on the Texas A&M mock bridge, shown in Figure 3.5, were constructed with different types of defects. Corrosion defects were fabricated by grinding the wires and strands to the desired cross-sectional area.[6] To simulate cases where all seven wires of the strands are fully lost, the cross-sectional areas of the strands were gradually reduced over a 2-ft length and then cut through to represent an entire loss in strand cross-sectional area. Corrosion was then induced on the steel by submerging parts of the steel strands in an HCl bath solution prior to constructing the tendons. After construction, the tendons and the bridge itself were discretized into 1 ft. sections and labeled alphabetically. Each tendon location specification included the tendon number as well as the section designation (i.e., 13JK). Indirect impedance measurements were performed at locations in which all the steel strands were severed with corroded ends, the steel strands were partially corroded, or all the strands were not corroded.

The experimental setup is shown in Figure 3.6 with the leads of the potentiostat connected to the electrodes. Four small holes were drilled into the HDPE duct to provide access to the grout. Dimensionally stable 0.5 cm diameter titanium rods coated in iridium-oxide were inserted into the holes and used as the electrodes. An in-house conductive gel consisting of a 1M sodium sulphate solution and carboxyl-methyl cellulose as a polymeric gelling agent

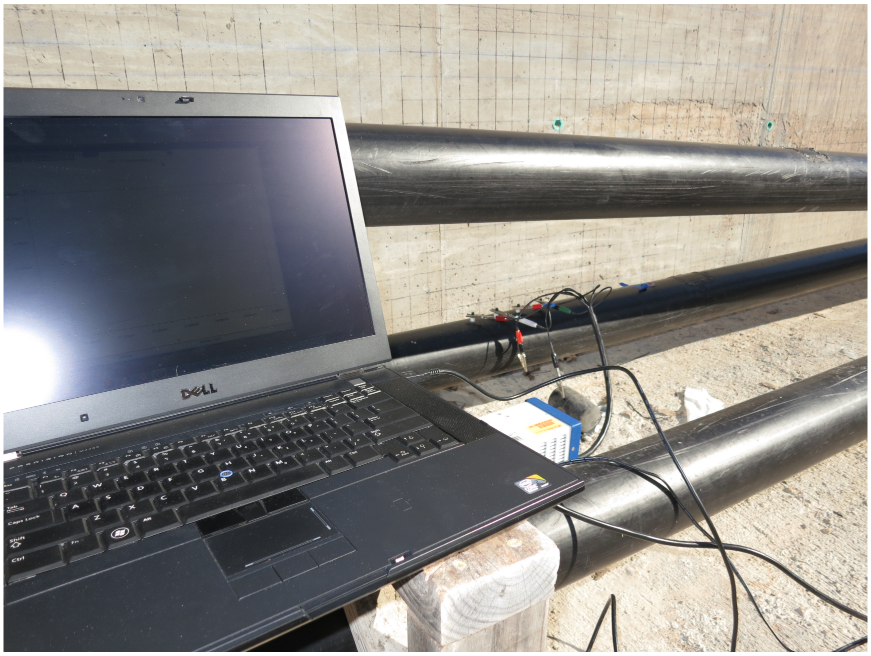

Figure 3.6: Experimental setup of the indirect impedance measurement. Photograph taken at the Texas A&M mock bridge by Mark Orazem. The Gamry Reference 600 potentiostat is the white/blue box in the center of the photograph.

was used to make an electrical connection between the electrode and the grout. Impedance measurements can be taken by either modulating potential, referred to as potentiostatic modulation, or current, referred to as galvanostatic modulation. Potentiostatic modulation was found to be more reproducible and less noisy than galvanostatic modulation measurements. The impedance was measured with a Gamry reference 600 potentiostat over a range of frequencies. Real-time Lissajous plots are displayed on the computer screen while measuring each frequency. After the measurements were performed, the holes were sealed by using a HDPE welding technique.

3.2.2 Results

Results from the Texas A&M mock bridge are presented in Figure 3.7 for different locations as marked on the bridge. The indirect impedance is a function of the grout resistivity, the steel-grout interfacial impedance, and the location of the steel strands. Measurements were taken at the top of the tendon, unless the designation ends in 2, in which they were taken along the side. Corrosion associated with segregation of grout is most likely to occur near the top of the tendon since the grout near the top will have a higher conductivity. If there is a steel strand located near the electrodes, the real impedance will be negative at high frequencies due to the potential distribution, as is the case for location 16CD. The high-frequency limit of the real impedance represents the ohmic resistance which can be associated with the resistance of current flow between the grout and the steel. The ohmic resistance is also a good measure of the depth of the steel. The significantly larger ohmic resistance measured at section 16VW may be attributed to properties of the grout, such as

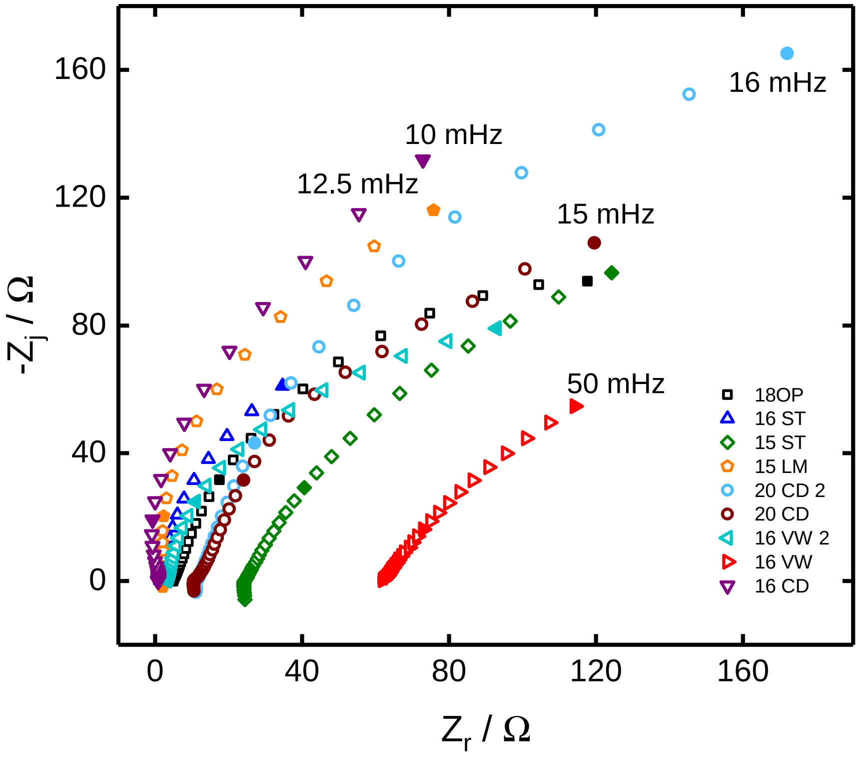

Figure 3.7: Experimental impedance in Nyquist format measured at different sections of the Texas A&M bridge tendons.

voids.

Sections 16VW and 16ST had the smallest impedance values. The smaller impedance values suggest that corrosion was present. The indirect impedance for section 16VW is shown separately in Figure 3.8. The measurement was fit with a simple circuit with a series and a parallel resistor accounting for the ohmic contribution and the steel impedance was expressed as a $R_\mathrm{p}C_0$ circuit where R_p is the polarization resistance of the steel which is inversely related to the corrosion rate. Based on the circuit fitting, $R_\mathrm{p} = 292.9\ \Omega$. The figure inset shows the high-frequency behavior. The results show a very small high-frequency capacitive loop which overlaps the lower frequency data and may be a sign of corrosion. The indirect impedance for section 16ST is shown separately in Figure 3.9. The high-frequency behavior for section 16ST shows an inductive feature and significant high-frequency noise which has not been observed in our bench-top work or numerical simulations. The circuit did not fit the impedance well, but R_p was estimated to be 316.5 Ω.

Table 3.1: Results of measurements performed at the Texas A&M mock bridge facility. Locations, categories, and defect descriptions taken from Hurlebaus et al.[6]

Location	Category	Description of Condition	Impedance observations
18OP	INT	No defects	
16ST	CS1	1-2 of 7 wires fully corroded[a]	high-frequency inductive feature, small low-frequency impedance
15ST	INT	No defects	
15LM	CS1	1-2 of 7 wires fully corroded[a]	
20CD	INT	No defects	
16VW	INT	No defects	large ohmic resistance, small low-frequency impedance
16CD	LS1	1-2 of 7 wires fully lost	
17TU	CT2	3-4 of 19 strands or 2-3 of 12 strands fully corroded[b]	Unable to obtain measurement
16NO	CT1	1-2 of 19 strands or 1-2 of 12 strands fully corroded[b]	Unable to obtain measurement
17NO	CT4	19 of 19 strands or 12 of 12 strands fractured[c]	Unable to obtain measurement
16HG	BT4	19 of 19 strands or 12 of 12 strands fractured[c]	Unable to obtain measurement
16TU	CT2	3-4 of 19 strands or 2-3 of 12 strands fully corroded[d]	Unable to obtain measurement

[a] 14-29% Strand Cross-Section, <3% Tendon Cross-Section

[b] 16-25% Tendon Cross-Section

[c] 100% Tendon Cross-Section

[d] 16-25% Tendon Cross-Section

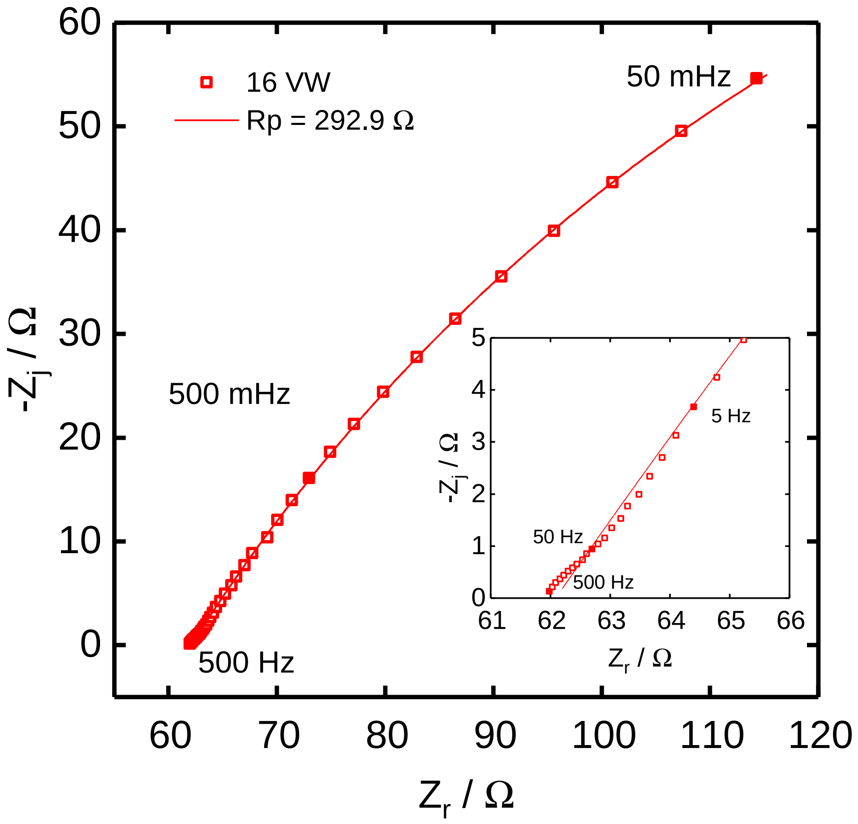

Figure 3.8: Experimental impedance in Nyquist format measured at location 16VW of the Texas A&M mock bridge tendons.

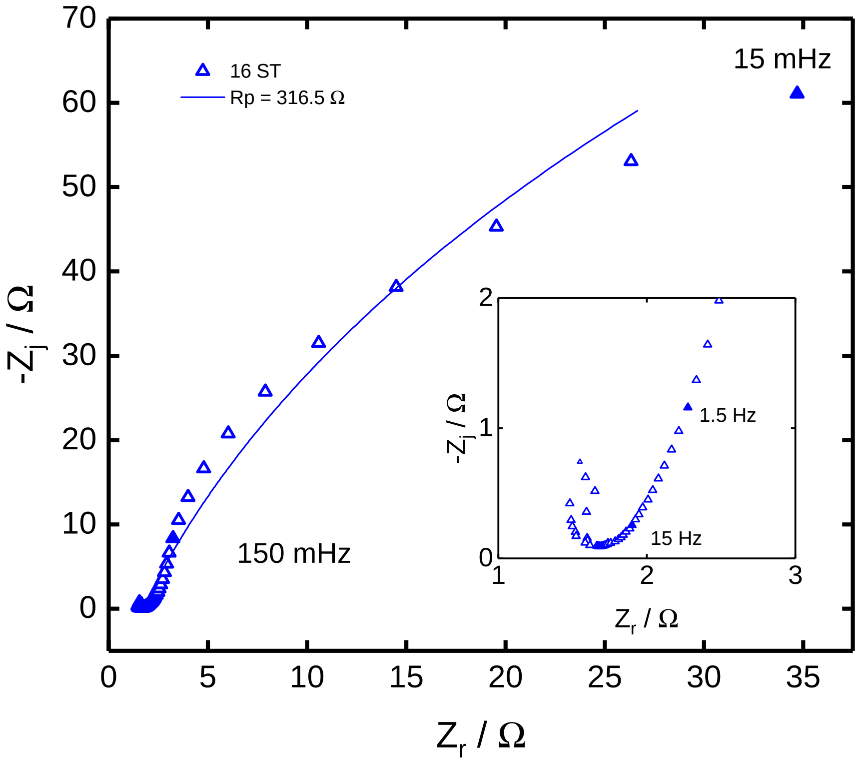

Figure 3.9: Experimental impedance in Nyquist format measured at location 16ST of the Texas A&M mock bridge tendons.

Chapter 4

Finite-Element Simulations

Finite-element simulations of the indirect impedance measurement were performed to assess the contribution of the grout resistivity to impedance as well as to determine the location of the steel that a particular electrode configuration senses. The indirect impedance was found to include two separate contributions of the grout resistivity. There is an ohmic impedance associated with the grout that is parallel to the steel and another ohmic impedance associated with the grout that is in series to the steel. The parallel component was much larger than the series component, and the impedance decreased with decreased frequency, whereas, the series component increased with decreased frequency. By understanding the exact influence the grout has on the indirect impedance, a method may be devised to extract the properties of the steel and determine the corrosion rate.

4.1 Mathematical Development

To aid in the interpretation of the experimental results, a finite-element model was developed to simulate the indirect impedance. Huang et al.[59] explained the use of linear kinetics as the boundary condition on a disk electrode based on the derivations of Newman[74] and Nisancioglu.[75,76] The normal current density at the surface of the electrode can be expressed in terms of a faradaic reaction and a charging current as

$$i = C\frac{\partial(V-\Phi)}{\partial t} + \frac{(\alpha_\mathrm{a}+\alpha_\mathrm{c})i_0\mathrm{F}}{\mathrm{R}T}(V-\Phi) = -\kappa\frac{\partial\Phi}{\partial y} \tag{4.1}$$

The oscillating current density may be expressed in the frequency domain as

$$\tilde{i} = \mathrm{j}\omega C(\tilde{V}-\tilde{\Phi}) + \frac{(\alpha_\mathrm{a}+\alpha_\mathrm{c})i_0\mathrm{F}}{\mathrm{R}T}(\tilde{V}-\tilde{\Phi}) \tag{4.2}$$

with the use of the relationship

$$i = \bar{i} + \mathrm{Re}\left\{\tilde{i}e^{\mathrm{j}\omega t}\right\} \tag{4.3}$$

where the current is expressed as the addition of a steady-state and an oscillating term. In Equation (4.2), $\tilde{V}$ is the potential perturbation, and $\tilde{\Phi}$ is the complex oscillating potential within the electrolyte. For the indirect impedance simulation, both the working and counter electrode boundary conditions were set as oscillating currents with a positive potential perturbation applied to the working electrode and a negative one applied to the counter electrode. A similar boundary condition was set at the steel but with the potential set to zero such that all other potentials would be in reference to the steel. The steel was modeled for an active corrosion case and a passive blocking electrode case. The active case is expressed as the addition of the charging and faradaic current, i.e.,

$$\tilde{i} = \mathrm{j}\omega C(-\tilde{\Phi}) + \frac{(\alpha_\mathrm{a} + \alpha_\mathrm{c})i_0\mathrm{F}}{\mathrm{R}T}(-\tilde{\Phi}) \tag{4.4}$$

The oscillating potential is found by solving Laplace's equation with the given frequency-dependent boundary conditions. With the use of potential probes, the impedance is simulated as the quotient of the potential difference between two reference probes and the current perturbation applied between the current-injecting electrodes expressed as

$$Z = \frac{\tilde{V}_\mathrm{ref1} - \tilde{V}_\mathrm{ref2}}{\tilde{I}} \tag{4.5}$$

The charge-transfer resistance for linear kinetics can be expressed in terms of the exchange current density as

$$R_\mathrm{t} = \frac{\mathrm{R}T}{i_0\left(\alpha_\mathrm{a} + \alpha_\mathrm{c}\right)} \tag{4.6}$$

which is the same expression used to estimate the polarization resistance of the steel in the corroding case. The 3D potential distribution was determined under the assumption of uniform electrolyte conductivity, and the indirect impedance was simulated.

The active case is expressed as the sum of the charging and faradaic current as

$$\tilde{i} = \mathrm{j}\omega C(-\tilde{\Phi}) + \frac{(\alpha_a + \alpha_c)i_0 F}{RT}(-\tilde{\Phi}) \tag{4.7}$$

The passive case is modeled using a constant-phase element (CPE) with an impedance of

$$Z_\mathrm{CPE} = \frac{1}{(\mathrm{j}\omega)^\alpha Q} \tag{4.8}$$

where the phase angle is independent of frequency. When $\alpha = 1$, Q has units of capacitance. When α does not equal unity, the system has a distribution of time constants or surface heterogeneity either normal or parallel to the surface.[34] The expression used to represent blocking behavior at the steel for the normal current density of a CPE is

$$\tilde{i} = -\tilde{\varphi}\omega^\alpha Q\left[\cos(\alpha\frac{\pi}{2}) + \mathrm{j}\sin(\alpha\frac{\pi}{2})\right] \tag{4.9}$$

The oscillating potential is found by solving Laplace's equation with the given frequency-dependent boundary conditions.

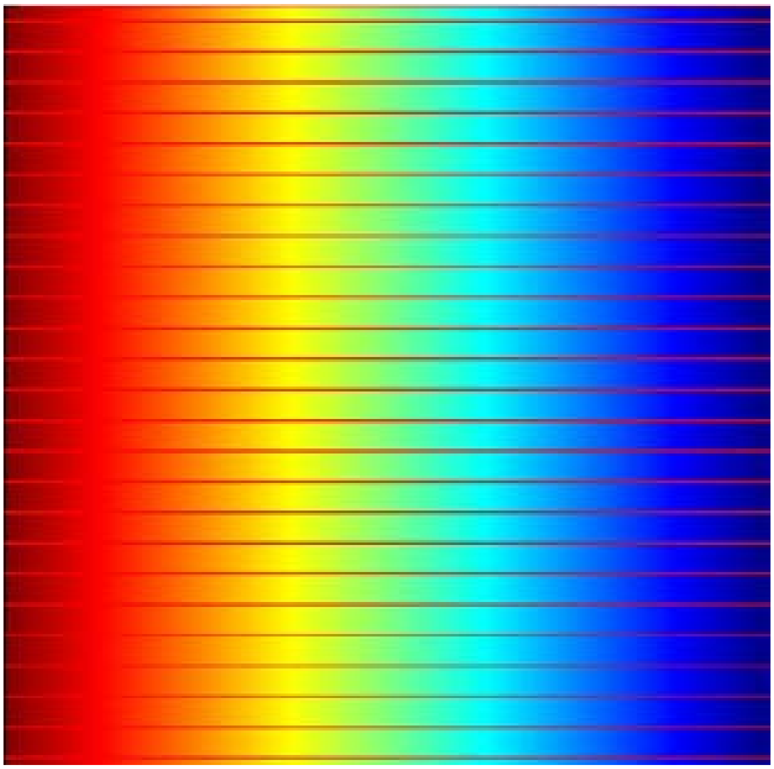

Figure 4.1: Calculated current and potential distribution for a two-dimensional 1-cm by 1-cm square of uniform 10 Ωm resistivity with current injecting electrodes placed on the vertical sides.

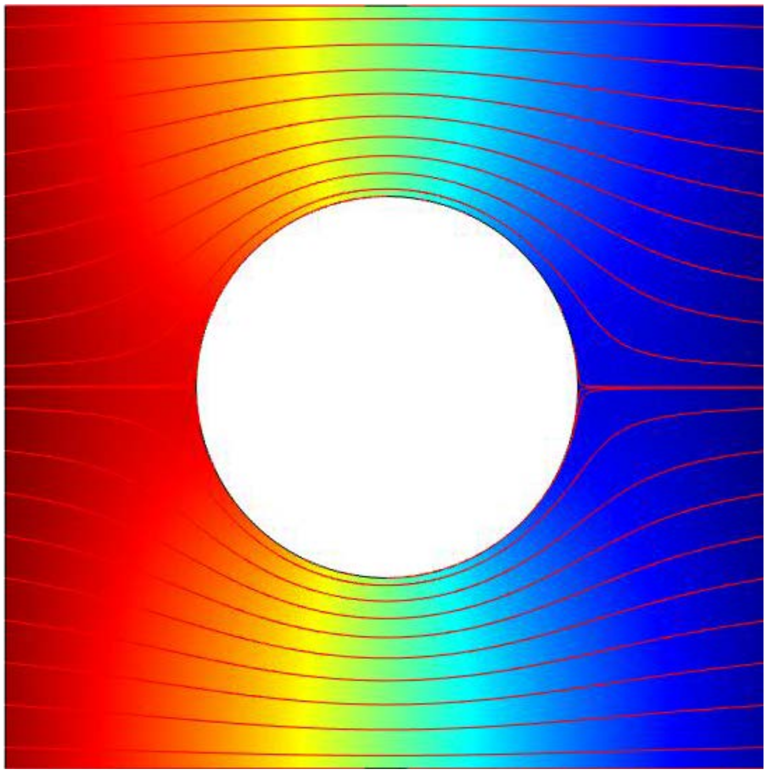

Figure 4.2: Current and potential distribution at the low-frequency limit for the system shown in Figure 4.1 with a 0.25-cm radius steel placed in the center and current injecting electrodes placed on the vertical sides.

4.2 Justification of Boundary Conditions

A two-dimensional square of uniform resistivity, shown in Figure 4.1, was modeled to confirm the oscillating current boundary conditions. The vertical sides of the square acted as the current-injecting electrodes. The potential distribution is shown by the color gradient in Figure 4.1, and the current path is shown by the horizontal red lines. The two-electrode impedance was simulated by dividing the potential difference between the electrodes by the total current crossing one of the electrode boundaries. At all frequencies, the real part of the impedance is given by the resistivity of the electrolyte multiplied by the distance between the electrodes and divided by the cross-sectional area. The imaginary impedance is zero since the grout is modeled as a homogenous material with a constant resistance without any dielectric properties.

A steel circular element was inserted into the grout model with the boundary condition described by Equation 4.7. The charge-transfer resistance was set to $R_{\mathrm{t}} = 100\ \Omega\mathrm{cm}^2$ and the double layer capacitance was $C_{\mathrm{dl}} = 2\ \mu\mathrm{F/cm}^2$. At low frequencies, Figure 4.2, the steel behaves as an open circuit due to the dominance of the charge-transfer resistance and repels the current. At high frequencies, Figure 4.3, it behaves as a closed-circuit and the current enters the steel normal to the surface. These results are consistent with those of Keddam et al.[24] The Nyquist plot of the simulated impedance, Figure 4.4, is a capacitive loop representative of a resistor and a capacitor in parallel. This is a simple model that

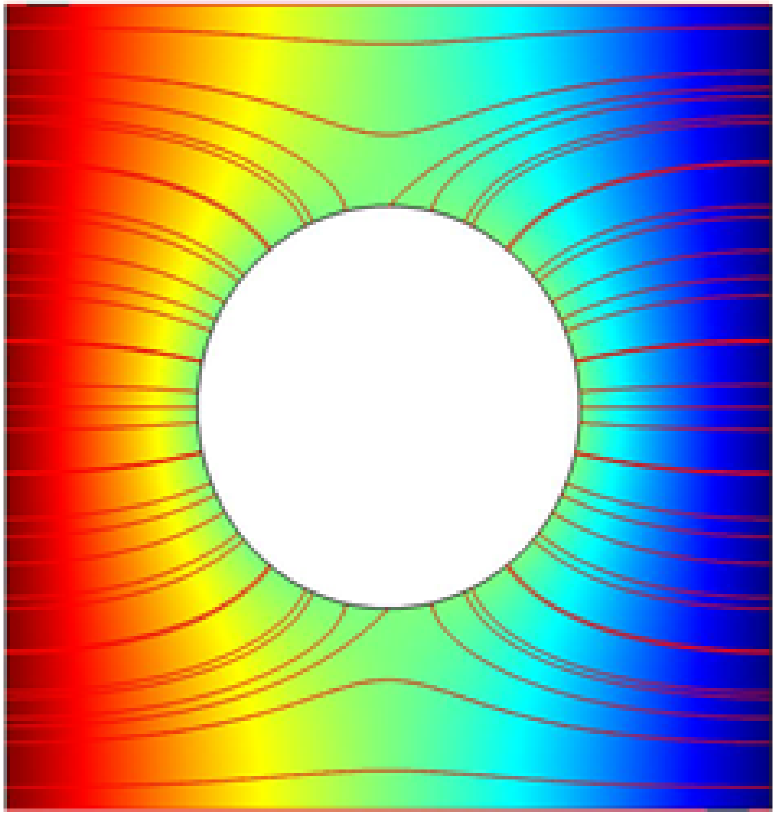

Figure 4.3: Current and potential distribution at the high-frequency limit for the system presented in Figure 4.2.

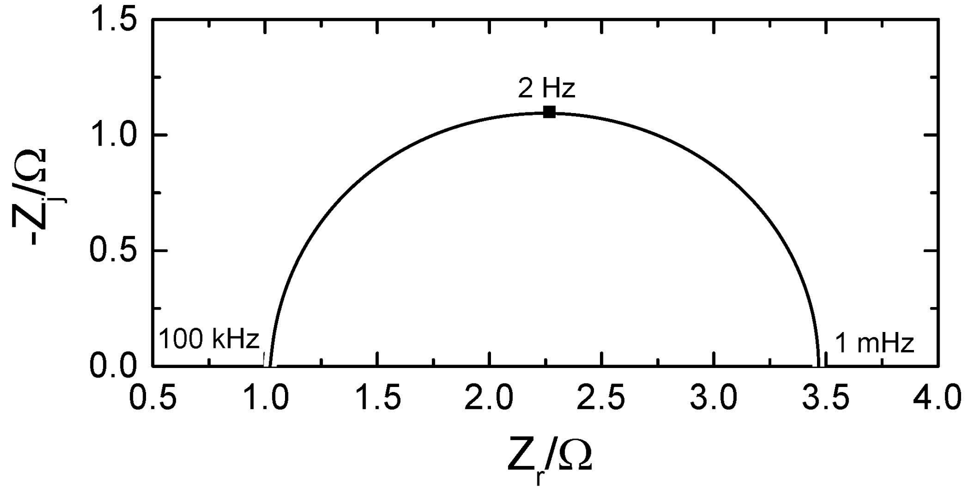

Figure 4.4: Simulated impedance of a 1-cm square grout model with a 0.25 cm radius steel circle placed in the center and current injecting electrodes placed on the vertical sides.

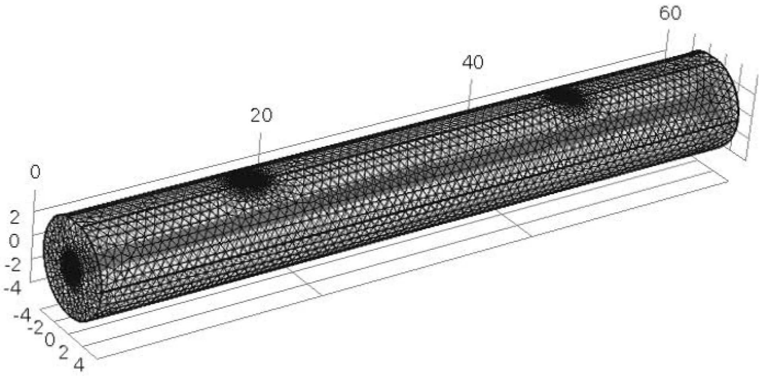

Figure 4.5: Mesh of the 3D tendon model.

shows the concept of indirect impedance, and confirms the use of the oscillating boundary conditions.

A three-dimensional, 60cm long cylindrical section of a tendon was modeled, with and without steel, to simulate the impedance of a post-tensioned tendon. The steel strand is 0.625cm in radius and is located along the longitudinal axis of the cylinder. All dimensions of the model were made to match the fabricated tendons. The mesh of the model, Figure 4.5, is composed of free tetrahedral elements which decrease in size at the electrode boundaries. Boundary-layer elements were added to the steel and electrode boundaries. Reference electrodes were placed along the surface to analyze the potential distribution along the surface.

4.3 Results and Analysis

The simulated indirect impedance is presented for a finite-element model of a tendon with one steel strand. The parameters used were $R_\mathrm{t} = 11.8$ kΩcm^2, $C = 20$ μF/cm^2, and $\rho = 125$ Ω m. An equivalent circuit is presented to fit the impedance based on the ohmic impedance of the grout and the interfacial impedance of the steel. A simplified analogue circuit is presented which reduces the equivalent circuit to three components. A sensitivity analysis of the parameters to changes in steel polarization resistance as well as the distance between the measurement electrodes is also presented.

4.3.1 Experimental Data Fitting

The passive case simulation was used to iteratively fit the experimental impedance by first estimating the resistivity of the grout as 125 Ω-m and iterating the CPE parameters at the steel. Q was found to be 0.9 Ss$^\alpha$ and α was 0.9. The simulated impedance is shown to fit experimental data of 2 electrode configurations at low frequencies, provided in Figures 4.6 and 4.7. The fitting of the indirect impedance for two different electrode configurations is a validation of our finite-element model in its ability to replicate experimental measurements and therefore may be used to establish an interpretation procedure.

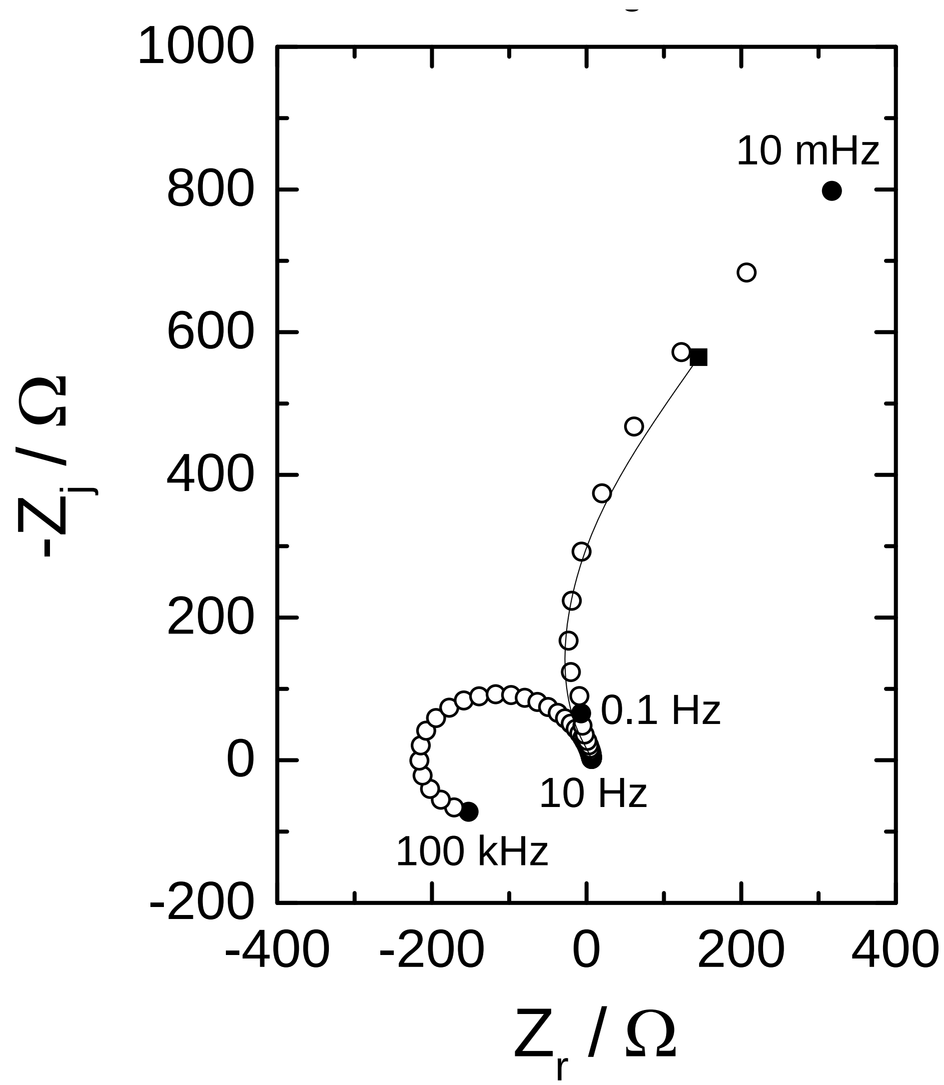

Figure 4.6: Simulated impedance results compared to the experimental results with an electrode configuration of 1357.

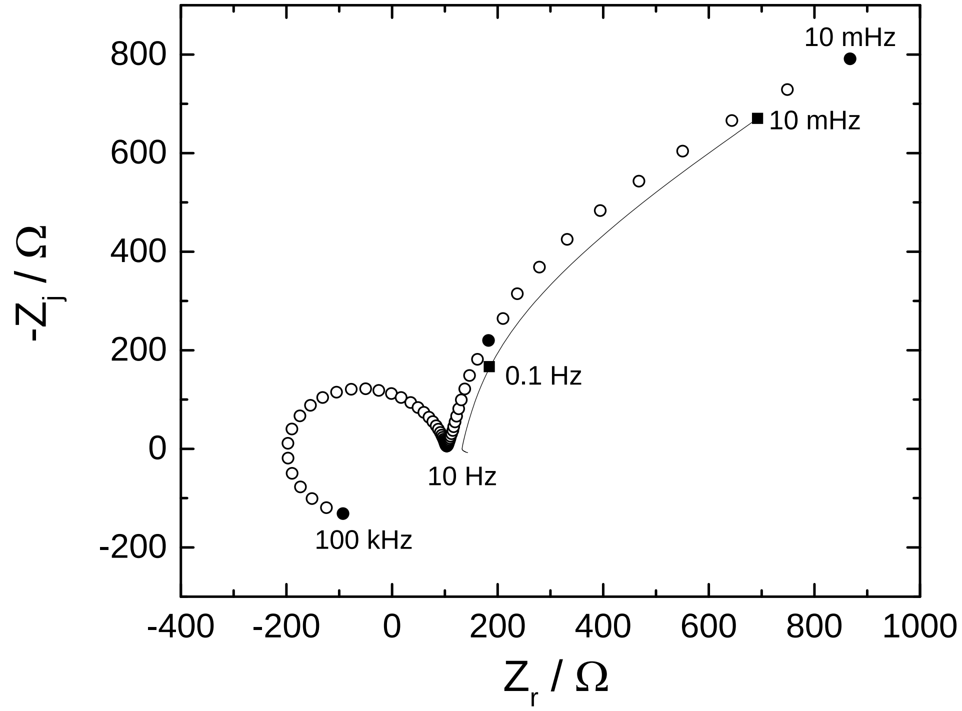

Figure 4.7: Simulated impedance results compared to the experimental results with an electrode configuration of 2356.

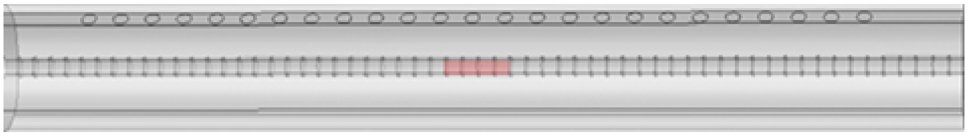

Figure 4.8: Tendon model with locally corroding section in the center of the steel.

4.3.2 Determination of Steel Sensing Area

The area of steel that is sensed for each electrode arrangement is required for interpretation. The indirect impedance was simulated for three different cases: a fully passive steel strand, a uniformly corroding steel strand, and a passive strand with a localized area of corrosion at the center indicated by the red section in Figure 4.8. Twenty-five electrode points were placed along the surface such that multiple electrode configurations could be simulated at once.

In one set of simulations the electrodes were placed with the centerline of the array directly over the active site as is shown in Figure 4.9. The distance between the two reference electrodes was varied from 32 cm to 4 cm to determine if there is a maximum distance in which the corrosion could not be detected. When the electrodes were spaced at 32 cm, the difference between the passive case and the locally corroding case was extremely small. As the electrodes were moved closer together, the difference increased, but, even when the reference electrodes were placed just above the active location, Figure 4.10, the impedance of the locally corroding case alone did not indicate the presence of corrosion. However, the

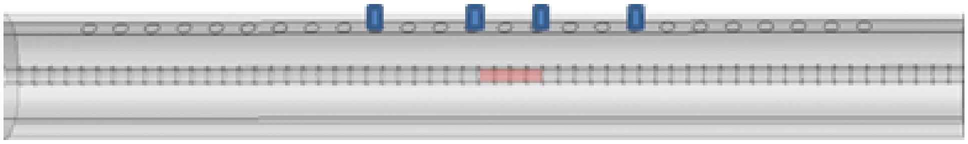

Figure 4.9: Schematic representation of the system geometry for a reference electrode spacing of 4 cm.

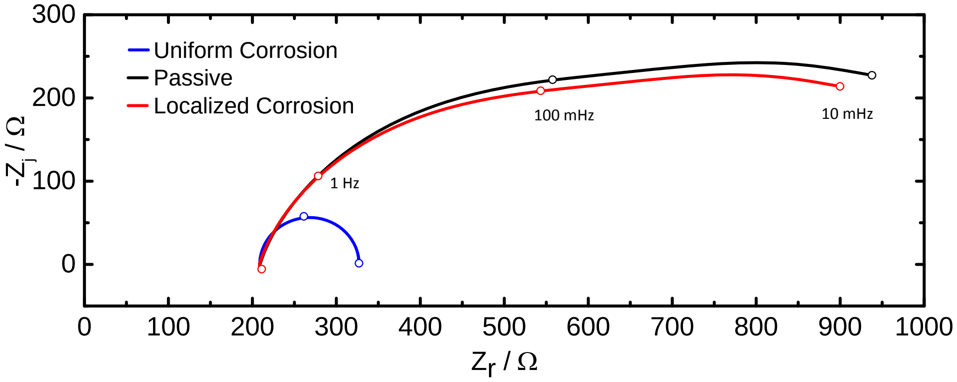

Figure 4.10: Simulated indirect impedance of a 2-ft model tendon containing one steel strand for a passive case, a locally corroding cases of 4 cm at the midpoint of the steel strand, and a uniformly corroding steel for a reference electrode spacing of 4 cm.

presence of a small difference, even when the reference electrode distance is 32 cm, indicates that the polarized steel area extends far out from the electrode points, but the location of steel most sensed by the indirect impedance is not at the centerline of the electrode array.

In another set of simulations, the electrodes were equally spaced at 4 cm and were moved along the tendon to mimic a likely procedure for a field application. In this case, when the midpoint of the electrode array was 18 cm left of the active location, the impedance of the passive and the actively corroding case showed only small differences at lower frequencies. When the electrodes were located 10 cm from the corroding section, the difference became more apparent. However, when one of the reference electrodes was directly over the site of corrosion, the difference diminished. The most prominent difference occurred when the current injection electrode was directly over the site of corrosion, as is shown in Figure 4.11. The simulated impedance results for this configuration are shown in Figure 4.12 in Nyquist format. The passive case shows one depressed capacitive loop, while the corroding case shows two overlapping time constants.

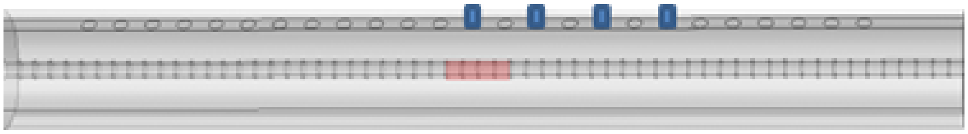

Figure 4.11: Schematic representation of the system geometry for a reference electrode spacing of 4 cm.

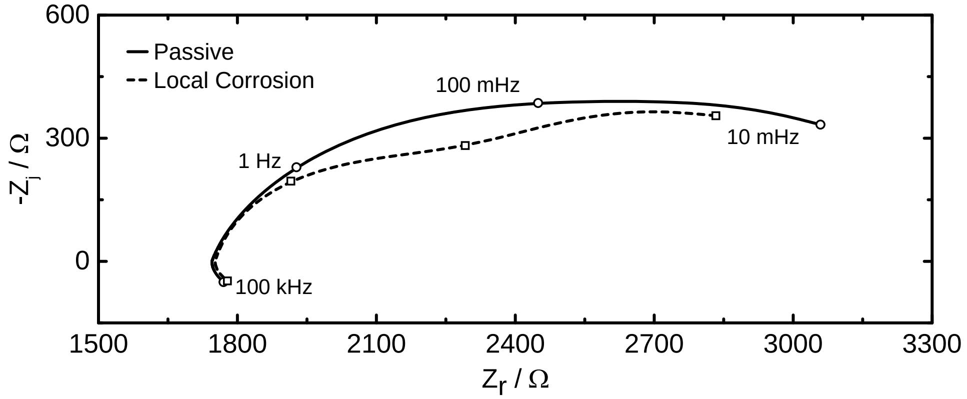

Figure 4.12: Simulated indirect impedance for a 2-ft model tendon containing one steel strand for a passive case (solid line). For the curve marked "Local Corrosion" (dashed line), corrosion was simulated for 4 cm length of strand located at the midpoint of the steel strand. The centerline of the electrode array was 6 cm to the right of the centerline such that a working electrode was located directly over the corroding area.

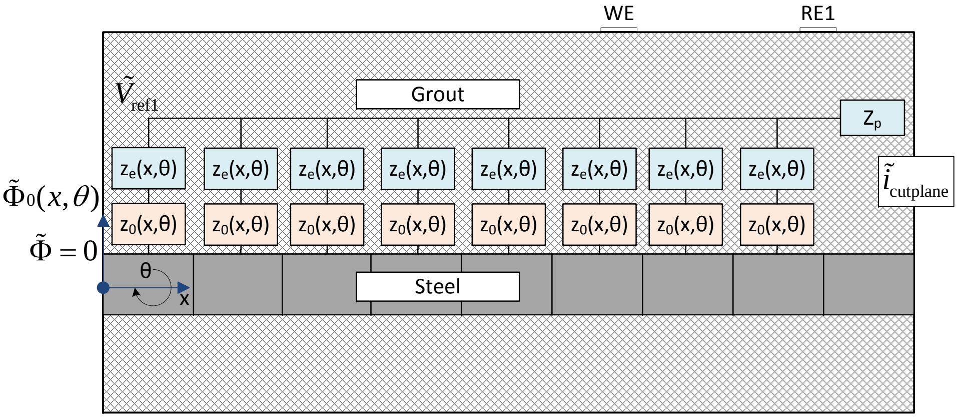

Figure 4.13: Equivalent circuit diagram used to represent the indirect impedance.

4.3.3 Equivalent Circuit

During the indirect impedance measurement, current flows through the grout as well as through the steel. If the contribution of the grout resistivity to the indirect impedance can be determined, then the total steel impedance may be extracted. All previous researchers have attempted to address the contribution of the grout resistivity to the indirect impedance with the use of resistors in series or parallel to the impedance of the steel. However, due to the nonuniform potential distribution along the surface of the steel and throughout the resistive material, the contribution of the grout must be in the form of an ohmic impedance with real and imaginary parts.

The appropriate equivalent circuit model for an indirect impedance measurement is shown in Figure 4.13. There are two primary current paths from the working electrode to the counter electrode. The current may either run parallel to the steel or in series to the steel. Since some of the current can take one path while the rest takes the other, these two paths

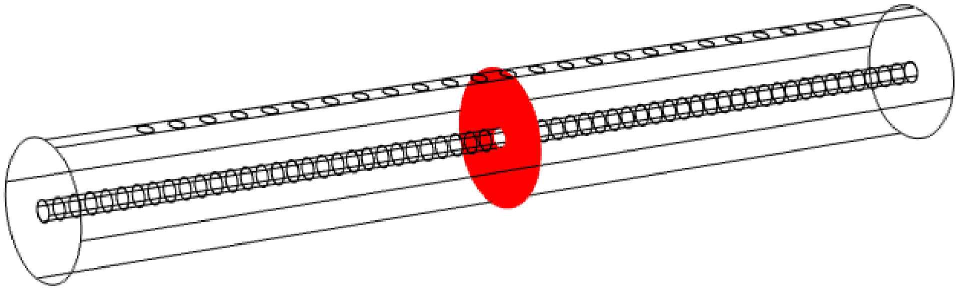

Figure 4.14: Cut plane used to determine the oscillating current through the grout.

must be in parallel. The impedance of the parallel path may be expressed as

$$Z_{\mathrm{parallel}} = \frac{\tilde{V}_{\mathrm{ref1}} - \tilde{V}_{\mathrm{ref2}}}{\tilde{i}_{\mathrm{cutplane}}} \tag{4.10}$$

in which the potential difference between the two reference electrodes is divided by the total current through a plane located at the midpoint of the electrode array as shown in Figure 4.14. The plane only includes the cross-section of the resistive material and not the steel.

The series path impedance must contain the impedance through the grout as well as the interfacial impedance of the steel. Due to the nonuniform potential distribution throughout the grout and along the steel surface the series path impedance must be expressed as

$$Z_{\mathrm{s}} = \left(\int_0^{60} \int_0^{360} \frac{1}{z_{\mathrm{e}}(x,\theta) + z_0(x,\theta)} d\theta dx \right)^{-1} \tag{4.11}$$

in which the sum of the local ohmic and interfacial impedances as a function of position on the surface of the steel are integrated in a parallel fashion. A diagram showing the local ohmic and interfacial impedances configurations is provided in Figure 4.13.

The local ohmic impedance is calculated as

$$z_{\mathrm{e}}(x,\theta) = \frac{\tilde{V}_{ref} - \tilde{\Phi}_0(x,\theta)}{\tilde{i}_0(x,\theta)} \tag{4.12}$$

which is based on the potential difference of the reference electrode and the potential on a point of the steel. The modulus of the ohmic and interfacial impedances is presented in Figure 4.15 as a function of axial location for $\theta = 0$. The solid lines represent the local ohmic impedance and the dashed lines represent the local interfacial impedance. The interfacial impedance is uniform along the steel surface and increases with frequency. The ohmic impedance is nonuniform along the length of the steel and reaches a minimum at the working and counter electrode locations. The ohmic impedance outside the electrode array increases with increases in frequency. At high frequencies, the series path impedance is mostly comprised of the ohmic impedance contribution. At low frequencies the interfacial impedance is on the same order as the ohmic impedance at locations near the working and counter electrodes. The results presented in Figure 4.15 provide an explanation for the sensitivity to corrosion observed below the current injection electrodes.

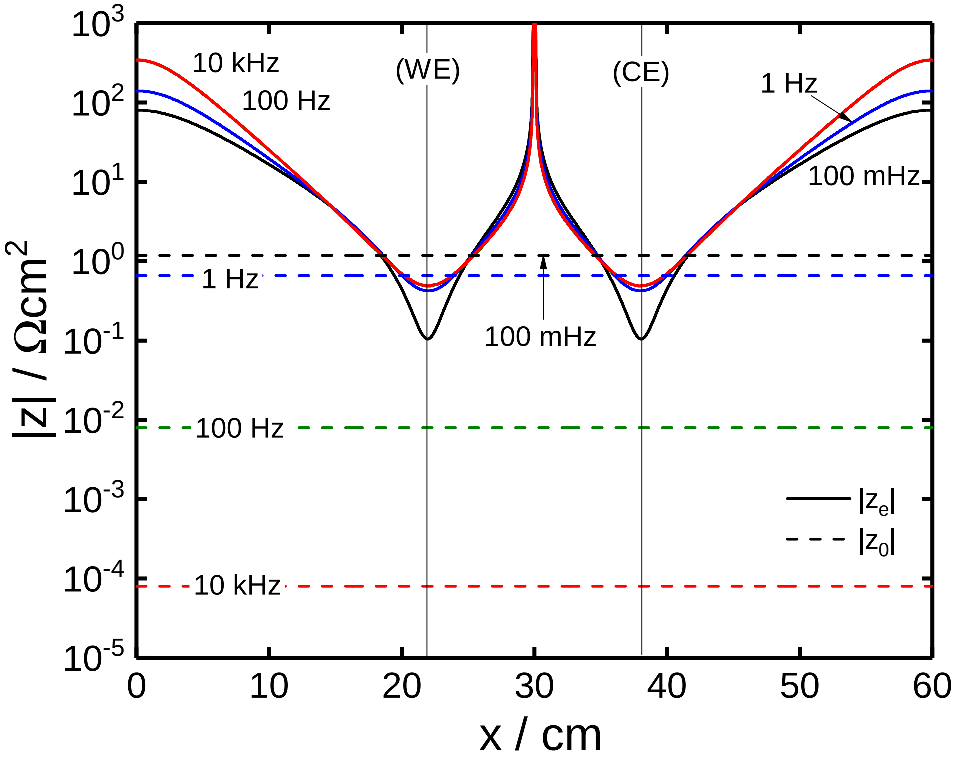

Figure 4.15: Magnitude of the series local ohmic impedance (solid lines) and the local interfacial impedance (dashed lines) as a function of steel position with frequency as a parameter.

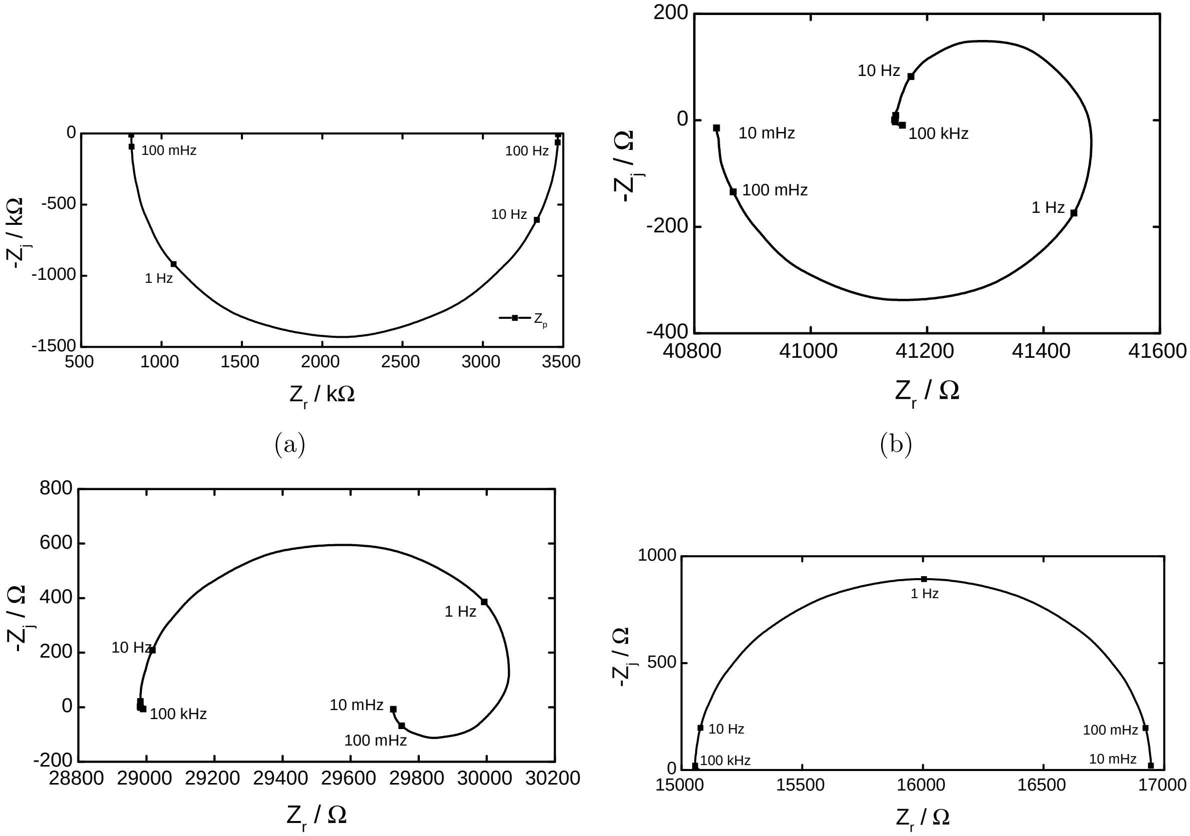

(a) (b)

(c) (d)

Figure 4.16: The ohmic impedance of a segment located at: (a) 1 cm, (b) 16 cm, (c) 17 cm, and (d) 26 cm.

For simplicity, the series path impedance was calculated by segmenting the steel surface into 1 cm by 90° sections and calculating the global ohmic and interfacial impedances of each section. The series impedance was then evaluated as the parallel combination of the global impedances between the reference electrode and a segment of the steel surface. The ohmic impedance between the reference electrode and a segment of steel may be expressed as

$$Z_{\text{e,segment}} = \frac{\tilde{V}_{\text{ref1}} - \tilde{V}_{\text{avg,segment}}}{\tilde{i}_{\text{segment}}} \tag{4.13}$$

The ohmic impedance of the first half of the steel segments is calculated based on $\tilde{V}_{\text{ref1}}$ and the second half of the segments is calculated using $\tilde{V}_{\text{ref2}}$. It is necessary to segment the steel to account for the large variation in potential along the steel surface which results in a distribution of local ohmic impedance.

The ohmic impedance to the steel is shown in Figure 4.16 in Nyquist format for three segments of steel located outside the electrode array and one located inside the array. The locations of the segments of the steel are expressed in terms of distance along a number line with the origin (x=0cm) placed at the left. The ohmic impedance at 1 cm, shown in Figure 4.16(a), is inductive and at 16 cm (Figure 4.16(b)) and 17 cm (Figure 4.16(c)), which are

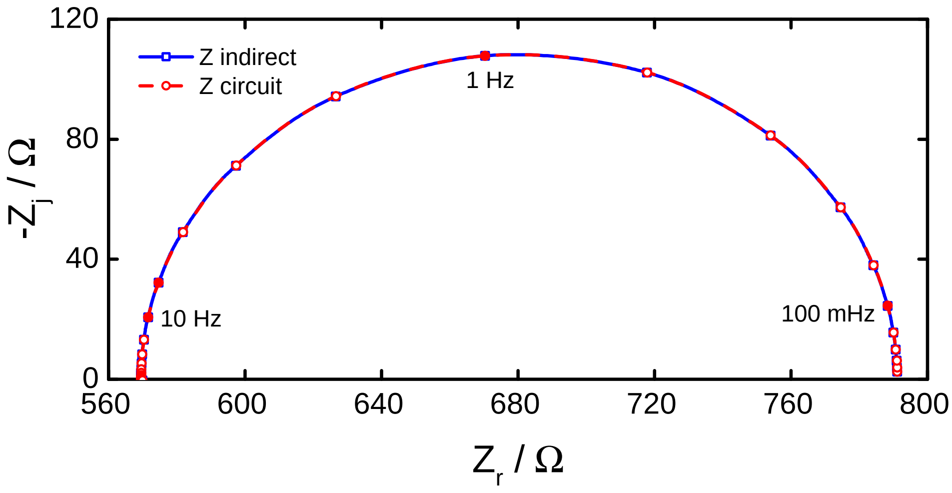

Figure 4.17: Simulated indirect impedance and equivalent circuit impedance calculated using Equation 4.17 in Nyquist format.

closer to the electrode array, the impedance is capacitive at high frequencies and inductive at low frequencies. The ohmic impedance at location 26 cm (Figure 4.16(d)), which is located within the electrode array, is capacitive.

The total series impedance for each section of steel may be expressed as

$$Z_{\text{segment}} = Z_{\text{e,segment}} + Z_{0,\text{segment}} \tag{4.14}$$

where $Z_{0,\text{segment}}$ represents the interfacial impedance and may be expressed as

$$Z_{0,\text{segment}} = \frac{\tilde{V}_{\text{avg,segment}}}{\tilde{i}_{\text{segment}}} \tag{4.15}$$

which is the quotient of the average oscillating potential of a segment and the oscillating current through segment. The complete series impedance may be expressed as

$$Z_{\text{series}} = \frac{1}{\sum_{1}^{\text{segments}} \frac{1}{Z_{\text{segment}}}} \tag{4.16}$$

which is a parallel combination of the series impedances for each segment. The indirect impedance may be expressed as

$$Z_{\text{indirect}} = \frac{Z_{\text{series}} Z_{\text{parallel}}}{Z_{\text{series}} + Z_{\text{parallel}}} \tag{4.17}$$

representing a parallel combination of the series path impedance and the parallel path impedance.

A comparison of the simulated indirect impedance and the impedance calculated using Equation 4.17 is shown in Figure 4.17. The two impedances are nearly identical. Any error between the simulated indirect impedance and the circuit impedance is due to the averaging of the potential along the surface of each steel segment. The error decreases with decreases in the size of the segments. The breakdown of the indirect impedance presented here may also be extended to account for multiple steel strands. The series ohmic impedance to each strand may be calculated and each of them would be added in parallel.

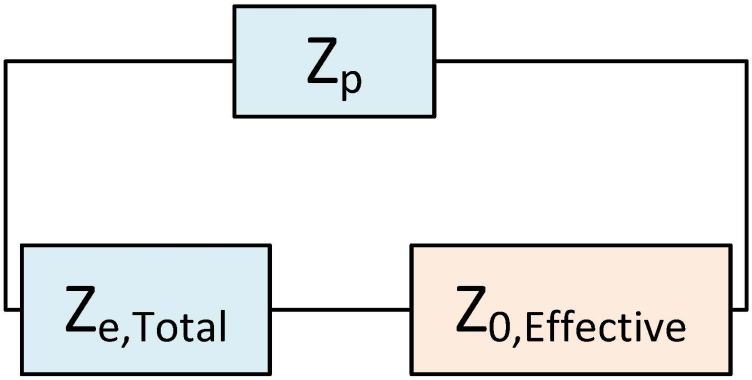

Figure 4.18: Reduced analogue circuit used to represent the indirect impedance.

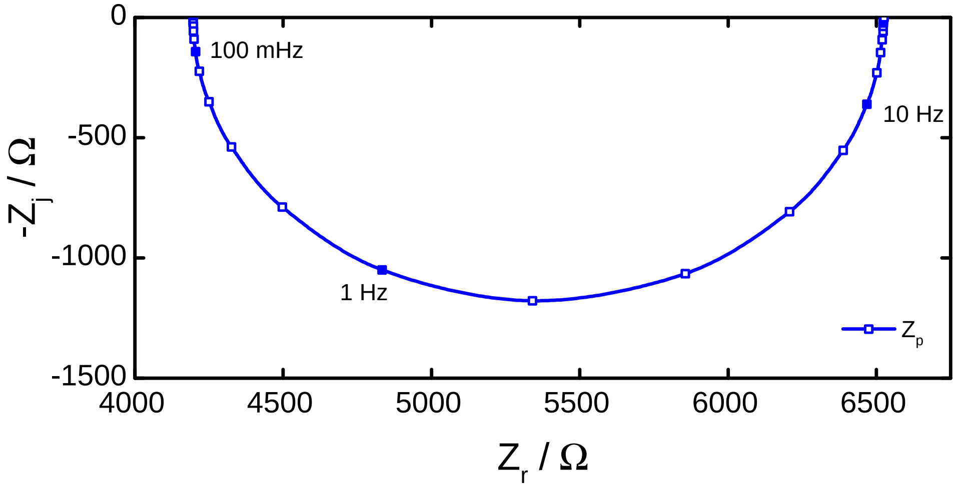

Figure 4.19: Simulated parallel ohmic impedance.

4.3.4 Circuit Analogue

Due to the nonuniform current distribution imposed by the unusual geometry of the electrode configuration in an indirect impedance measurement, the contribution of the grout resistivity to the overall indirect impedance is in the form of an ohmic impedance and has real and imaginary parts. Therefore, an equivalent circuit containing linear elements that properly describes the system is not feasible.

A more appropriate circuit expresses the contribution of the grout resistivity in terms of an ohmic impedance such as the circuit shown in Figure 4.18. The parallel path impedance is the same as expressed in Equation 4.10 for the equivalent circuit. The parallel ohmic impedance is presented in Figure 4.19. The parallel impedance is inductive and is large in comparison to the overall impedance.

As described in equation 4.14, the series path impedance contains the series ohmic contribution of the grout as well as the steel interfacial impedance. To subtract the total steel interfacial impedance from the series path impedance, the effective polarized area of steel needs to be estimated. Technically, the entire steel surface is polarized since the poten-

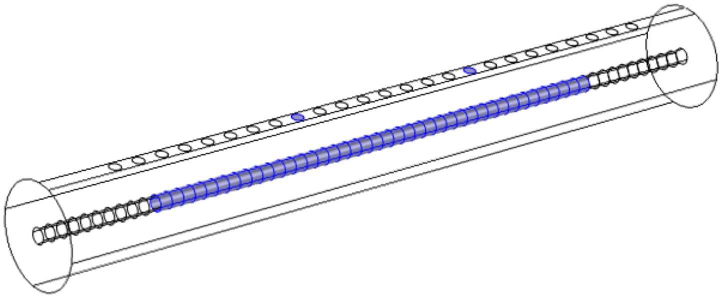

Figure 4.20: Schematic showing the effective area of polarized steel.

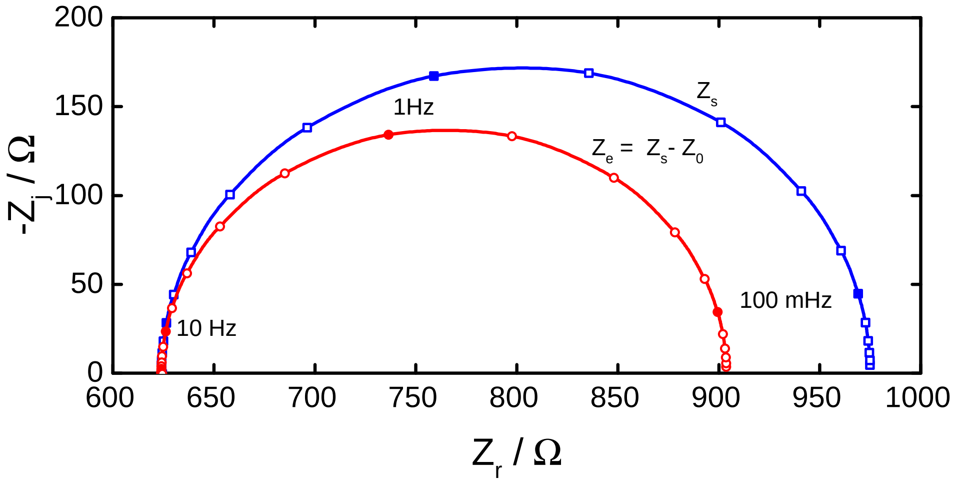

Figure 4.21: Series path simulated impedance and series simulated ohmic impedance.

tial everywhere along the steel is non-zero. However, steel segments that are far from the current-injecting electrodes have a larger ohmic contribution and a smaller influence of the steel interfacial impedance.

The effective area of polarized steel was determined by decreasing the polarization resistance of a segment by a factor of 10 and assessing the change in the overall impedance. If the low-frequency limit of the indirect impedance changed by more than one percent, the segment of steel was categorized as polarized. The effective area of polarized steel is shown in Figure 4.20. The effective area of steel that is polarized during the indirect impedance did not include the outer 10 cm of the steel strand.

The effective series ohmic impedance, shown in Figure 4.21, was found by subtracting the total interfacial impedance based on the effective polarized area of steel from the series path impedance, also presented in Figure 4.21. The series and parallel ohmic impedances confound interpretation of the indirect impedance. However, without taking into account the variation in ohmic impedance as a function of frequency, the polarization resistance of

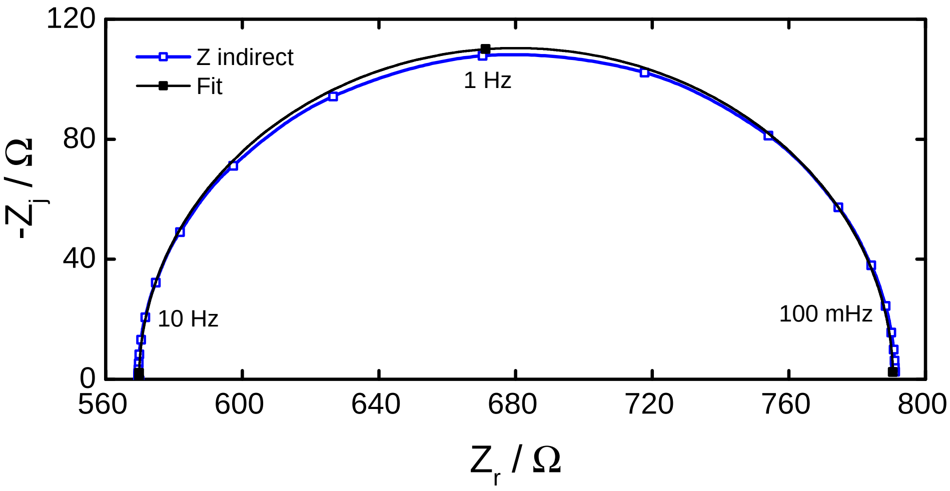

Figure 4.22: Simulated indirect impedance and the impedance calculated from a circuit containing resistors instead of the series and parallel ohmic impedances.

the steel will be overestimated, resulting in an under prediction of the corrosion rate.

As an example, a circuit in which the series and parallel ohmic impedances were expressed as resistors was fit to the indirect impedance, shown in Figure 4.22. The regression yielded an estimated total polarization resistance of 313 Ω, whereas, the actual total polarization resistance based on the effective area of steel was 71.2 Ω. Without accounting for the complex nature of the ohmic contributions to the indirect impedance measurement, the polarization resistance was overestimated by a factor of more than four.

4.3.5 Influence of Electrode Configuration

The ohmic impedance parameters vary with changes in the placement of the measurement electrodes. Simulations were performed in which the distance between the reference electrodes was increased while the distance between the working electrode and counterelectrode were held fixed. Simulations were also performed in which the distance between the working electrodes was increased as the distance between the reference electrodes were held fixed. The effective series and parallel ohmic impedances were calculated for each case.

The series ohmic impedance is shown in Figure 4.23 in Nyquist format with the distance between the two reference electrodes as a parameter. The distance between the working electrode and counterelectrode was fixed at 14 in. while the distance between the references electrodes was increased from 2 in. to 10 in. by increments of 4 in. The results indicate that the series ohmic impedance is a strong function of the distance between the working electrodes and the reference electrodes. When this distance is large, the series ohmic impedance is inductive as is shown in the cases where the reference electrode spacing is 2 in. and 6 in. When the distance between the reference electrodes is 10 in. and the distance between the working electrode and the reference electrode is 2 in., the series ohmic impedance is capacitive. Another interesting feature is at low frequencies the series ohmic impedance is negative, which would lead to large distortions in the overall indirect impedance.

The parallel ohmic impedance is shown in Figure 4.24 for the same set of simulations

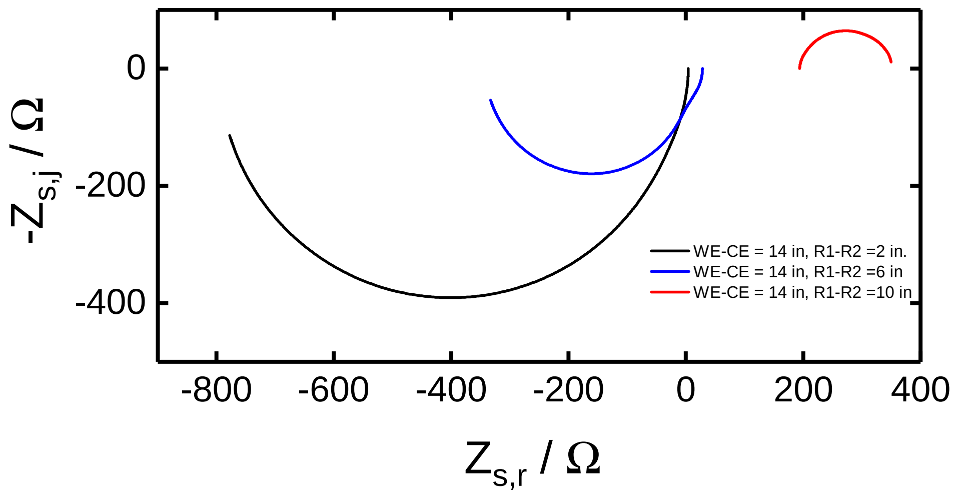

Figure 4.23: The series ohmic impedance in Nyquist format with the spacing between reference electrodes as a parameter.

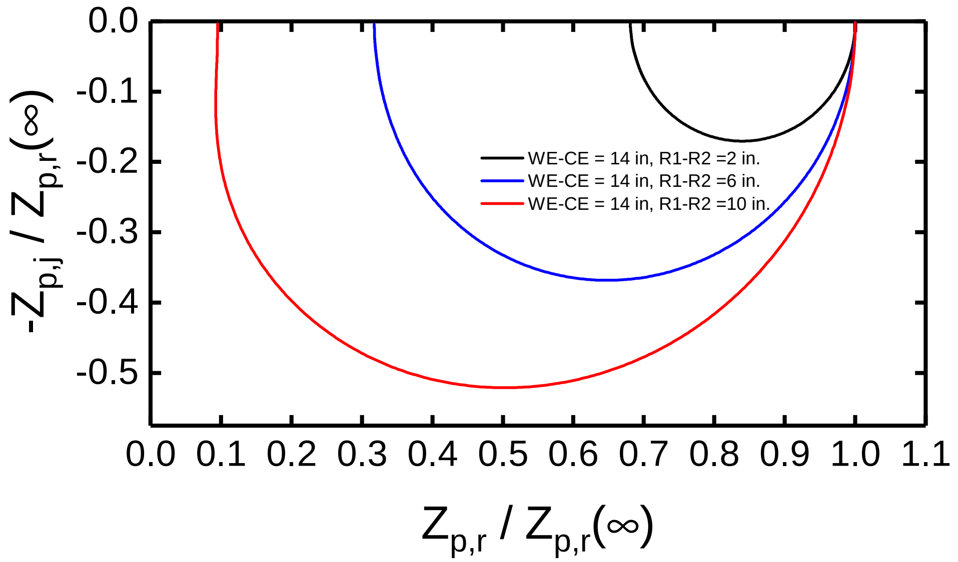

Figure 4.24: The parallel ohmic impedance scaled by the high frequency limit of the real part of the parallel ohmic impedance in Nyquist format with the distance between reference electrodes as a parameter.

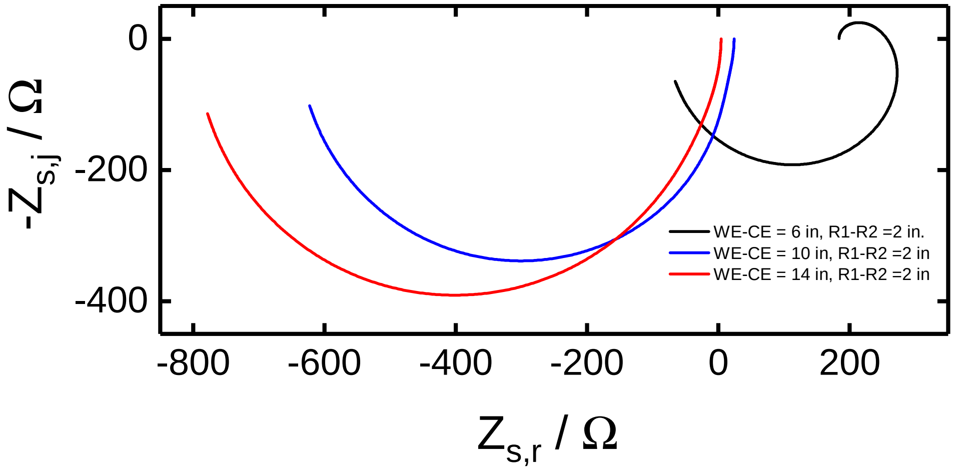

Figure 4.25: The series ohmic impedance in Nyquist format with the distance between the working and counter electrodes as a parameter.

presented in Figure 4.23. The results are shown in Nyquist format but scaled by the high-frequency limit of the impedance since the parallel impedance varied significantly with changes in the reference electrode spacing. The parallel ohmic impedance was inductive for each case and the size of the inductive loop increased with increases in the reference electrode spacing. Also, the shape of the inductive loop became more deformed with larger distance between reference electrodes.

The series ohmic impedance is shown in Figure 4.25 in Nyquist format with the distance between the working and counter electrodes as a parameter while the distance between the reference electrodes was fixed at 2 in. The results are similar to the case when the distance between reference electrodes was increased, which indicates that the series ohmic impedance is most sensitive to the distance between the working electrode and the reference electrode.

The parallel ohmic impedance is shown in Figure 4.26 in Nyquist format with the distance for the same electrode spacing as presented in Figure 4.25. The magnitude of the parallel ohmic impedance does not change much with changes in the distance between the working and counterelectrodes indicating that the parallel component of the ohmic impedance is most sensitive to the distance between the reference electrodes.

The overall indirect impedance is shown in Figure 4.27 scaled by the ohmic resistance for various electrode configurations to determine which electrode configuration yields the smallest amount of frequency dispersion. The greatest frequency dispersion is observed when the distance between the working and counter electrode is much larger than the distance between the two reference electrodes. The smallest amount of frequency dispersion is observed when the electrodes were equally spaced at a distance of 2 in. The indirect impedance would also change as the depth of the steel from the electrodes changes. However, if the electrodes are placed such that the distance between each electrode is uniform and that distance is close to the depth of the steel, the frequency dispersion will be minimal for systems with only one steel strand.

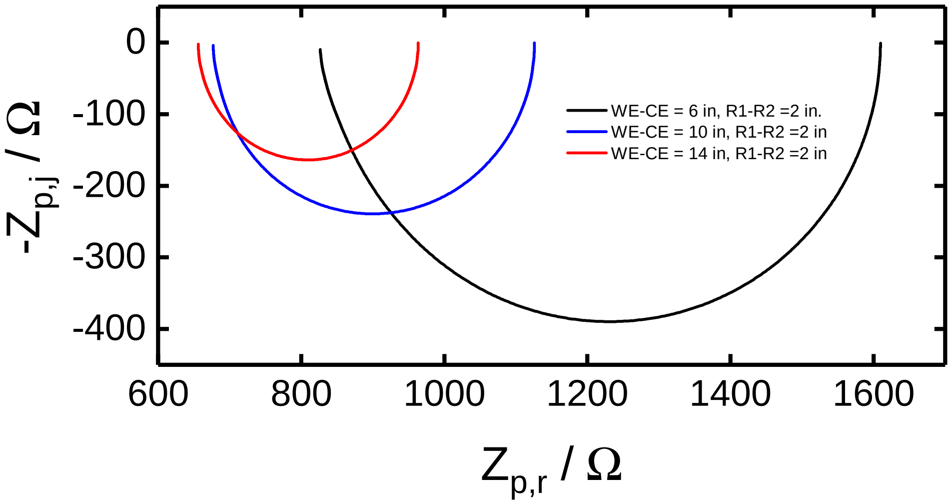

Figure 4.26: The parallel ohmic impedance in Nyquist format with the distance between the working and counter electrodes as a parameter.

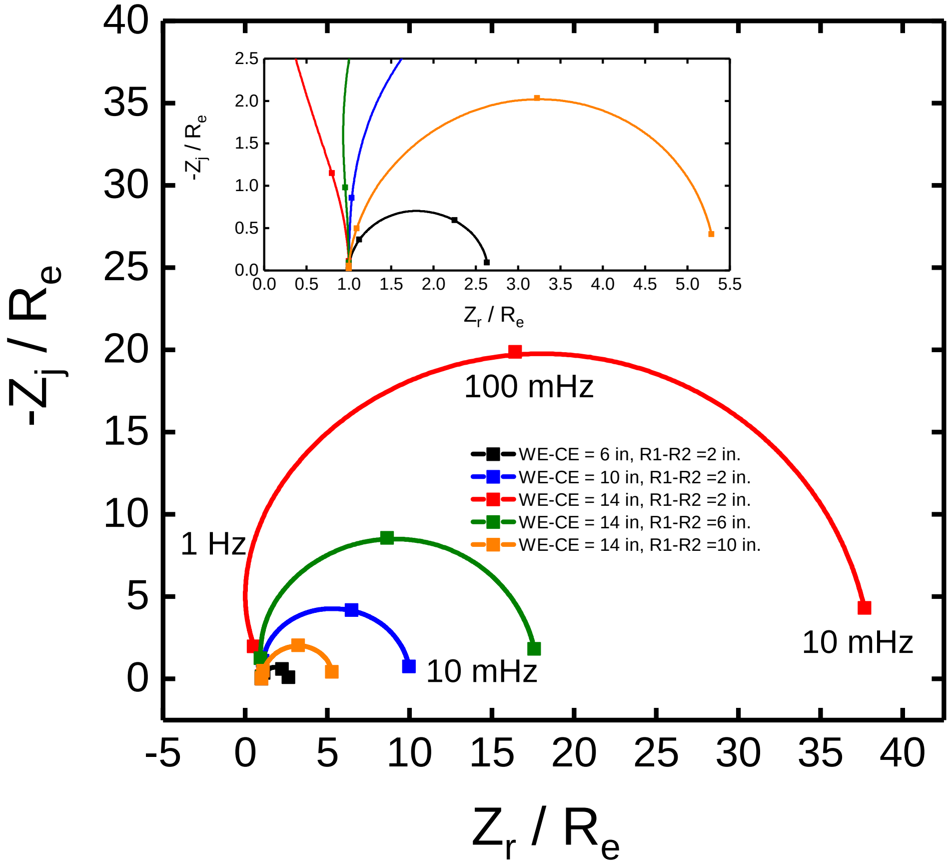

Figure 4.27: The simulated indirect impedance scaled by the ohmic resistance with electrode spacing as a parameter. Three simulations were performed for changes in reference electrode spacing, and the other three were for changing the spacing between the working and counter electrode.

4.3.6 Sensitivity to Steel Polarization Resistance

Simulations were performed in which the steel polarization resistance was increased to determine the sensitivity of the indirect impedance to the steel corrosion state. The variation in the steel and grout interfacial impedance is shown in Figure 4.28 with the polarization resistance as a parameter. The capacitance was held constant. As the polarization resistance is increased, the interfacial impedance becomes more capacitive. The corresponding indirect impedance is shown in Figure 4.29 in Nyquist format. The indirect impedance increases as the polarization resistance of the steel increases showing that the indirect impedance is sensitive to the steel condition.

The overall goal is to be able to measure the indirect impedance and somehow determine the interfacial impedance such that the corrosion rate may be estimated. The series and parallel ohmic impedance contributions to the indirect impedance makes the extraction of the interfacial impedance difficult. However, if these parameters can be estimated from the geometry of the system, estimating the steel polarization resistance may be feasible. The series and parallel ohmic impedances were calculated as a function of steel polarization resistance to determine how dependent the ohmic contribution of the indirect impedance is on the steel impedance. The series ohmic impedance is shown in Figure 4.30 with the polarization resistance as a parameter. As the polarization resistance increases, the series ohmic impedance also increases and becomes more inductive. However, the high-frequency limit does not change. The parallel ohmic impedance is shown in Figure 4.31 with the polarization resistance as a parameter. As with the series ohmic impedance, the parallel component also increases as the polarization increases. However, the low-frequency limit of the real part of the parallel ohmic impedance is more well defined. The high-frequency limit of the parallel ohmic impedance also does not change. Since the ohmic components of the indirect impedance are functions of the steel interfacial impedance, it would be difficult to predict these parameters solely from the geometry. Nevertheless, since the high-frequency limits are not dependent on the interfacial impedance, the ohmic resistance of the indirect impedance coupled with knowledge of the system geometry may be used to estimate the high-frequency limits of the series and parallel ohmic impedances.

4.3.7 Application to Ringling Tendon

The geometry of the tendon extracted from the Ringling Bridge was modeled using a finite-element simulation. The model geometry is shown in Figure 4.32 including the same electrode placement as was used for the experimental measurement. Impedance simulations were performed with the electrode array placed along the axis at one of the designated locations. In one case, all of the steel strands were modeled as passive. In another case, all of the steel strands were modeled as passive except for one which was modeled as uniformly corroding. The one corroding strand is labeled in Figure 4.32 with a solid red circle. The simulated impedance is presented in Figure 4.33 in Nyquist format with the location of the electrodes as a parameter for the case in which all of the strands were passive. Due to the location of the steel strands in relation to the location of the electrode probes, the simulated impedance had inductive features at high frequencies. These simulations show that the indirect impedance is sensitive to steel position, and it may be important to have a general sense of the location

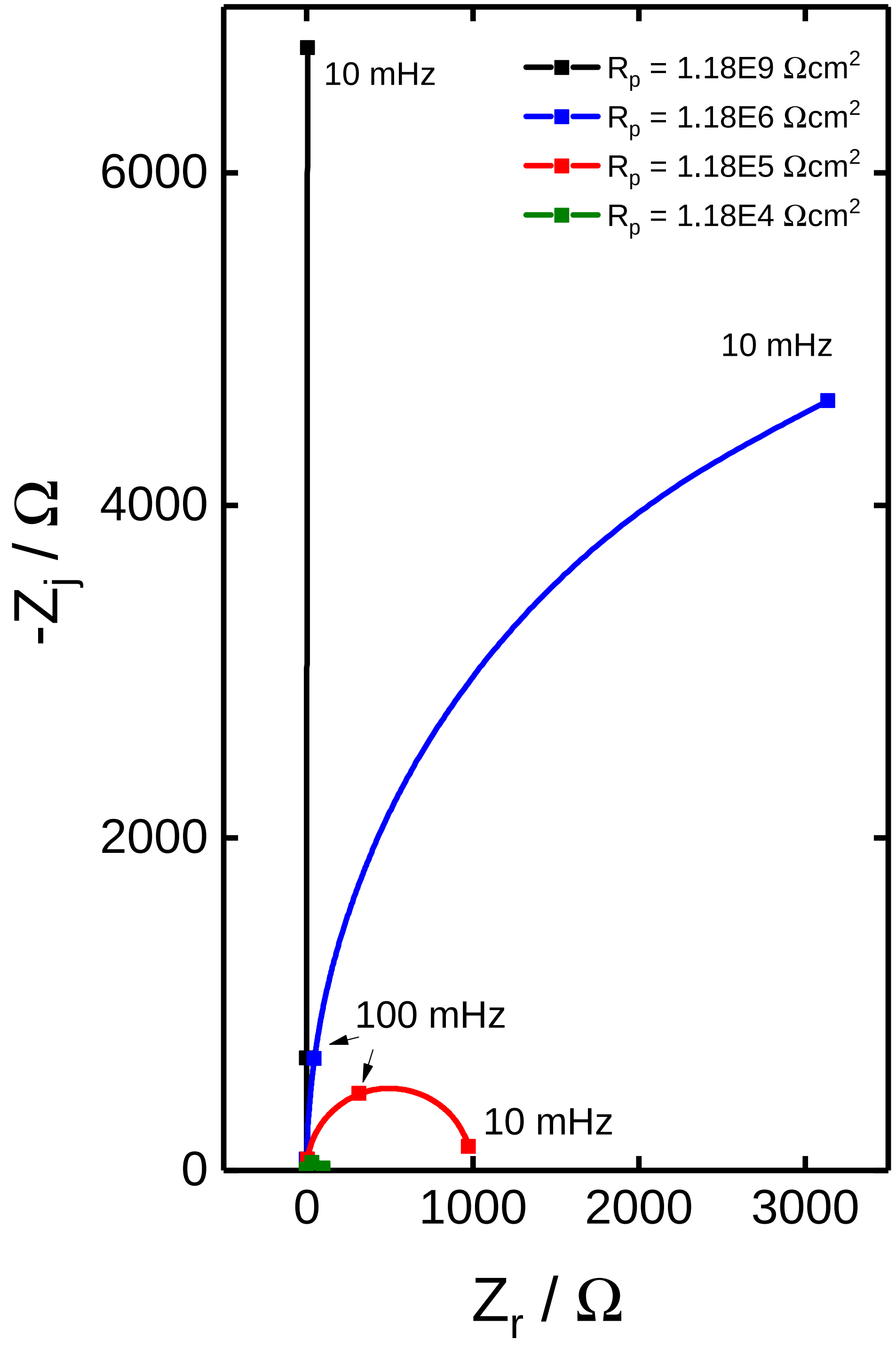

Figure 4.28: The interfacial impedance for a circuit with R_p in parallel with C_0 and with R_p as a parameter.

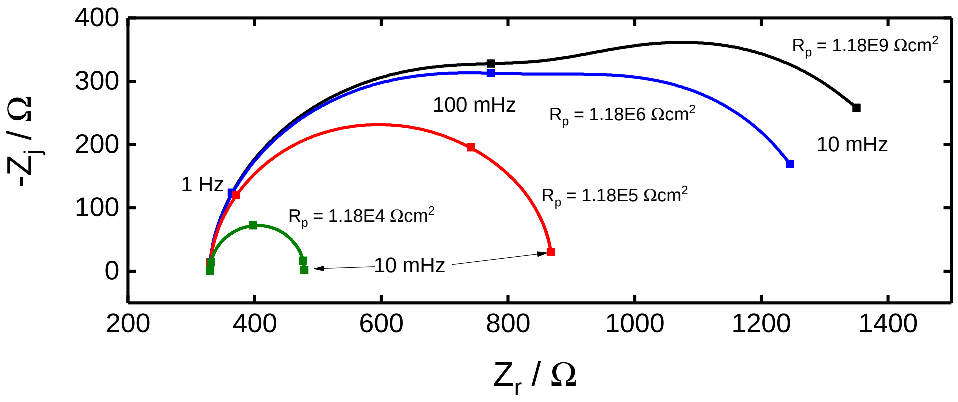

Figure 4.29: The simulated indirect impedance in Nyquist format with R_{p} as a parameter.

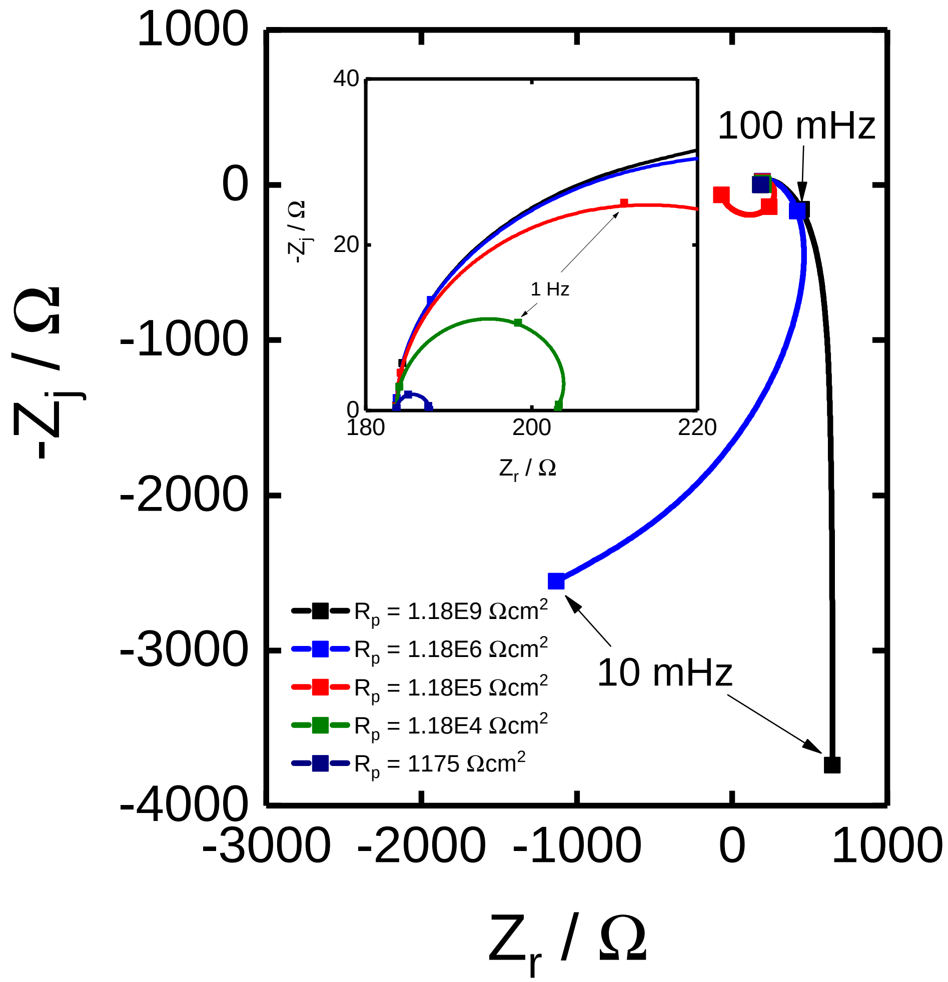

Figure 4.30: The series ohmic impedance in Nyquist format with R_{p} as a parameter.

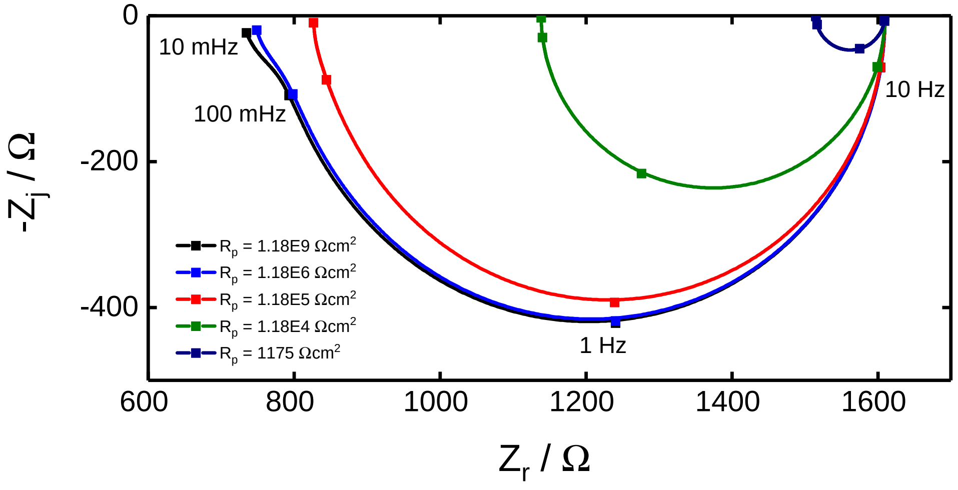

Figure 4.31: The parallel ohmic impedance in Nyquist format with R_p as a parameter.

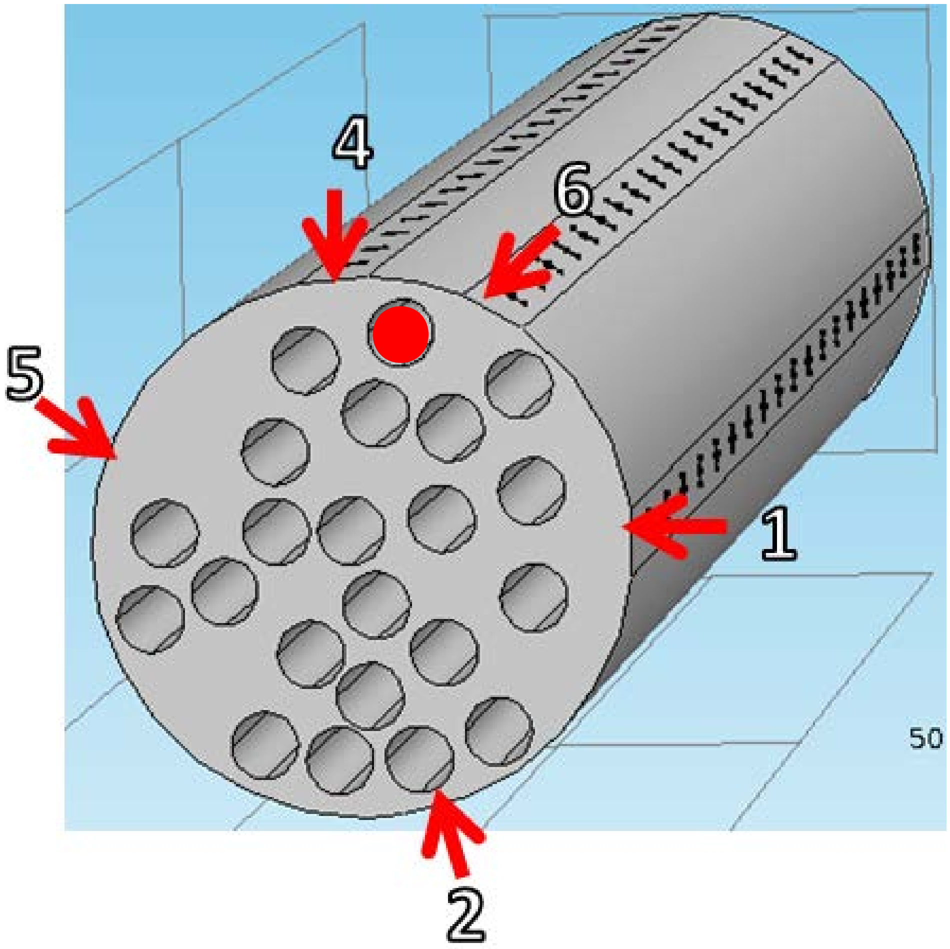

Figure 4.32: Finite-element representation of the Ringling Bridge tendon (see Figure 3.1).

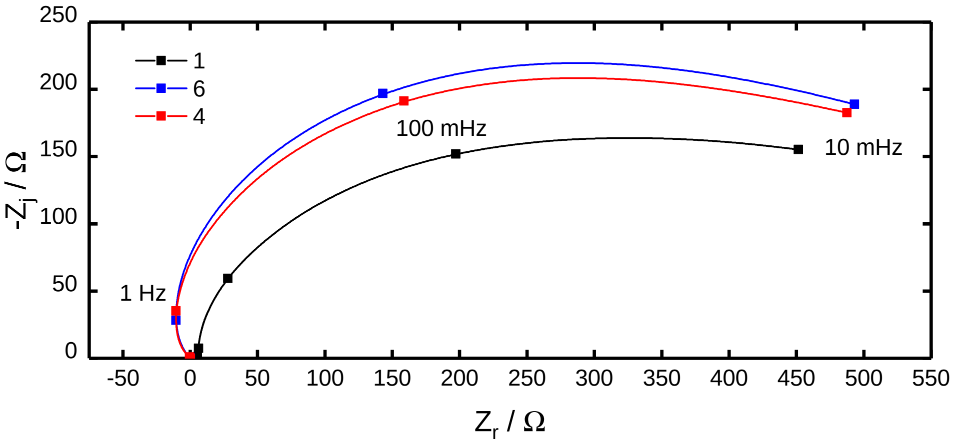

Figure 4.33: Simulated indirect impedance for a 2-ft. cylindrical tendon with passive steel strands dispersed throughout the grout according to the configuration shown in Figure 3.1.

of the steel strands to formulate a reasonable estimate of the corrosion rate.

Simulations were also performed in which the electrodes were placed circumferentially around the tendon as was done experimentally. The simulations were done with all the steel strand set to a passive boundary conditions as well as a scenario in which one of the steel strands was corroding, shown by the location of the red circle in Figure 4.32. The simulation results are presented in Figure 4.34 for the all passive case, represented by the solid lines, and when one of the strands is corroding, shown by the dotted lines. When the electrode probes were placed at locations 1-6-4-5, the difference between the passive case impedance and the corroding case was not extreme. The difference was more pronounced when the electrode probes were placed at locations 2-1-6-4. When the electrodes are placed longitudinally along the tendon, the indirect impedance measurement is most sensitive when the corrosion is directly beneath the working or counter electrode. The same is still true when the electrodes are placed circumferentially around the tendon.

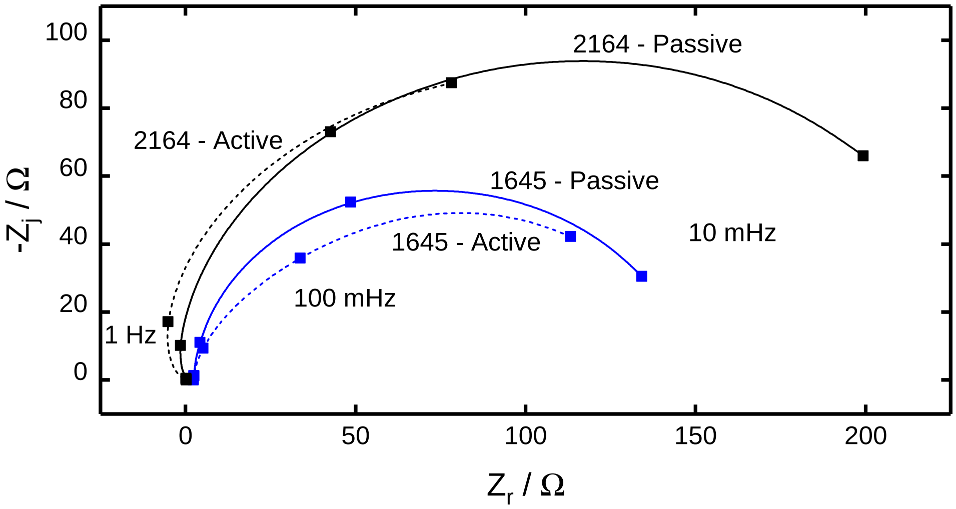

Figure 4.34: Simulated indirect impedance for a 2-ft. cylindrical tendon steel with strands dispersed within the grout according to the configuration shown in Figure 3.1 with corrosion state as a parameter.

Chapter 5

Discussion

Through the experience of performing indirect impedance measurements on the Texas A&M mock bridge and the tendons extracted from the Ringling Bridge, some difficulties were realized. If the electrodes are placed at a location where the steel is exposed from the grout, it is not possible to obtain an impedance measurement. If this occurs in the field, the electrode array should be shifted to a different location around the tendon. The results from the Texas A&M bridge did not show as much of the capacitive loop as did the measurements taken from the Ringling tendon. In fact, the magnitude of the impedance also varied significantly between the two cases. This may be due to the use of different grouts which may have different material properties. The variation of grout properties poses a major challenge in devising a general interpretation procedure. Also, since the indirect impedance is a function of the steel location, which would be difficult to determine a priori, any analysis aimed at estimating a corrosion rate of the steel would have to include a way of accounting for the grout properties.

The experiments and simulations both showed that the indirect impedance is a highly localized technique as it is only capable of detecting corrosion or at least showing significant signs of corrosion if it is located directly beneath the working or counter electrodes. Greatest sensitivity was seen at frequencies at or below 1 Hz. Otherwise, the measurement does not show qualitative signs of corrosion. There was no advantage to placing the electrodes circumferentially around the tendon instead of longitudinally. Therefore, if a measurement is taken at the top of the tendon and the corrosion occurs in the center, it will likely be undetected. However, corrosion was shown to occur in the locations of deficient grout formed at elevated locations of the tendon in cases where excess water was used to mix the grout.[77]

While there are many difficulties with the application of indirect impedance to corrosion detection in tendons, there are still clear advantages over existing technologies. The procedure for the indirect impedance measurement is relatively simple and does not require heavy equipment. Measurements are performed in approximately 20 minutes, and the holes that are drilled can be sealed if desired. The interpretation of the indirect impedance results is still a work in progress. Finite-element simulations were used to determine the sensitivity of the indirect impedance to corrosion. The present work contributes to the understanding of the influence of grout impedance to the measured indirect impedance and with more research, a reliable method to estimating the corrosion rate may be achieved.

Chapter 6

Conclusions

Indirect impedance was shown to be capable of monitoring the corrosion activity in post-tensioned tendons. Through proof-of-concept experiments in which tendon sections were fabricated with one steel strand and forced to corrode, it was determined that the indirect impedance is qualitatively sensitive to the corrosion rate of the steel. Finite-element models were used to simulate the indirect impedance response. The resistivity of the grout contributes to the overall impedance in two ways: a series ohmic component associated with the current that enters the steel and a parallel ohmic component representative of the current that flows parallel to the steel. Since the current distribution changes with frequency and is nonuniform throughout the grout, the ohmic components must be expressed as complex variables.

A finite-element model of a tendon containing one steel strand was used to gain an understanding of the components that contribute to the indirect impedance. The parallel ohmic impedance was found to be much larger than the series ohmic impedance and is inductive; whereas, the series component is capacitive. If the ohmic impedances are expressed as resistors, the polarization resistance of the steel will be greatly overestimated, and corrosion may be undetected. The series and parallel ohmic impedances change with steel location, resistivity of the grout, and the properties of the steel, making it difficult to extract the interfacial impedance from the indirect impedance data.

Finite-element simulations were also performed to determine how the ohmic impedance components change with variations in electrode spacing and steel polarization resistance. The results showed that when the electrodes are equally spaced apart at a distance relatively similar to the depth of the steel, frequency dispersion was minimized. Changes in the steel polarization resistance also influence the ohmic impedance components. As the polarization resistance increases and the interfacial impedance is more capacitive, the series ohmic impedance becomes more inductive. The parallel ohmic impedance is inductive for all polarization resistances but increases in magnitude as the polarization resistance increases.

Experiments performed on tendons with multiple steel strands including a tendon extracted from the Ringling Bridge as well as tendons on the mock bridge section at Texas A&M brought up some challenges. Specifically, it was shown that corrosion could go undetected if it is not present directly under the working or counter electrodes. For example, if there are 10 steel strands and one of the strands in the center of the tendon is corroding, it would be extremely difficult to detect this from the indirect impedance measurement.

Therefore, any adoption of indirect impedance as a suitable corrosion detection technique would require multiple measurements at multiple locations. The best frequency range to detect corrosion on the strand was at or below 1 Hz.

In supporting work, the corrosion behavior of ASTM A416 steel in alkaline electrolyte was investigated by electrochemical and surface analysis approaches, including X-ray photoelectron spectroscopy (XPS) and high-angle annular dark-field scanning transmission electron microscopy (HAADF-STEM). The power-law model was used to extract values for oxide film thickness from constant-phase element (CPE) parameters obtained as functions of operating conditions. Calibration experiments showed that, despite different silicon content in nominally identical steels, different film thicknesses as observed by HAADF-STEM, and different impedance responses, three samples yielded a common value for ρ_δ, an important parameter in the power-law model. Application of Monte Carlo simulations showed that values of both ρ_δ and δ followed log normal distributions. Application of the power-law model allowed extraction of film thicknesses, yielding 2–6 nm for silicon-rich steel and 1–2 nm for silicon-poor steel.

Chapter 7

Breakdown of Effort Allocated to Work

An estimate of the effort breakdown is presented in Table 7.1.

Table 7.1: Breakdown of experiments and hours spent on each task.

Activity	Unit	Quantity
Background		
Literature review	time	300 h
	Papers read	300
	Papers directly applicable to project	60
Fundamental Studies		
Synthetic tendon	# tendons fabricated	23
	# EIS measurements	300
	# COMSOL Simulations	100
	Simulation computation time	1000 h
	Model development time	450 h
	Regression and simulation time	500 h
steel disk in grout	three-electrode measurements	75
Simulated pore solution	# electrodes fabricated	8
	# of EIS measurements	900
	Model development time	120 h
	Regression analysis time	200 h
surface analysis	MAIC facility time	50 h
	# images	20
	analysis time	150 h
Application		
Mock Bridge	measurements taken	50
Ringling Bridge tendon sections	measurements taken	100

References

1. B. Hirschorn, M. E. Orazem, B. Tribollet, V. Vivier, I. Frateur, and M. Musiani, "Constant-Phase-Element Behavior Caused by Resistivity Distributions in Films: 1. Theory," *Journal of the Electrochemical Society*, **157** (2010) C452–C457.

2. B. Hirschorn, M. E. Orazem, B. Tribollet, V. Vivier, I. Frateur, and M. Musiani, "Constant-Phase-Element Behavior Caused by Resistivity Distributions in Films: 2. Applications," *Journal of the Electrochemical Society*, **157** (2010) C458–C463.

3. S. Joiret, M. Keddam, X. Nóvoa, M. Pérez, C. Rangel, and H. Takenouti, "Use of EIS, Ring-Disk Electrode, EQCM and Raman Spectroscopy to Study the Film of Oxides Formed on Iron in 1 M NaOH," *Cement and Concrete Composites*, **24** (2002) 7–15.

4. J. C. Griess and D. J. Naus, "Corrosion of Steel Tendons Used in Prestressed Concrete Pressure Vessels," in *Corrosion of Reinforcing Steel in Concrete*, D. Tonini and J. Gaidis, editors, STP 713 (Philadelphia, PA: ASTM International, 1980) 32–50.

5. Y.-M. Chen and M. E. Orazem, "Impedance Analysis of ASTM A416 Tendon Steel Corrosion in Alkaline Simulated Pore Solutions," *Corrosion Science*, **104** (2016) 26–35.

6. S. Hurlebaus, M. B. D. Hueste, M. M. Karthik, and T. Terzioglu, *Condition Assessment of Bridge Post-Tensioning and Stay Cable Systems Using NDE Methods*, Final Report Project No. 14-28, Transportation Research Board of The National Academies, Washington, D. C. (2016).

7. Y.-M. Chen, N. G. Rudawski, E. Lambers, and M. E. Orazem, "Application of Impedance Spectroscopy and Surface Analysis to Obtain Oxide Film Thickness," *Journal of the Electrochemical Society*, (2017) in press.

8. W. H. Hartt and S. Venugopalan, *Corrosion Evaluation of Post-Tensioned Tendons on the Mid Bay Bridge in Destin, Florida*, Technical report, Florida Department of Transportation (2002).

9. J. C. Rafols, K. Lau, I. Lasa, M. Paredes, and A. ElSafty, "Approach to Determine Corrosion Propensity in Post-Tensioned Tendons with Deficient Grout," *Open Journal of Civil Engineering*, **3** (2013) 182–187.

10. The Concrete Society, *Durable Post-tensioned Concrete Structures*, 47 (Surrey: The Concrete Society, 1996).

11. E. Proverbio and G. Ricciardi, “Failure of a 40 Years Old Post Tensioned Bridge near Seaside,” in *Proceedings of Eurocorr 2000* (Bedfordshire, 2000) .

12. R. Woodward and F. Williams, “Collapse of Yns-y-gwas Bridge, West Glamorgan,” *Proceedings of the Institution of Civil Engineers*, **84** (1988) 635–669.

13. A. Lewis, “A Moratorium Lifted,” *Concrete*, **30** (1996) 25–27.

14. S. C. Cederquist, “Motor Speedway Bridge Collapse Caused by Corrosion,” *Materials Performance*, **39** (2000) 18–19.

15. R. G. Powers, A. Sagüés, and Y. P. Virmani, *Corrosion of Post-tensioned Tendons in Florida Bridges*, Technical report, Florida Department of Transportation (1999).

16. A. Sagüés, S. Kranc, and R. Hoenhe, *Initial Development of Methods for Assessing Condition of Post-tensioned Tendons of Segmental Bridges*, Final Report, Contract BC374, Florida Department of Transportation (2000).

17. J. Corven, *Mid-bay Bridge Post-tensioning Evaluation*, Technical report, Florida Department of Transportation (2001).

18. R. E. Minchin Jr., *Identification and Demonstration of a Technology Adaptable to Locating Water in Post-tensioned Bridge Tendons*, Final report,, Florida Department of Transportation (2006).

19. A. Ghorbanpoor, *Magnetic-Based NDE of Prestressed and Post-Tensioned Concrete MembersThe MFL System*, Technical report, U. S. Department of Transportation (2000).

20. P. Y. Virmani, *Literature Review of Chloride Threshold Values for Grouted Post-Tensioned Tendons*, Technical report, Federal Highway Administration (2012).

21. J. Martin, K. Broughton, A. Giannopolous, M. Hardy, and M. Forde, “Ultrasonic Tomography of Grouted Duct Post-Tensioned Reinforced Concrete Bridge Beams,” *NDT&E International*, **34** (2001) 107–103.

22. C. Andrade, I. Martinez, and M. Castellote, “Feasibility of Determining Corrosion Rates by Means of Stray Current-induced Polarisation,” *Journal of Applied Electrochemistry*, **38** (2008) 1467–1476.

23. P. J. Monteiro and H. Morrison, “Non-destructive Method of Determining the Position and Condition of Reinforcing Steel in Concrete,” (1999). US Patent 5,855,721.

24. M. Keddam, X. R. Nóvoa, and V. Vivier, “The Concept of Floating Electrode for Contact-Less Electrochemical Measurements: Application to Reinforcing Steel-Bar Corrosion in Concrete,” *Corrosion Science*, **51** (2009) 17951801.

25. A. Sagüés, R. Powers, and H. Wang, “Mechanism of Corrosion of Steel Strands In Post Tensioned Grouted Assemblies,” in *Proceedings of Corrosion/2003*, 312 (Houston: National Association of Corrosion Engineers, 2003) 1–15.

26. L. Bertolini and M. Carsana, "High PH Corrosion of Prestressing Steel in Segregated Grout," in *Modelling of Corroding Concrete Structures*, C. Andrade and G. Mancini, editors (Berlin: Springer, 2011) 147–158.

27. T. Hamilton, J. West, and J. Wouters, *Corrosion of Prestressing Steels*, Committee Report ACI 222.2R-01, American Concrete Institute, Farmington Hills (2001).

28. M. Sánche, J. Gregori, C. Alonso, J. Garca-Jaren, H. Takenouti, and F. Vicente, "Electrochemical Impedance Spectroscopy for Studying Passive Layers on Steel Rebars Immersed In Alkaline Solutions Simulating Concrete Pores," *Electrochimica Acta*, **52** (2007) 7634–7641.

29. J. Flis, H. W. Pickering, and K. Osseo-Asare, "Interpretation of Impedance Data for Reinforcing Steel in Alkaline Solution Containing Chlorides and Acetates," *Electrochimica Acta*, **43** (1998) 1921–1929.

30. L. Dhouibi, E. Triki, and A. Raharinaivo, "The Application of Electrochemical Impedance Spectroscopy to Determine the Long-Term Effectiveness of Corrosion Inhibitors for Steel in Concrete," *Cement and Concrete Composites*, **24** (2002) 35–43.

31. M. Pech-Canul and P. Castro, "Corrosion Measurements of Steel Reinforcement in Concrete Exposed to a Tropical Marine Atmosphere," *Cement and Concrete Research*, **32** (2002) 491–498.

32. E. Barsoukov and J. R. Macdonald, editors, *Impedance Spectroscopy: Theory, Experiment, and Applications*, 2nd edition (Hoboken, NJ: John Wiley & Sons, 2005).

33. A. Lasia, *Electrochemical Impedance Spectroscopy and its Applications* (New York: Springer, 2014).

34. M. E. Orazem and B. Tribollet, *Electrochemical Impedance Spectroscopy* (Hoboken, NJ: John Wiley & Sons, 2008).

35. M. E. Orazem and B. Tribollet, *Electrochemical Impedance Spectroscopy*, 2nd edition (Hoboken: John Wiley & Sons, 2017).

36. M. E. Orazem, B. Tribollet, V. Vivier, S. Marcelin, N. Pébère, A. L. Bunge, E. A. White, D. P. Riemer, I. Frateur, and M. Musiani, "Interpretation of Dielectric Properties for Materials showing Constant-Phase-Element (CPE) Impedance Response," *Journal of the Electrochemical Society*, **160** (2013) C215–C225.

37. G. J. Brug, A. L. G. van den Eeden, M. Sluyters-Rehbach, and J. H. Sluyters, "The Analysis of Electrode Impedances Complicated by the Presence of a Constant Phase Element," *Journal of Electroanalytical Chemistry*, **176** (1984) 275–295.

38. C. H. Hsu and F. Mansfeld, "Technical Note: Concerning the Conversion of the Constant Phase Element Parameter Y_0 into a Capacitance," *Corrosion*, **57** (2001) 747–748.

39. J.-B. Jorcin, M. E. Orazem, N. Pébère, and B. Tribollet, “CPE Analysis by Local Electrochemical Impedance Spectroscopy,” *Electrochimica Acta*, **51** (2006) 1473–1479.

40. E. A. White, M. E. Orazem, and A. L. Bunge, “Characterization of Damaged Skin by Impedance Spectroscopy: Mechanical Damage,” *Pharmaceutical Research*, **30** (2013) 2036–2049.

41. E. A. White, M. E. Orazem, and A. L. Bunge, “Characterization of Damaged Skin by Impedance Spectroscopy: Chemical Damage by Dimethyl Sulfoxide,” *Pharmaceutical Research*, **30** (2013) 2607–2624.

42. M. Musiani, M. E. Orazem, N. Pébère, B. Tribollet, and V. Vivier, “Determination of Resistivity Profiles in Anti-corrosion Coatings from Constant-Phase-Element Parameters,” *Progress in Organic Coatings*, **77** (2014) 2076–2083.

43. A. S. Nguyen, M. Musiani, M. E. Orazem, N. Pébère, B. Tribollet, and V. Vivier, “Impedance Analysis of the Distributed Resistivity of Coatings in Dry and Wet Conditions,” *Electrochimica Acta*, **179** (2015) 452–459.

44. A. S. Nguyen, M. Musiani, M. E. Orazem, N. Pébère, B. Tribollet, and V. Vivier, “Impedance Study of the Influence of Chromates on the Properties of Waterborne Coatings Deposited on 2024 Aluminium Alloy,” *Corrosion Science*, **109** (2016) 174–181.

45. D. P. Riemer and M. E. Orazem, “Impedance Based Characterization of Raw Materials Used in Electrochemical Manufacturing,” *ECS Interface*, **23** (2014) 63–67.

46. M. E. Orazem, B. Tribollet, V. Vivier, D. P. Riemer, E. White, and A. Bunge, “On the Use of the Power-Law Model for Interpreting Constant-Phase-Element Parameters,” *Journal of the Brazilian Chemical Society*, **25** (2014) 532–539.

47. I. Frateur, L. Lartundo-Rojas, C. Méthivier, A. Galtayries, and P. Marcus, “Influence of Bovine Serum Albumin in Sulphuric Acid Aqueous Solution on the Corrosion and the Passivation of an IronChromium Alloy,” *Electrochimica Acta*, **51** (2006) 1550–1557.

48. M. Montemor, A. Simoes, and M. Ferreira, “Analytical Characterization of the Passive Film Formed on Steel in Solutions Simulating the Concrete Interstitial Electrolyte,” *Corrosion*, **54** (1998) 347–353.

49. P. Ghods, O. B. Isgor, F. Bensebaa, and D. Kingston, “Angle-resolved XPS Study of Carbon Steel Passivity and Chloride-induced Depassivation in Simulated Concrete Pore Solution,” *Corrosion Science*, **58** (2012) 159–167.

50. S. Haupt and H. Strehblow, “Corrosion, Layer Formation, and Oxide Reduction of Passive Iron in Alkaline Solution: A Combined Electrochemical and Surface Analytical Study,” *Langmuir*, **3** (1987) 873–885.

51. P. Schmuki, M. Büchler, S. Virtanen, H. Isaacs, M. Ryan, and H. Böhni, “Passivity of Iron in Alkaline Solutions Studied by in-Situ XANES and a Laser Reflection Technique,” *Journal of the Electrochemical Society*, **146** (1999) 2097–2102.

52. P. Graat and M. A. J. Somers, “Quantitative Analysis of Overlapping XPS Peaks by Spectrum Reconstruction: Determination of the Thickness and Composition of Thin Iron Oxide Films,” *Surface and Interface Analysis*, **26** (1998) 773–782.

53. H. B. Gunay, P. Ghods, O. B. Isgor, G. J. Carpenter, and X. Wu, “Characterization of Atomic Structure of Oxide Films on Carbon Steel in Simulated Concrete Pore Solutions Using EELS,” *Applied Surface Science*, **274** (2013) 195–202.

54. O. Khaselev and J. Sykes, “In-situ Electrochemical Scanning Tunneling Microscopy Studies on the Oxidation of Iron in Alkaline Solution,” *Electrochimica Acta*, **42** (1997) 2333–2337.

55. L. Freire, X. Nóvoa, M. Montemor, and M. Carmezim, “Study of Passive Films Formed on Mild Steel in Alkaline Media by the Application of Anodic Potentials,” *Materials Chemistry and Physics*, **114** (2009) 962–972.

56. K. Sohlberg, T. J. Pennycook, W. Zhou, and S. J. Pennycook, “Insights into the Physical Chemistry of Materials from Advances in HAADF-STEM,” *Physical Chemistry Chemical Physics*, **17** (2015) 3982–4006.

57. M. Orazem, D. Bloomquist, C. Alexander, and Y.-M. Chen, *Impedance-Based Detection of Corrosion in Post-Tensioned Cables: Phase 2. Extension of Sensor Development*, Technical Report BDV-31-977-19, Florida Department of Transportation (2014).

58. L. Li and A. A. Sagüés, “Effect of Chloride Concentration on the Pitting and Repassivation Potentials of Reinforcing Steel in Alkaline Solutions,” in *Proceedings of Corrosion/1999*, 567 (Houston: NACE International, 1999) 1–11.

59. V. M.-W. Huang, V. Vivier, M. E. Orazem, N. Pébère, and B. Tribollet, “The Apparent CPE Behavior of an Ideally Polarized Disk Electrode: A Global and Local Impedance Analysis,” *Journal of the Electrochemical Society*, **154** (2007) C81–C88.

60. N. I. Kato, “Reducing focused ion beam damage to transmission electron microscopy samples,” *Journal of Electron Microscopy*, **53** (2004) 451–458.

61. W. M. Haynes, editor, *CRC Handbook of Chemistry and Physics*, 93rd edition (New York, New York: Taylor and Francis Group, LLC, 2012).

62. D. C. Harris, *Quantitative Chemical Analysis* (New York: Macmillan, 2010).

63. P. Ghods, O. Isgor, J. Brown, F. Bensebaa, and D. Kingston, “XPS Depth Profiling Study on the Passive Oxide Film of Carbon Steel in Saturated Calcium Hydroxide Solution and the Effect of Chloride on the Film Properties,” *Applied Surface Science*, **257** (2011) 4669–4677.

64. C. Page, “Mechanism of Corrosion Protection in Reinforced Concrete Marine Structures,” *Nature*, **258** (1975) 514–515.

65. A. Suryavanshi, J. Scantlebury, and S. Lyon, “Corrosion of Reinforcement Steel Embedded in High Water-Cement Ratio Concrete Contaminated with Chloride,” *Cement and Concrete Composites*, **20** (1998) 263–281.

66. G. Glass, R. Yang, T. Dickhaus, and N. Buenfeld, “Backscattered Electron Imaging of the Steel–Concrete Interface,” *Corrosion Science*, **43** (2001) 605–610.

67. R. de Levie, “Electrochemical Responses of Porous and Rough Electrodes,” in *Advances in Electrochemistry and Electrochemical Engineering*, P. Delahay, editor, volume 6 (New York: Interscience, 1967) 329–397.

68. C. L. Alexander, B. Tribollet, and M. E. Orazem, “Contribution of Surface Distributions to Constant-Phase-Element (CPE) Behavior: 1. Influence of Roughness,” *Electrochimica Acta*, **173** (2015) 416–424.

69. M. E. Orazem, N. Pébère, and B. Tribollet, “Enhanced Graphical Representation of Electrochemical Impedance Data,” *Journal of the Electrochemical Society*, **153** (2006) B129–B136.

70. O. J. Murphy, J. O. Bockris, T. E. Pou, D. L. Cocke, and G. Sparrow, “SIMS Evidence Concerning Water in Passive Layers,” *Journal of the Electrochemical Society*, **129** (1982) 2149–2151.

71. J. Eldridge and R. Hoffman, “A Mössbauer Spectroscopy Study of the Potential Dependence of Passivated Iron Films,” *Journal of The Electrochemical Society*, **136** (1989) 955–961.

72. N. N. Greenwood and A. Earnshaw, *Chemistry of the Elements* (Amsterdam: Elsevier, 2012).

73. P. Agarwal, M. E. Orazem, and L. H. García-Rubio, “Measurement Models for Electrochemical Impedance Spectroscopy: I. Demonstration of Applicability,” *Journal of the Electrochemical Society*, **139** (1992) 1917–1927.

74. J. S. Newman, “Frequency Dispersion in Capacity Measurements at a Disk Electrode,” *Journal of the Electrochemical Society*, **117** (1970) 198–203.

75. K. Nisancioglu, “Theoretical Problems Related to Ohmic Resistance Compensation,” in *The Measurement and Correction of Electrolyte Resistance in Electrochemical Tests*, L. L. Scribner and S. R. Taylor, editors, STP 1056 (Philadelphia, PA: American Society for Testing and Materials, 1990) 61–77.

76. K. Nisancioglu, P. O. Gartland, T. Dahl, and E. Sander, “Role of Surface Structure and Flow Rate on the Polarization of Cathodically Protected Steel in Seawater,” *Corrosion*, **43** (1987) 710–718.

77. S. Permeh, K. Krishna Vigneshwaran, and K. Lau, *Corrosion of Post-Tensioned Tendons with Deficient Grout*, Final Report, Project BDV29-977-04, Florida Department of Transportation (2016).